

AD-A122 037

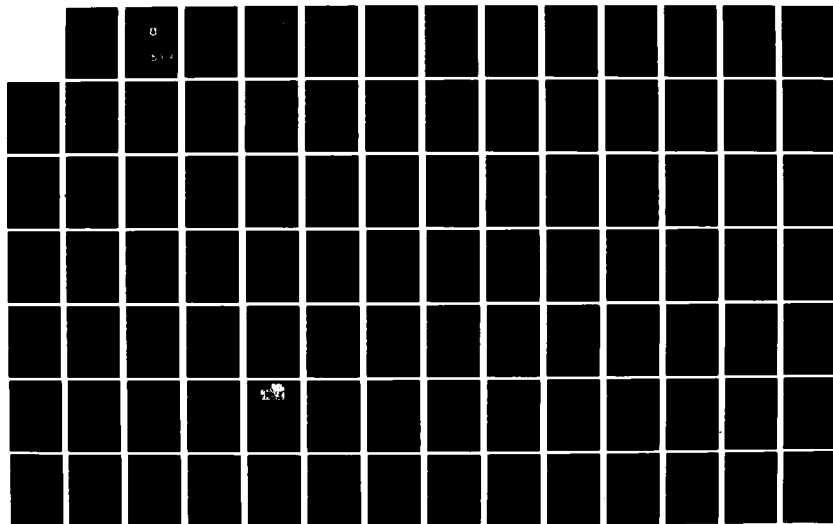
JOURNAL OF ENGINEERING THERMOPHYSICS (SELECTED
ARTICLES)(U) FOREIGN TECHNOLOGY DIV WRIGHT-PATTERSON
AFB OH 04 NOV 82 FTD-ID(RS)T-1011-82

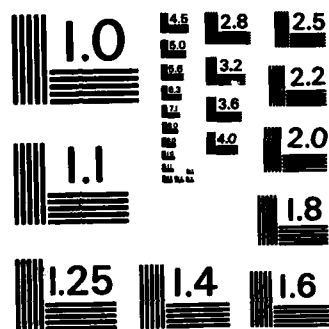
1/2

UNCLASSIFIED

F/G 13/7

NL





MICROCOPY RESOLUTION TEST CHART
NATIONAL BUREAU OF STANDARDS-1963-A

2

AD A 122 037

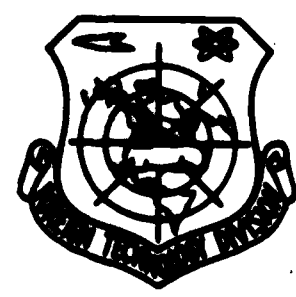
FTD-ID(RS)T-1011-82

FOREIGN TECHNOLOGY DIVISION



JOURNAL OF ENGINEERING THERMOPHYSICS

(Selected Articles)



DTIC
ELECTE
DEC 2 1982
B

DTIC FILE COPY

Approved for public release;
distribution unlimited.



82 12 02 061

EDITED TRANSLATION

FTD-ID(RS)T-1011-82

4 November 1982

MICROFICHE NR: FTD-82-C-001414

JOURNAL OF ENGINEERING THERMOPHYSICS (Selected Articles)

English pages: 112

Source: Gongcheng Rewuli Xuebao, Vol. 1, Nr. 2,
May 1980, pp. 110-155; 165-175; 185-194

Country of origin: China

Translated by: SCITRAN

F33657-81-D-0263

Requester: FTD/TQTA

Approved for public release; distribution unlimited

THIS TRANSLATION IS A RENDITION OF THE ORIGINAL FOREIGN TEXT WITHOUT ANY ANALYTICAL OR EDITORIAL COMMENT. STATEMENTS OR THEORIES ADVOCATED OR IMPLIED ARE THOSE OF THE SOURCE AND DO NOT NECESSARILY REFLECT THE POSITION OR OPINION OF THE FOREIGN TECHNOLOGY DIVISION.

PREPARED BY:

TRANSLATION DIVISION
FOREIGN TECHNOLOGY DIVISION
WP.AFB, OHIO.

Accession For	
NTIS GRA&I	<input checked="checked" type="checkbox"/>
DTIC TAB	<input type="checkbox"/>
Unannounced	<input type="checkbox"/>
Justification	
By	
Distribution/	
Availability Codes	
Dist	Avail and/or Special
A	



Table of Contents

Graphics Disclaimer	ii
Application of Non-Orthogonal Curvilinear Coordinates to Calculate the Flow in Turbomachines, by Chen Nai-xing	1
A General Theory of Three-Dimensional Flow in Transonic Turbomachines with Shocks, by Xu Jian-zhong	15
An Experiment to Improve the Surge Margin by Use of Cascade with Splitter Blades, by Tsui Chih-ya, Zhou Sheng, Lu Ren-fu, Zhang Lian-Chi	29
The Performance Calculation of an Axial Flow Compressor Stage, by Zhang Yu-jing	36
Application of the Finite Element Method to the Solution of Transient Two-Dimensional Temperature Field for Air- Cooled Turbine Blade, by Guo Kuan-liang, Ge Xin-shi, Sun Ziao-lan	51
Computerized Laser Thermal Diffusivity Measurement Apparatus, by Xi Tung-geng, Zhou Sin-yu, Li Zong-jie, Ni He-line, Gu Zong-yi	63
Experimental Investigation of Simulating Impingement Cooling of Concave Surfaces of Turbine Airfoils, by Cheng-Ji-rui, Wang Bao-guan	78
Experimental Investigation of Total-Pressure Loss and Airflow Distribution for Gas Turbine Combustors, by Fan Zuo-min, Chao Zhi-fang	98

GRAPHICS DISCLAIMER

All figures, graphics, tables, equations, etc. merged into this translation were extracted from the best quality copy available.

APPLICATION OF NON-ORTHOGONAL CURVILINEAR
COORDINATES TO CALCULATE THE FLOW
IN TURBOMACHINES*

Chen Nai-xing**

(Marine System Engineering Research Institute)

In the first part of the paper, the formulas of calculating gradients of a scalar, divergents and vorticities of a vector in non-orthogonal curvilinear coordinates are presented by vector analysis. With aid of these relations we then obtained basic aerothermodynamic equations governing relative steady flow of a nonviscous fluid in a turbomachine. General non-orthogonal coordinates are suggested for solving Φ -equation of three-dimensional turbomachine flow. The potential equation for three-dimensional flow calculation is obtained.

Ψ -equations (Wu's equations), expressed in term of general non-orthogonal coordinates, of two kinds of stream surfaces are discussed in the third part.

In the last part of this paper, three forms of velocity gradient formulas are presented.

1. NON-ORTHOGONAL CURVILINEAR COORDINATE SYSTEM

The Publication of Comrade Wu Zhonghua's paper [2] has attracted attention from everywhere. By using the tensor method, he derived for the first time the fundamental equations for 3-dimensional flow in turbomachines in non-orthogonal curvilinear coordinates, which stimulated the development of a design method for turbomachine aerodynamics. We started our work in 1973. The publication of reference [2] has also stimulated and inspired our work.

* This paper has been presented at the Second National Engineering Thermophysics Conference in Hangzhou in November, 1978.

** Currently at the Mechanics Institute, Academic Sinica.

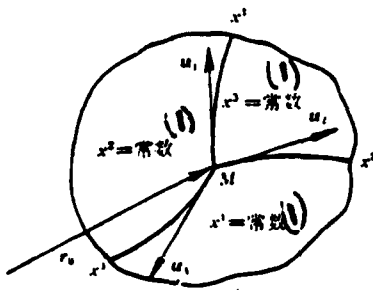


Figure 1. Non-orthogonal curvilinear coordinates.

Key: 1--constant.

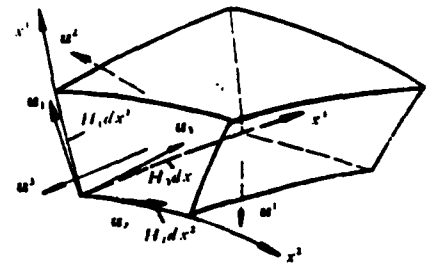


Figure 2. Non-orthogonal curvilinear micro-element.

In a non-orthogonal curvilinear coordinate system, the position of a point M may be represented by the 3 coordinate values x^1, x^2, x^3 . The 3 unit vectors u_1, u_2, u_3 are taken in the tangential directions along the increment directions of the 3 variables x^1, x^2, x^3 at the point M. u^1, u^2, u^3 represent respectively the 3 unit normal vectors perpendicular to the 3 surfaces of the non-orthogonal curvilinear hexahedron with volume dV .

The partial derivatives of the radial vector $r_0(x^1, x^2, x^3)$ may be written as

$$\partial r_0 / \partial x^i = H_i u_i, \quad (i = 1, 2, 3) \quad (1.1)$$

where H_i is the length of $\partial r_0 / \partial x^i$, called the Lamé coefficient. They may be obtained from the following equation:

$$H_i^2 = (\partial r_0 / \partial x^i)^2 = (\partial x / \partial x^i)^2 + (\partial y / \partial x^i)^2 + (\partial z / \partial x^i)^2. \quad (1.2) \quad /111$$

Any vector C decomposed along the 2 sets of 3 non-coplanar vectors u_1, u_2, u_3 and u^1, u^2, u^3 may be written as

$$\begin{aligned} C &= C^1 u_1 + C^2 u_2 + C^3 u_3, \\ C &= C_1 u^1 + C_2 u^2 + C_3 u^3. \end{aligned} \quad (1.3)$$

The relationship between C_1 and C^1 is

$$C_1 = [C^1 \cos(u_1, u_1) + C^2 \cos(u_1, u_2) + C^3 \cos(u_1, u_3)] / \cos(u^1, u_1) \quad (1.4)$$

As is well known, a vector pointing in the direction of the fastest change in a scalar ϕ with a magnitude equal to the derivative in this direction is called the gradient of ϕ . The derivative along an arbitrary direction m is the projection of the gradient ($\nabla\phi$) of ϕ in this direction. According to this definition, it is not difficult to derive the formula for the gradient as:

$$\nabla\phi = \frac{1}{\cos(u^1, u_1)} \frac{\partial\phi}{H_1 \partial x^1} u^1 + \frac{1}{\cos(u^2, u_2)} \frac{\partial\phi}{H_2 \partial x^2} u^2 + \frac{1}{\cos(u^3, u_3)} \frac{\partial\phi}{H_3 \partial x^3} u^3. \quad (1.5)$$

The flux of a vector C per unit volume through the surface of an infinitesimal volume around a point is called the divergence of the vector, i.e.

$$\nabla \cdot C = \lim_{dV \rightarrow 0} \frac{\oint_C C \cdot dA}{dV}.$$

Dividing the sum of the fluxes through the six surfaces $dA_1, dA_2, dA_3, dA'_1, dA'_2, dA'_3$ with the volume dV of the hexahedron we get

$$\nabla \cdot C = [\partial(H_2 H_3 C^1 \Pi) / \partial x^1 + \partial(H_1 H_3 C^2 \Pi) / \partial x^2 + \partial(H_1 H_2 C^3 \Pi) / \partial x^3] / H_1 H_2 H_3 \Pi. \quad (1.6)$$

$$\Pi = \sin(u_2, u_3) \cos(u^1, u_1) = \sin(u_1, u_2) \cos(u^3, u_3) = \sin(u_3, u_1) \cos(u^2, u_2) \quad (1.7)$$

The projection in an arbitrary direction m of the curl $\nabla \times C$ of a vector C may be given in the following definition:

$$(\nabla \times C)_m = \lim_{dA \rightarrow 0} \frac{\oint_C C \cdot dr_i}{dA}$$

where dA is the area enclosed by the closed boundary of the integral \oint_C . Hence it can be seen that $(\nabla \times C)_m$ is independent of the coordinate system. For example, the projection of the curl of vector C along the normal direction u^1 of the surface dA_1 is

$$(\nabla \times C)_u = \{ \partial[H_2 C_2 \cos(u^2, u_2)] / \partial x^2 - \partial[H_2 C_2 \cos(u^2, u_1)] / \partial x^1 \} / H_1 H_2 \sin(u_1, u_2)$$

Finally, we get the expressions of the 3 components of the curl as

$$\left. \begin{aligned} \xi^1 &= \{ \partial[H_2 C_2 \cos(u^2, u_2)] / \partial x^3 - \partial[H_2 C_2 \cos(u^2, u_1)] / \partial x^2 \} / H_1 H_2 \sin(u_1, u_2) \cos(u^1, u_1); \\ \xi^2 &= \{ \partial[H_2 C_2 \cos(u^2, u_2)] / \partial x^1 - \partial[H_1 C_1 \cos(u^1, u_1)] / \partial x^3 \} / H_1 H_2 \sin(u_1, u_2) \cos(u^2, u_2); \\ \xi^3 &= \{ \partial[H_1 C_1 \cos(u^1, u_1)] / \partial x^2 - \partial[H_2 C_2 \cos(u^2, u_2)] / \partial x^1 \} / H_1 H_2 \sin(u_1, u_2) \cos(u^3, u_3). \end{aligned} \right\} \quad (1.8)$$

$$\nabla \times C = \xi^1 u_1 + \xi^2 u_2 + \xi^3 u_3. \quad (1.9)$$

It is not difficult to find the aero-thermodynamic equations of the relatively stable flow in a turbomachine expressed in non-orthogonal curvilinear coordinates by using vector analysis. From equation (1.6) and $\nabla \cdot (\rho W) = 0$, we can obtain the continuity equation as

$$\frac{\partial(H_1 H_2 \rho W^1 \Pi)}{\partial x^1} + \frac{\partial(H_1 H_2 \rho W^2 \Pi)}{\partial x^2} + \frac{\partial(H_1 H_2 \rho W^3 \Pi)}{\partial x^3} = 0. \quad (1.10)$$

Substituting equations (1.8), (1.9) in 2 forms of the equation of motion, i.e.

$$\begin{aligned} \nabla(|W|^2/2) - W \times (\nabla \times W) + 2\omega \times W - \omega^2 r &= -\nabla p / \rho; \\ W \times (\nabla \times V) &= J_R(\nabla I - T \nabla s), \end{aligned}$$

it is easy to derive the 3 components of the equations of motion u^1, u^2, u^3 expressed in terms of the pressure gradient and the gradient of stagnation enthalpy I and entropy s through vector analysis:

$$\begin{aligned} \frac{1}{2} \frac{\partial(W)^2}{\partial x^1} + \frac{W^3}{H_1 H_2} \left\{ \frac{\partial[H_1 W_1 \cos(u^1, u_1)]}{\partial x^2} - \frac{\partial[H_2 W_2 \cos(u^2, u_2)]}{\partial x^1} \right\} \\ - \frac{W^2}{H_1 H_2} \left\{ \frac{\partial[H_2 W_2 \cos(u^2, u_2)]}{\partial x^1} - \frac{\partial[H_1 W_1 \cos(u^1, u_1)]}{\partial x^2} \right\} \\ + 2\omega[W^2 \sin(u_1, u_2) \cos(u^3, e_3) - W^3 \sin(u_1, u_1) \cos(u^2, e_2)] \\ - \omega^2 r \cos(u_1, e_r) = -\frac{1}{\rho H_1} \frac{\partial p}{\partial x^1}; \end{aligned} \quad (1.11a)$$

$$\begin{aligned}
& \frac{1}{2} \frac{\partial(W)^2}{H_2 \partial x^2} + \frac{W^1}{H_1 H_2} \left\{ \frac{\partial[H_2 W_2 \cos(u^2, u_2)]}{\partial x^1} - \frac{\partial[H_1 W_1 \cos(u^1, u_1)]}{\partial x^2} \right\} \\
& - \frac{W^3}{H_2 H_3} \left\{ \frac{\partial[H_3 W_3 \cos(u^3, u_3)]}{\partial x^2} - \frac{\partial[H_2 W_2 \cos(u^2, u_2)]}{\partial x^3} \right\} \\
& + 2\omega[W^3 \sin(u_2, u_3) \cos(u^1, e_s) - W^1 \sin(u_1, u_2) \cos(u^3, e_s)] \\
& - \omega^2 r \cos(u_2, e_r) = -\frac{1}{\rho H_2} \frac{\partial p}{\partial x^2};
\end{aligned} \tag{1.11b}$$

$$\begin{aligned}
& \frac{1}{2} \frac{\partial(W)^2}{H_3 \partial x^3} + \frac{W^2}{H_2 H_3} \left\{ \frac{\partial[H_3 W_3 \cos(u^3, u_3)]}{\partial x^2} - \frac{\partial[H_2 W_2 \cos(u^2, u_2)]}{\partial x^3} \right\} \\
& - \frac{W^1}{H_3 H_1} \left\{ \frac{\partial[H_1 W_1 \cos(u^1, u_1)]}{\partial x^3} - \frac{\partial[H_3 W_3 \cos(u^3, u_3)]}{\partial x^1} \right\} \\
& + 2\omega[W^1 \sin(u_3, u_1) \cos(u^2, e_s) - W^2 \sin(u_2, u_3) \cos(u^1, e_s)] \\
& - \omega^2 r \cos(u_3, e_r) = -\frac{1}{\rho H_3} \frac{\partial p}{\partial x^3}.
\end{aligned} \tag{1.11c}$$

$$\begin{aligned}
& -W^3 \left\{ \frac{\partial[H_1 V_1 \cos(u^1, u_1)]}{\partial x^3} - \frac{\partial[H_3 V_3 \cos(u^3, u_3)]}{\partial x^1} \right\} / H_3 \\
& + W^2 \left\{ \frac{\partial[H_2 V_2 \cos(u^2, u_2)]}{\partial x^1} - \frac{\partial[H_1 V_1 \cos(u^1, u_1)]}{\partial x^2} \right\} / H_2 \\
& = J_g \left(\frac{\partial I}{\partial x^1} - \frac{T \partial s}{\partial x^1} \right);
\end{aligned} \tag{1.12a}$$

$$\begin{aligned}
& -W^1 \left\{ \frac{\partial[H_2 V_2 \cos(u^2, u_2)]}{\partial x^1} - \frac{\partial[H_1 V_1 \cos(u^1, u_1)]}{\partial x^2} \right\} / H_1 \\
& + W^3 \left\{ \frac{\partial[H_3 V_3 \cos(u^3, u_3)]}{\partial x^2} - \frac{\partial[H_2 V_2 \cos(u^2, u_2)]}{\partial x^3} \right\} / H_3 \\
& = J_g \left(\frac{\partial I}{\partial x^2} - T \frac{\partial s}{\partial x^2} \right);
\end{aligned} \tag{1.12b}$$

$$\begin{aligned}
& -W^2 \left\{ \frac{\partial[H_3 V_3 \cos(u^3, u_3)]}{\partial x^2} - \frac{\partial[H_2 V_2 \cos(u^2, u_2)]}{\partial x^3} \right\} / H_2 \\
& + W^1 \left\{ \frac{\partial[H_1 V_1 \cos(u^1, u_1)]}{\partial x^3} - \frac{\partial[H_3 V_3 \cos(u^3, u_3)]}{\partial x^1} \right\} / H_1 \\
& = J_g \left(\frac{\partial I}{\partial x^3} - \frac{T \partial s}{\partial x^3} \right).
\end{aligned} \tag{1.12c}$$

/113

2. POTENTIAL FUNCTION EQUATION OF TURBOMACHINE 3 DIMENSIONAL POTENTIAL FLOW

Let the flow in the interior of the turbomachine be isentropic with both the total enthalpy and entropy uniform at the inlet. Hence, (except for $V // \nabla \times V$) $\nabla \times V = 0$, ϕ , there exists a potential function, in the absolute flow field. Its gradient is related to the non-orthogonal velocity component by

$$V_i = \left(\frac{\partial \phi}{H_i dx^i} \right) / \cos(u^i, u_i) \quad (i = 1, 2, 3); \quad (2.1)$$

$$V^i = \frac{1}{\cos(u^i, u_i)} \left[\frac{\cos(u^i, u_1)}{\cos(u^1, u_1)} \frac{\partial \phi}{H_1 \partial x^1} + \frac{\cos(u^i, u_2)}{\cos(u^2, u_2)} \frac{\partial \phi}{H_2 \partial x^2} + \frac{\cos(u^i, u_3)}{\cos(u^3, u_3)} \frac{\partial \phi}{H_3 \partial x^3} \right] \quad (i = 1, 2, 3). \quad (2.2)$$

Substituting the above equation into equation (1.10), we get, after simplification, the potential function equation

$$\begin{aligned} & B_{11}(\partial^2 \phi / \partial x^{12}) + B_{22}(\partial^2 \phi / \partial x^{22}) + B_{33}(\partial^2 \phi / \partial x^{32}) + 2B_{12}(\partial^2 \phi / \partial x^1 \partial x^2) \\ & + 2B_{23}(\partial^2 \phi / \partial x^2 \partial x^3) + 2B_{31}(\partial^2 \phi / \partial x^3 \partial x^1) + (\partial \phi / \partial x^1)(\partial B_{11} / \partial x^1 \\ & + \partial B_{21} / \partial x^2 + \partial B_{31} / \partial x^3) + (\partial \phi / \partial x^2)(\partial B_{12} / \partial x^1 + \partial B_{22} / \partial x^2 + \partial B_{32} / \partial x^3) \\ & + (\partial \phi / \partial x^3)(\partial B_{13} / \partial x^1 + \partial B_{23} / \partial x^2 + \partial B_{33} / \partial x^3) = \omega(\partial A_1 / \partial x^1 \\ & + \partial A_2 / \partial x^2 + \partial A_3 / \partial x^3) - H_1 H_2 H_3 \Pi (W^1 \partial \ln \rho / H_1 \partial x^1 \\ & + W^2 \partial \ln \rho / H_2 \partial x^2 + W^3 \partial \ln \rho / H_3 \partial x^3). \end{aligned} \quad (2.3)$$

The coefficients $A_1, A_2, A_3, B_{11}, B_{12}, \dots$ are functions of the geometrical parameters. Its expression is

$$A_i = \frac{r H_1 H_2 H_3 \Pi}{H_i} \frac{\cos(u^i, e_\theta)}{\cos(u^i, u_i)}; \quad B_{ij} = B_{ji} = \frac{H_1 H_2 H_3}{H_i H_j} \frac{\Pi \cos(u^i, u^j)}{\cos(u^i, u_i) \cos(u^j, u_j)}. \quad (2.4)$$

The equation for the potential function belongs to the solution of the boundary problems of the second kind. Hence, its boundary conditions may be obtained from the condition that the product of the normal unit vector to the wall and the velocity vector vanishes, i.e., $n \cdot W = 0$. For regions up or down stream far away from the blade, the direction of air flow velocity

is usually parallel to the inner and outer shells, e.g. for an axial flow turbomachine outlet, we have

$$W_r = \partial\Phi/\partial r = 0 \quad (z = \pm\infty).$$

For some special cases, the potential function equation may be simplified somewhat. For example: by choosing the angular ϕ coordinate as x^2 coordinate, and any non-orthogonal curvilinear coordinates e_θ and e_1, e_3 in the meridional plane as X^1 and X^3 , we have

$$\begin{aligned} & \frac{H_1 H_2}{H_1 \sin \theta_{13}} \frac{\partial^2 \Phi}{\partial x^{12}} + \frac{H_3 H_1}{H_2 \sin \theta_{13}} \frac{\partial^2 \Phi}{\partial x^{22}} + \frac{H_1 H_2}{H_3 \sin \theta_{13}} \frac{\partial^2 \Phi}{\partial x^{32}} - 2 \frac{H_2 \cos \theta_{13}}{\sin \theta_{13}} \frac{\partial^2 \Phi}{\partial x^3 \partial x^1} \\ & + \left[\partial \left(\frac{H_3 H_2}{H_1 \sin \theta_{13}} \right) / \partial x^1 - \partial \left(\frac{H_2 \cos \theta_{13}}{\sin \theta_{13}} \right) / \partial x^3 \right] \frac{\partial \Phi}{\partial x^1} \\ & + \left[\partial \left(\frac{H_3 H_1 \sin \theta_{13}}{H_2} \right) / \partial x^2 \right] \frac{\partial \Phi}{\partial x^2} + \left[\partial \left(\frac{H_1 H_2}{H_3 \sin \theta_{13}} \right) / \partial x^3 \right. \\ & \left. - \partial \left(\frac{H_2 \cos \theta_{13}}{\sin \theta_{13}} \right) / \partial x^1 \right] \frac{\partial \Phi}{\partial x^3} = -\omega \frac{\partial(r H_1 H_2 \sin \theta_{13})}{H_1 \partial x^1} \\ & - H_1 H_2 H_3 \sin \theta_{13} \left(\frac{W^1}{H_1} \frac{\partial \ln \rho}{\partial x^1} + \frac{W^2}{H_2} \frac{\partial \ln \rho}{\partial x^2} + \frac{W^3}{H_3} \frac{\partial \ln \rho}{\partial x^3} \right). \end{aligned} \quad (2.5)$$

The boundary conditions near the wall is

/114

$$n \cdot W = n^1 (\partial\Phi/H_1 \partial x^1) + n_\theta (\partial\Phi/H_2 \partial x^2 - \omega r) + n^3 (\partial\Phi/H_3 \partial x^3) = 0 \quad (2.6)$$

where n_θ, n^1 are, respectively, the components along the 3 directions u_1, u_2, u_3 of the normal unit vector to the wall.

3. NON-ORTHOGONAL CURVILINEAR COORDINATE STREAM FUNCTION EQUATION OF BINARY RELATIVE FLOW SURFACE

As early as 1952, Professor Wm. Zhonghua proposed a general computational model to obtain the solution to 3 dimensional flow by taking advantage of binary relative flow surfaces (S_1, S_2) to simplify 3 dimensional flow into two 2 dimensional problems, so that the binary relative flow surfaces may be iterated. The flow matrix method or velocity gradient method (streamline curvature

method) may be used to solve for this binary relative flow surface. In the former method, the stream function Ψ is used as the unknown to find the various parameters in the flow field. In the calculation of the S_1 stream surface, it is common to apply the equation of motion in the second form. Here, x^2 and x^3 are the curvilinear coordinates in the stream surface S_1 , and x^1 is normal to the stream surface; the velocity component along the u_1 direction and the curl of V are zero.

$$\left\{ \frac{\partial [H_2 W_2 \cos(u^2, u_1)]}{\partial x^3} - \frac{\partial [H_1 W_1 \cos(u^3, u_1)]}{\partial x^2} \right\} / H_1 H_2 \sin(u_2, u_1) \cos(u^1, u_1) + 2\omega \cos(u^1, e_z) / \cos(u^1, u_1) = 0. \quad (3.1)$$

In the case of uniformly distributed stagnant rotation enthalpy and entropy, for the stream surface S_1 in the form of the surface of revolution, the stream function Ψ that satisfies the continuity equation

$$\frac{\partial (H_2 \tau \rho W^2 \sin \theta_{23})}{\partial x^1} + \frac{\partial (H_1 \tau \rho W^3 \sin \theta_{23})}{\partial x^3} = 0 \quad (3.2)$$

has the following relations

$$\frac{\partial \Psi}{\partial x^1} = H_2 \tau \rho g W^3 \sin \theta_{23}, \quad \frac{\partial \Psi}{\partial x^3} = -H_1 \tau \rho g W^2 \sin \theta_{23}. \quad (3.3)$$

Substituting the above equations into eg (3.1), we may obtain the same stream function equation (Wu's equation) as in Reference [2]:

$$\frac{1}{H_1^2} \frac{\partial^2 \Psi}{\partial (x^1)^2} + \frac{D}{H_1 H_2} \frac{\partial^2 \Psi}{\partial x^2 \partial x^3} + \frac{1}{H_2^2} \frac{\partial^2 \Psi}{\partial (x^3)^2} + E \frac{\partial \Psi}{H_1 \partial x^1} + F \frac{\partial \Psi}{H_2 \partial x^3} = G. \quad (3.4)$$

$$\begin{aligned} D &= -2 \cos \theta_{23}, \\ E &= \frac{\partial}{\partial x^2} \left(\ln \frac{H_1}{H_2 \sin \theta_{23}} \right) - \frac{\partial \ln \tau}{\partial x^2} + \cos \theta_{23} \frac{\partial \ln \tau}{\partial x^1} + \frac{1}{\sin \theta_{23}} \frac{\partial \theta_{23}}{\partial x^2}, \\ F &= \frac{\partial}{\partial x^3} \left(\ln \frac{H_2}{H_1 \sin \theta_{23}} \right) - \frac{\partial \ln \tau}{\partial x^3} + \cos \theta_{23} \frac{\partial \ln \tau}{\partial x^1} + \frac{1}{\sin \theta_{23}} \frac{\partial \theta_{23}}{\partial x^3}, \\ G &= 2\omega \tau \rho g \sin \sigma \sin^2 \theta_{23} + \frac{\partial \Psi}{\partial x^2} \left(\frac{\partial \ln \rho}{\partial x^2} - \cos \theta_{23} \frac{\partial \ln \rho}{\partial x^3} \right) \\ &\quad + \frac{\partial \Psi}{\partial x^3} \left(\frac{\partial \ln \rho}{\partial x^3} - \cos \theta_{23} \frac{\partial \ln \rho}{\partial x^2} \right) + Jg \left(\frac{\partial I}{\partial x^2} - T \frac{\partial s}{\partial x^2} \right) \\ &\quad + \tau^2 \rho^2 g^2 \sin^2 \theta_{23} / \left(\frac{\partial \Psi}{\partial x^2} \right). \end{aligned} \quad (3.5)$$

The coordinate system for the S_2 stream surface stream function equation may be chosen as follows: $x^2 = \varphi$, X^1 and X^3 are the non-orthogonal curvilinear coordinates on the meridional plane. Also let n be the unit normal vector perpendicular to the S_2 stream surface. The partial derivatives along the stream surface with respect to X^1 and X^2 are

$$\frac{\partial(\quad)}{H_1 \partial x^1} = \frac{\partial(\quad)}{H_1 \partial x^1} + \frac{n_1 \cos(u^1, u_1)}{n_2} \frac{\partial(\quad)}{r \partial \varphi}; \quad \frac{\partial(\quad)}{H_3 \partial x^3} = \frac{\partial(\quad)}{H_3 \partial x^3} + \frac{n_3 \cos(u^3, u_1)}{n_2} \frac{\partial(\quad)}{r \partial \varphi}. \quad (3.6)$$

Taking into consideration the force exerted on the stream surface due to circumferential pressure gradient

/11

$$F = - \left(\frac{1}{n_2} \frac{1}{\rho} \frac{\partial p}{r \partial \varphi} \right) n = F_1 u^1 + F_2 u^2 + F_3 u^3.$$

and the perpendicular relationship between the force F and the stream velocity W as well as the relationship between the unit normal vector n and the stream velocity W , after simplification we get the three component equations of the equation of motion for the S_2 stream surface as

$$\begin{aligned} & W^1 \frac{\partial W^1}{H_1 \partial x^1} + W^2 \frac{\partial W^2}{H_3 \partial x^3} + \left(W^1 \frac{\partial W^1}{H_1 \partial x^1} + W^2 \frac{\partial W^2}{H_3 \partial x^3} \right) \cos \theta_{31} \\ & - \left(2\omega W_\varphi + \omega^2 r + \frac{W_\varphi^2}{r} \right) \cos \theta_1 \\ & + W^3 (W^1 + W^2 \cos \theta_{31}) \frac{1}{H_1} \frac{\partial H_1}{H_3 \partial x^3} \\ & - W^3 (W^2 + W^1 \cos \theta_{31}) \frac{1}{H_3} \frac{\partial H_3}{H_1 \partial x^1} = - \frac{1}{\rho} \frac{\partial p}{H_1 \partial x^1} + F_1^*; \end{aligned} \quad (3.7a)$$

$$W^1 \frac{\partial W_\varphi}{H_1 \partial x^1} + W^2 \frac{\partial W_\varphi}{H_3 \partial x^3} + \left(\frac{W_\varphi}{r} + 2\omega \right) (W^1 \cos \theta_1 + W^2 \sin \theta_3) = F_2^* \quad (3.7b)$$

or

$$\begin{aligned} & \frac{W^1}{r} \frac{\partial (V_\varphi r)}{H_1 \partial x^1} + \frac{W^2}{r} \frac{\partial (V_\varphi r)}{H_3 \partial x^3} = F_2^*; \\ & W^1 \frac{\partial W^2}{H_1 \partial x^1} + W^2 \frac{\partial W^2}{H_3 \partial x^3} + \left(W^1 \frac{\partial W^1}{H_1 \partial x^1} + W^2 \frac{\partial W^1}{H_3 \partial x^3} \right) \cos \theta_{31} \end{aligned} \quad (3.7b')$$

$$\begin{aligned} & - \left(2\omega W_\varphi + \omega^2 r + \frac{W_\varphi^2}{r} \right) \sin \theta_3 + W^1 (W^1 \cos \theta_{31} + W^2) \frac{1}{H_3} \frac{\partial H_1}{H_1 \partial x^1} \\ & - W^1 (W^1 + W^2 \cos \theta_{31}) \frac{1}{H_1} \frac{\partial H_1}{H_3 \partial x^3} - (W^1)^2 \sin \theta_{31} \frac{\partial \theta_{31}}{H_3 \partial x^1} \\ & = - \frac{1}{\rho} \frac{\partial p}{H_3 \partial x^3} + F_3^*. \end{aligned} \quad (3.7c)$$

By using the same method, we may obtain the equation of motion expressed in terms of the gradients of the stagnant rotation enthalpy and entropy.

$$\begin{aligned}
 & -\frac{W_\varphi}{r} \frac{\partial(V_\varphi r)}{H_1 \partial x^1} + W^3 \left(\frac{\partial W^1}{H_3 \partial x^3} - \frac{\partial W^3}{H_1 \partial x^1} \right) + W^3 \cos \theta_{31} \left(\frac{\partial W^3}{H_3 \partial x^3} - \frac{\partial W^1}{H_1 \partial x^1} \right) \\
 & + W^3 (W^1 + W^3 \cos \theta_{31}) \frac{1}{H_1} \frac{\partial H_1}{H_3 \partial x^3} - W^3 (W^1 \cos \theta_{31} + W^3) \frac{1}{H_3} \frac{\partial H_3}{H_1 \partial x^1} \\
 & + W^3 \sin \theta_{31} \left(W^1 \frac{\partial \theta_{31}}{H_1 \partial x^1} - W^3 \frac{\partial \theta_{31}}{H_3 \partial x^3} \right) = J_g \left(-\frac{\partial I}{H_1 \partial x^1} + T \frac{\partial s}{H_1 \partial x^1} \right) \\
 & + F_1^*;
 \end{aligned} \tag{3.8a}$$

$$\frac{W^1}{r} \frac{\partial(V_\varphi r)}{H_1 \partial x^1} + \frac{W^3}{r} \frac{\partial(V_\varphi r)}{H_3 \partial x^3} = F_2^*; \tag{3.8b}$$

$$\begin{aligned}
 & -\frac{W_\varphi}{r} \frac{\partial(V_\varphi r)}{H_3 \partial x^3} + W^1 \left(\frac{\partial W^3}{H_1 \partial x^1} - \frac{\partial W^1}{H_3 \partial x^3} \right) + W^1 \cos \theta_{31} \left(\frac{\partial W^1}{H_1 \partial x^1} - \frac{\partial W^3}{H_3 \partial x^3} \right) \\
 & + W^1 (W^1 \cos \theta_{31} + W^3) \frac{1}{H_3} \frac{\partial H_3}{H_1 \partial x^1} - W^1 (W^1 + W^3 \cos \theta_{31}) \frac{1}{H_1} \frac{\partial H_1}{H_3 \partial x^3} \\
 & + W^1 \sin \theta_{31} \left(W^3 \frac{\partial \theta_{31}}{H_3 \partial x^3} - W^1 \frac{\partial \theta_{31}}{H_1 \partial x^1} \right) = J_g \left(-\frac{\partial I}{H_3 \partial x^3} + T \frac{\partial s}{H_3 \partial x^3} \right) \\
 & + F_3^*.
 \end{aligned} \tag{3.8c} \quad /116$$

$$\left. \begin{aligned}
 F_1^* &= -F_1 \sin \theta_{31} = -\frac{1}{\rho} \frac{\partial p}{r \partial \varphi} \frac{n_1}{n_2} \sin \theta_{31}; \\
 F_2^* &= -F_2 = -\frac{1}{\rho} \frac{\partial p}{r \partial \varphi} = F_\varphi; \\
 F_3^* &= -F_3 \sin \theta_{31} = -\frac{1}{\rho} \frac{\partial p}{r \partial \varphi} \frac{n_3}{n_2} \sin \theta_{31}
 \end{aligned} \right\} \tag{3.9}$$

$$F_1^* = F_2^* \frac{n_1}{n_2} \sin \theta_{31}; \quad F_3^* = F_2^* \frac{n_3}{n_2} \sin \theta_{31}. \tag{3.10}$$

$$F_1^* W^1 + F_2^* W_\varphi + F_3^* W^3 = 0. \tag{3.11}$$

If the partial derivatives of the stream function of the continuity equation which satisfies the S_2 stream surface

$$\frac{\partial(H_3 \tau \rho W^1 \sin \theta_{31})}{\partial x^1} + \frac{\partial(H_1 \tau \rho W^3 \sin \theta_{31})}{\partial x^3} = 0 \tag{3.12}$$

is

$$\frac{\partial \Psi}{\partial x^1} = H_1 \tau \rho g W^3 \sin \theta_{31}; \quad \frac{\partial \Psi}{\partial x^3} = -H_3 \tau \rho g W^1 \sin \theta_{31}. \quad (3.13)$$

Substitution of the above equation into the first component equation (3.7a) of the equation of motion gives the stream function equation of the S_2 stream surface [2]

$$\frac{1}{H_1^2} \frac{\partial^2 \Psi}{(\partial x^1)^2} + \frac{D}{H_1 H_3} \frac{\partial^2 \Psi}{\partial x^1 \partial x^3} + \frac{1}{H_3^2} \frac{\partial^2 \Psi}{(\partial x^3)^2} + E \frac{\partial \Psi}{H_1 \partial x^1} + F \frac{\partial \Psi}{H_3 \partial x^3} = G. \quad (3.14)$$

where the coefficients are respectively

$$\left. \begin{aligned} D &= -2 \cos \theta_{31}, \\ E &= \frac{\partial}{H_1 \partial x^1} \left(\ln \frac{H_1}{H_1 \sin \theta_{31}} \right) - \frac{\partial \ln \tau}{H_1 \partial x^1} + \cos \theta_{31} \frac{\partial \ln \tau}{H_3 \partial x^3} + \frac{1}{\sin \theta_{31}} \frac{\partial \theta_{31}}{H_3 \partial x^3}, \\ F &= \frac{\partial}{H_3 \partial x^3} \left(\ln \frac{H_1}{H_3 \sin \theta_{31}} \right) - \frac{\partial \ln \tau}{H_3 \partial x^3} + \cos \theta_{31} \frac{\partial \ln \tau}{H_1 \partial x^1} + \frac{1}{\sin \theta_{31}} \frac{\partial \theta_{31}}{H_1 \partial x^1}, \\ G &= \frac{\partial \Psi}{H_1 \partial x^1} \left(\frac{\partial \ln \rho}{H_1 \partial x^1} - \frac{\partial \ln \rho}{H_3 \partial x^3} \cos \theta_{31} \right) + \frac{\partial \Psi}{H_3 \partial x^3} \left(\frac{\partial \ln \rho}{H_3 \partial x^3} - \frac{\partial \ln \rho}{H_1 \partial x^1} \cos \theta_{31} \right) \\ &\quad + \tau \sin \theta_{31} \rho g H, \\ H &= \left[-\frac{W_\varphi}{r} \frac{\partial (V_\varphi r)}{H_1 \partial x^1} + J_g \left(\frac{\partial l}{H_1 \partial x^1} - T \frac{\partial s}{H_1 \partial x^1} \right) - F_1^* \right] / W^3 \end{aligned} \right\} \quad (3.15)$$

See Reference [2] for solutions to this problem and the reverse problem.

4. THE FUNDAMENTAL SET OF EQUATIONS OF THE S_1 AND S_2 STREAM SURFACES IS SUTIBALE FOR THE VELOCITY GRADIENT METHOD

Professor Wu Zhonghua proposed as early as 1950 the velocity gradient method (or also known as the stream line curvature method) [7] with station by station calculation to simplify the 2 dimensional problem of the whole field into the 1 dimensional method of each calculation station. The equation for stream surface S_1 derived in this paper may be applied to the case of a surface of revolution.

The velocity gradient equation of the S_1 stream surface is usually written in 3 forms. In order to save space, we shall write the velocity gradient equation in the following form:

$$\partial W^3 / r \partial \varphi + P W^3 + Q = 0 \quad (4.1)$$

Table 1. Computational formulae for the coefficients P, Q of the velocity gradient equation of S_1 and S_2 stream surfaces.

2 方程形式	1 系数	P	Q
3 S ₁ 流面	I	$\frac{1}{1 + \Lambda_1 \cos \theta_{11}} \left[-\frac{\partial \ln W^3}{H_1 \partial x^1} (\Lambda_1 + \cos \theta_{11}) + \left(\cos \theta_{11} \frac{\partial \Lambda_1}{r \partial \varphi} - \frac{\partial \Lambda_1}{H_1 \partial x^1} \right) - \Lambda_1 \left(\frac{\partial \ln r}{H_1 \partial x^1} - \cos \theta_{11} \frac{\partial \ln H_1}{r \partial \varphi} + \sin \theta_{11} \frac{\partial \theta_{11}}{r \partial \varphi} \right) + \left(\frac{\partial \ln H_1}{r \partial \varphi} - \cos \theta_{11} \frac{\partial \ln r}{H_1 \partial x^1} + \sin \theta_{11} \frac{\partial \theta_{11}}{H_1 \partial x^1} \right) \right]$	$-\frac{2\omega r \sin \sigma \sin \theta_{11}}{1 + \Lambda_1 \cos \theta_{11}}$
	II	$\frac{1}{1 - (M^2)^2 (\Lambda_1^2 + 2\Lambda_1 \cos \theta_{11} + 1)} \cdot \frac{\Lambda_1 + \cos \theta_{11}}{\Lambda_1^2 + 2\Lambda_1 \cos \theta_{11} + 1} \left\{ \Lambda_1 \left(\frac{\partial \ln H_1}{r \partial \varphi} + \cot \theta_{11} \frac{\partial \theta_{11}}{r \partial \varphi} + \frac{\partial \ln \tau}{r \partial \varphi} \right) + \left(\frac{\partial \ln r}{H_1 \partial x^1} + \cot \theta_{11} \frac{\partial \theta_{11}}{H_1 \partial x^1} + \frac{\partial \ln \tau}{H_1 \partial x^1} \right) + \frac{\partial \Lambda_1}{r \partial \varphi} - (M^2)^2 \left[(\Lambda_1 + \cos \theta_{11}) \frac{\partial \Lambda_1}{H_1 \partial x^1} - \Lambda_1 \sin \theta_{11} \frac{\partial \theta_{11}}{H_1 \partial x^1} - \frac{\omega^2 r}{(W_1)^2} \frac{Dr}{H_1 \partial x^1} \right] \right\} + \frac{1}{\Lambda_1^2 + 2\Lambda_1 \cos \theta_{11} + 1} \left[\left(\cos \theta_{11} \frac{\partial \Lambda_1}{r \partial \varphi} - \frac{\partial \Lambda_1}{H_1 \partial x^1} \right) - \Lambda_1 \left(\frac{\partial \ln r}{H_1 \partial x^1} - \cos \theta_{11} \frac{\partial \ln H_1}{r \partial \varphi} + \sin \theta_{11} \frac{\partial \theta_{11}}{r \partial \varphi} \right) + \left(\frac{\partial \ln H_1}{r \partial \varphi} - \cos \theta_{11} \frac{\partial \ln r}{H_1 \partial x^1} + \sin \theta_{11} \frac{\partial \theta_{11}}{H_1 \partial x^1} \right) \right]$	$-\frac{2\omega r \sin \sigma \sin \theta_{11}}{\Lambda_1^2 + 2\Lambda_1 \cos \theta_{11} + 1}$
	III	$\left\{ \Lambda_1^2 \left(\frac{\partial \ln H_1}{r \partial \varphi} + \cot \theta_{11} \frac{\partial \theta_{11}}{r \partial \varphi} + \frac{\partial \ln \tau}{r \partial \varphi} \right) + \Lambda_1 \left(2 \cos \theta_{11} \frac{\partial \ln H_1}{r \partial \varphi} + \frac{\cos 2\theta_{11}}{\sin \theta_{11}} \frac{\partial \theta_{11}}{r \partial \varphi} + \frac{\partial \theta_{11}}{r \partial \varphi} + \cot \theta_{11} \frac{\partial \theta_{11}}{H_1 \partial x^1} + \cos \theta_{11} \frac{\partial \ln \tau}{r \partial \varphi} + \frac{\partial \ln \tau}{H_1 \partial x^1} \right) + \left(\frac{\partial \ln H_1}{r \partial \varphi} + \frac{1}{\sin \theta_{11}} \frac{\partial \theta_{11}}{H_1 \partial x^1} + \cos \theta_{11} \frac{\partial \ln \tau}{H_1 \partial x^1} \right) + \frac{\partial \Lambda_1}{r \partial \varphi} (\Lambda_1 + 2 \cos \theta_{11}) - \frac{\partial \Lambda_1}{H_1 \partial x^1} + (\Lambda_1 + \cos \theta_{11}) \left(\frac{\partial \ln \rho}{H_1 \partial x^1} + \cos \theta_{11} \frac{\partial \ln \rho}{H_1 \partial x^1} \right) \right\} / (\Lambda_1^2 + 2\Lambda_1 \cos \theta_{11} + 1)$	$-\frac{2\omega r \sin \sigma \sin \theta_{11}}{\Lambda_1^2 + 2\Lambda_1 \cos \theta_{11} + 1}$
4 S ₂ 流面	I	$\frac{1}{1 + \Lambda \cos \theta_{11}} \left[-\frac{\partial \ln W^3}{H_1 \partial x^1} (\Lambda + \cos \theta_{11}) + \left(\cos \theta_{11} \frac{\partial \Lambda}{H_1 \partial x^1} - \frac{\partial \Lambda}{H_1 \partial x^1} \right) - \Lambda \left(\frac{\partial \ln H_1}{H_1 \partial x^1} - \cos \theta_{11} \frac{\partial \ln H_1}{H_1 \partial x^1} + \sin \theta_{11} \frac{\partial \theta_{11}}{H_1 \partial x^1} \right) + \left(\frac{\partial \ln H_1}{H_1 \partial x^1} - \cos \theta_{11} \frac{\partial \ln H_1}{H_1 \partial x^1} + \sin \theta_{11} \frac{\partial \theta_{11}}{H_1 \partial x^1} \right) \right]$	$\frac{1}{W^3 (1 + \Lambda \cos \theta_{11})} \left[\frac{W^3}{r} \frac{\partial (V_{gr})}{H_1 \partial x^1} + Jg \left(-\frac{\partial I}{H_1 \partial x^1} + T \cdot \frac{\partial I}{H_1 \partial x^1} \right) + F_1^2 \right]$
	II	$\left\{ \Lambda^2 \left(\frac{\partial \ln H_1}{H_1 \partial x^1} + \cot \theta_{11} \frac{\partial \theta_{11}}{H_1 \partial x^1} + \frac{\partial \ln \tau}{H_1 \partial x^1} \right) + \Lambda \left(2 \cos \theta_{11} \frac{\partial \ln H_1}{H_1 \partial x^1} + \frac{\cos 2\theta_{11}}{\sin \theta_{11}} \frac{\partial \theta_{11}}{H_1 \partial x^1} + \cot \theta_{11} \frac{\partial \theta_{11}}{H_1 \partial x^1} + \cos \theta_{11} \frac{\partial \ln \tau}{H_1 \partial x^1} + \frac{\partial \ln \tau}{H_1 \partial x^1} \right) + \left(\frac{\partial \ln H_1}{H_1 \partial x^1} + \frac{1}{\sin \theta_{11}} \frac{\partial \theta_{11}}{H_1 \partial x^1} + \cos \theta_{11} \frac{\partial \ln \tau}{H_1 \partial x^1} \right) + \frac{\partial \Lambda}{H_1 \partial x^1} (\Lambda + 2 \cos \theta_{11}) - \frac{\partial \Lambda}{H_1 \partial x^1} + (\Lambda + \cos \theta_{11}) \cdot \left(\frac{\partial \ln \rho}{H_1 \partial x^1} + \Lambda \frac{\partial \ln \rho}{H_1 \partial x^1} \right) \right\} / (\Lambda^2 + 2\Lambda \cos \theta_{11} + 1)$	$\left[\frac{W^3}{r} \frac{\partial (V_{gr})}{H_1 \partial x^1} + Jg \cdot \left(-\frac{\partial I}{H_1 \partial x^1} + T \frac{\partial I}{H_1 \partial x^1} \right) + F_1^2 \right] + W^3 (\Lambda^2 + 2\Lambda \cos \theta_{11} + 1)$

key: 1--coefficient; 2--form of equation; 3-- S_1 stream surface; 4-- S_2 stream surface; 5-- S_1 stream surface.

系数 方程形式		P	Q
S ₁ 流 面	III	$\frac{1}{1 - (M^2)(\Lambda^2 + 2\Lambda \cos \theta_{31} + 1)} \cdot \frac{\Lambda + \cos \theta_{31}}{\Lambda^2 + 2\Lambda \cos \theta_{31} + 1} \left\{ \Lambda \frac{\partial \ln H_1}{H_1 \partial x^1} \right.$ $+ \frac{\partial \ln H_1}{H_1 \partial x^1} + \operatorname{ctg} \theta_{31} \frac{D \theta_{31}}{H_1 dx^1} + \frac{D \ln r}{H_1 dx^1} + \frac{\partial \Lambda}{H_1 \partial x^1}$ $+ (M^2) \left[\Lambda \sin \theta_{31} \frac{D \theta_{31}}{H_1 dx^1} + \frac{(V_{\varphi r})^2}{r^2 (W^3)^2} \frac{Dr}{H_1 dx^1} - (\Lambda + \cos \theta_{31}) \right.$ $\cdot \frac{D \Lambda}{H_1 dx^1} - \frac{(V_{\varphi r} - \omega r^2)}{r^2 (W^3)^2} \frac{D(V_{\varphi r})}{H_1 dx^1} \left. - \frac{J}{R} \frac{D s}{H_1 dx^1} \right\}$ $+ \frac{1}{\Lambda^2 + 2\Lambda \cos \theta_{31} + 1} \left[(\cos \theta_{31} \frac{\partial \Lambda}{H_1 \partial x^1} - \frac{\partial \Lambda}{H_1 \partial x^1}) \right.$ $- \Lambda \left(\frac{\partial \ln H_1}{H_1 \partial x^1} - \cos \theta_{31} \frac{\partial \ln H_1}{H_1 \partial x^1} + \sin \theta_{31} \frac{\partial \theta_{31}}{H_1 \partial x^1} \right)$ $+ \left. \left(\frac{\partial \ln H_1}{H_1 \partial x^1} - \cos \theta_{31} \frac{\partial \ln H_1}{H_1 \partial x^1} + \sin \theta_{31} \frac{\partial \theta_{31}}{H_1 \partial x^1} \right) \right]$	$\left[\frac{W_{\varphi}}{r} \frac{\partial (V_{\varphi r})}{H_1 \partial x^1} + Jg \right.$ $\cdot \left(- \frac{\partial I}{H_1 \partial x^1} + T \frac{\partial s}{H_1 \partial x^1} \right)$ $+ F_1^* \left. \right] + W_1 (\Lambda^2 + 2\Lambda \cos \theta_{31} + 1)$

where the computational formulae for P and Q may be found in Table 1. In the table $\Lambda_1 = W^2/W^3$ represents the ratio of the two velocity components; $M^2 = W^2/a^2$ represents the Mach number of the velocity component W^3 .

The integral form of the continuity equation. The flow quantity of the ^{S₁} stream slab of thickness τ from φ_0 to φ is

$$G = \int_{\varphi_0}^{\varphi} \rho g r W^3 \sin \theta_{31} r d\varphi. \quad (4.2)$$

The velocity gradient equation of the stream surface S_2 is

$$\partial W^3 / H_1 \partial x^1 + P W^3 + Q = 0 \quad (4.3)$$

where P and Q may be found in Table 1; $\Lambda = W^1/W^3$.

The integral form of the continuity equation. The total flow quantity of the stream slab of thick ness τ (from h to t) through ϕ direction is

$$G = \int_h^t \rho g W^3 \tau \sin \theta_{31} H_1 dx^1. \quad (4.4)$$

The fundamental set of equations of viscous gas flowing in turbomachines expressed in non-orthogonal curvilinear coordinates will be published in another paper.

REFERENCES

- [1] Wu Zhonghua: A General Theory of Three-Dimensional Flow in Subsonic or Supersonic Turbomachines of Axial, Radial and Mixed Flow Types, ASME Paper no. 50-A-79, Trans ASME, Nov. 1952, or NACA TN 2604, 1952.
- [2] Wu Zhonghua: Three-Dimensional Turbomachine Flow Equations Expressed with Respect to Non-Orthogonal Curvilinear Coordinates and Methodes of Solution, Paper presented at the 3rd International Symposium on Air Breathing Engines held in March 1976 at Munich.
- [3] Wu Wenguan, Liu Cui: Matrix Solution of the Flow Field Problem of S_1 Stream Surface Using Non-Orthogonal Curvilinear Coordinates and Velocity Components. Journal of Engineering Thermal Physics, Vol. 1, #1, February, 1980.
- [4] Zhu Rongguo: Relaxation Solution of the Inverse Problem Flow Field for the S_2 Stream Surface Using Non-Orthogonal Curvilinear Coordinates and Velocity Components. Journal of Engineering Thermal Physics, Vol. 1, #1, February, 1980.
- [5] Chen Jingyi, Liu Diankui: The General Form of the Equation of Motion of a Turbomachine along a Curve and its Application February, 1976, Institute of Mechanics, Academia Sinica.
- [6] Liu Gaolian: Aerodynamics of Turbomachine, Lecture Note at the Chinese University of Science and Technology, 1964.
- [7] Wu Zhonghua, et. al.: Application of Radial-Equilibrium Condition to Axial-Flow Compressor and Turbine Design, NACA Rep. 955, 1950.

A GENERAL THEORY OF THREE-DIMENSIONAL FLOW IN TRANSONIC TURBOMACHINES WITH SHOCKS*

Xu Jian-zhong
(Academia Sinica)

Abstract

In order to consider the spatial property of a shock in a turbomachine correctly and in accordance with a three-dimensional steady transonic flow, the basic equations on the \bar{S}_1 and \bar{S}_2 stream surfaces in a four-dimensional "space" are derived through expanding the concept of the stream surface to the unsteady case. These equations will be valid for a three-dimensional unsteady flow, too. Applying the characteristic theory to the equations, the characteristic compatibility relations are obtained, and the boundary conditions are established. These equations and boundary conditions with the proper initial conditions entirely define the problem of the transonic flows with shocks on the two kinds of the stream surfaces. Based on the steps of a complete method of solution for the three-dimensional flow suggested in this paper and using a suitable difference scheme the flow may be solved numerically.

1. INTRODUCTION

For solving the subsonic and transonic steady 3-dimensional flow in turbomachines, reference [1] proposed the S_1 and S_2 binary relative stream surface theory, with the basic equations and boundary conditions of the binary stream surface established and the method of solution put forth. In the next two decades, this method was widely applied and verified. In recent years following the development of transonic turbomachines, there is an urgent need for calculating the 3 dimensional flow with spatial shock discontinuity. Based on the integral form of the binary stream surface fundamental equations, it was pointed out in Reference [2], after having derived the relationship among the air stream parameters in front of and behind a spatial shock, that to properly solve this type of 3 dimensional flow, it is necessary to calculate

*This paper has been presented during the Second National Engineering Thermal Physics Conference in Hangzhou, November, 1978.

separately on the binary stream surface the consistent 2 dimensional flow and iterate the binary stream surface calculation.

To establish this type of binary stream surface steady solution problem on the stream surface, one cannot proceed on a specified stream surface due to the 3-dimensionality of the spatial shock. It is necessary to extend the model of the steady stream surface as proposed in Reference [1] to non-steady flow and to merge the 3 dimensional flow* to the binary stream surface in the 4-dimensional "space" including time t . In this paper, we first briefly introduce the non-steady stream surface in this 4-dimensional "space" (or non-constant stream surface) and point out its relationship with each of the corresponding instantaneous 3-dimensional stream surfaces.

Then, in the 2nd and 3rd parts of this paper, the basic equations on the binary stream surface consistent with the 3-dimensional flow are established. They are suitable for both non-steady flow and steady flow with spatial shock. In the 4th part of this paper, we derive the characteristic consistency relationship on the binary stream surface based on characteristic curve theory and propose the set of boundary conditions on the up and down stream boundaries and on the object surface suitable for solving steady state motion. The initial conditions may be given according to the usual method. Thus, the steady solution problem has been completely established.

Lastly, we briefly describe the procedures to solve 3-dimensional flow by iterating the binary non-steady stream surface calculations. We would like to express our gratitude to Professor Wu Zhonghua for his guidance in developing this paper.

*It has been pointed out by Huang Ruixin that the steady stream surface may be extended to non-steady stream surface.

2. THE NON-STEADY STREAM SURFACE AND ITS GEOMETRICAL RELATIONS

/121

A spatial stream surface may consist of the collection of all stream lines through the points on a curve that is not a stream line in a flow field.

In non-steady flows, the stream surface changes with time. In this paper, we shall describe this non-steady stream surface in the 4 dimensional "space" including time t : $\bar{s}(r, \varphi, z, t) = 0$.

Thence,
$$\frac{\partial \bar{s}}{\partial r} dr + \frac{\partial \bar{s}}{\partial \varphi} d\varphi + \frac{\partial \bar{s}}{\partial z} dz + \frac{\partial \bar{s}}{\partial t} dt = 0$$

and its unit normal vector $N(N_r, N_\varphi, N_z, N_t)$ satisfies

$$\frac{N_r}{\frac{\partial \bar{s}}{\partial r}} = \frac{N_\varphi}{\frac{1}{r} \frac{\partial \bar{s}}{\partial \varphi}} = \frac{N_z}{\frac{\partial \bar{s}}{\partial z}} = \frac{N_t}{\frac{1}{U} \frac{\partial \bar{s}}{\partial t}} = \frac{1}{\sqrt{\left(\frac{\partial \bar{s}}{\partial r}\right)^2 + \left(\frac{1}{r} \frac{\partial \bar{s}}{\partial \varphi}\right)^2 + \left(\frac{\partial \bar{s}}{\partial z}\right)^2 + \left(\frac{1}{U} \frac{\partial \bar{s}}{\partial t}\right)^2}}$$

Thus, on the stream surface in the 4-dimensional "space",

$$N_r dr + N_\varphi r d\varphi + N_z dz + N_t U dt = 0,$$

$$\frac{N_t}{N_r} = -\frac{1}{U} \frac{\partial r}{\partial t}, \quad \frac{N_t}{N_\varphi} = -\frac{r}{U} \frac{\partial \varphi}{\partial t} \quad (1)$$

where the dash line in a derivative indicates the partial derivative along the stream surface.

On the other hand, there is a stream surface $s(r, \varphi, z) = 0$, at every instant in 3-dimensional space with its unit normal vector $n(n_r, n_\varphi, n_z)$ as a function of time t . At the same time, according to the definition of the stream surface, we have $n \cdot W = 0$ at every instant.

It should be pointed out that the following relations hold between the unit normal vector of the 3-dimensional spatial stream

surface and the 4-dimensional "spatial" stream surface n and N :

$$N_s/N_r = n_s/n_r, \quad N_s/N_\varphi = n_s/n_\varphi, \quad N_s/N_z = n_s/n_z \quad (2)$$

With the above relations for a non-steady stream surface, we can then merge the basic set of equations of absolute thermal motion for a non-viscous gas expressed in a relative coordinate system rotating with constant angular velocity ω given by Reference [1]

$$\frac{\partial \rho}{\partial t} + \frac{1}{r} \frac{\partial(\rho W_r r)}{\partial r} + \frac{1}{r} \frac{\partial(\rho W_\varphi)}{\partial \varphi} + \frac{\partial(\rho W_z)}{\partial z} = 0 \quad (3)$$

$$\frac{\partial W_r}{\partial t} + W_r \frac{\partial W_r}{\partial r} + \frac{W_\varphi}{r} \frac{\partial W_r}{\partial \varphi} + W_z \frac{\partial W_r}{\partial z} - \frac{V_\varphi^2}{r} = -\frac{1}{\rho} \frac{\partial p}{\partial r} \quad (4)$$

$$\begin{aligned} \frac{\partial W_\varphi}{\partial t} + W_r \frac{\partial W_\varphi}{\partial r} + \frac{W_\varphi}{r} \frac{\partial W_\varphi}{\partial \varphi} + W_z \frac{\partial W_\varphi}{\partial z} + \frac{W_r V_\varphi}{r} + 2\omega W_r \\ = -\frac{1}{\rho r} \frac{\partial p}{\partial \varphi} \end{aligned} \quad (5)$$

$$\frac{\partial W_z}{\partial t} + W_r \frac{\partial W_z}{\partial r} + \frac{W_\varphi}{r} \frac{\partial W_z}{\partial \varphi} + W_z \frac{\partial W_z}{\partial z} = -\frac{1}{\rho} \frac{\partial p}{\partial z} \quad (6)$$

$$\frac{\partial l}{\partial t} + W_r \frac{\partial l}{\partial r} + \frac{W_\varphi}{r} \frac{\partial l}{\partial \varphi} + W_z \frac{\partial l}{\partial z} - \frac{1}{\rho} \frac{\partial p}{\partial t} = 0 \quad (7)$$

onto the non-steady stream surface in binary 4-dimensional "space". It should be explained that as a closed system by equations, besides the above equations, the equation of state for a gas

$$p = \rho RT \quad (8)$$

and the relations

$$dh = C_p dT, \quad l = h + W^2/2 - U^2/2 \quad (9)$$

should be included.

Since these algebraic equations retain their forms on the stream surfaces, we will not specifically describe them in the following sections.

3. BASIC EQUATIONS ON THE NON-STEADY STREAM SURFACE S_1

/122

By extending the definition of the stream surface S_1 in [1] to the 4-dimensional "space", it may be expressed as $\bar{s}_1(r, \varphi, z, t) = 0$. Any function q on this surface may be expressed as

$$q = q(r, \varphi, z, t) = q[r(\varphi, z, t), \varphi, z, t].$$

We notice that in relation (2), the partial derivative of q on the stream surface S_1 may be written as

$$\frac{1}{r} \frac{\partial q}{\partial \varphi} = \frac{1}{r} \frac{\partial q}{\partial \varphi} - \frac{n_z}{n_r} \frac{\partial q}{\partial r}, \quad \frac{\partial q}{\partial z} = \frac{\partial q}{\partial z} - \frac{n_z}{n_r} \frac{\partial q}{\partial r}, \quad \frac{\partial q}{\partial t} = \frac{\partial q}{\partial t} - \frac{UN_r}{N_r} \frac{\partial q}{\partial r} \quad (10)$$

Introducing

$$\frac{\partial \ln b}{\partial t} = \frac{1}{n_r} \left[\frac{n_r}{r} \frac{\partial (W_r r)}{\partial r} + n_z \frac{\partial W_z}{\partial r} + n_z \frac{\partial W_z}{\partial r} \right] + \frac{UN_r}{N_r} \frac{\partial \ln \rho}{\partial r} + \frac{n_z W_z}{n_r r} \quad (11)$$

the continuity equation (3) may be written as

$$\frac{\partial(b\rho)}{\partial t} + \frac{1}{r} \frac{\partial(b\rho W_z)}{\partial \varphi} + \frac{1}{r} \frac{\partial(r b \rho W_z)}{\partial z} = 0 \quad (12)$$

Similarly, equations (4)-(7) may be expressed respectively as

$$\frac{\partial W_r}{\partial t} + \frac{W_z}{r} \frac{\partial W_r}{\partial \varphi} + W_z \frac{\partial W_r}{\partial z} - \frac{V_z^2}{r} = f_r \quad (13)$$

$$\frac{\partial W_z}{\partial t} + \frac{W_z}{r} \frac{\partial W_z}{\partial \varphi} + W_z \frac{\partial W_z}{\partial z} + \frac{iV_z W_z}{r} + 2\omega W_r = -\frac{1}{\rho r} \frac{\partial p}{\partial \varphi} + f_z \quad (14)$$

$$\frac{\partial W_z}{\partial t} + \frac{W_z}{r} \frac{\partial W_z}{\partial \varphi} + W_z \frac{\partial W_z}{\partial z} = -\frac{1}{\rho} \frac{\partial p}{\partial z} + f_z \quad (15)$$

$$\frac{\partial I}{\partial t} + \frac{W_z}{r} \frac{\partial I}{\partial \varphi} + W_z \frac{\partial I}{\partial z} - \frac{1}{\rho} \frac{\partial p}{\partial t} = J \quad (16)$$

where

$$f' = -\frac{1}{n_r \rho} \frac{\partial p}{\partial r} n - \frac{UN_r}{N_r} \frac{\partial W_r}{\partial r}, \quad J = -\frac{UN_r}{N_r} \left(\frac{\partial I}{\partial r} - \frac{1}{\rho} \frac{\partial p}{\partial r} \right) \quad (17)$$

If we consider steady flow, $\partial/\partial t = 0, N_r = 0$, then the above equations become respectively the basic equations (34b), (40), (41), (39a), (39b) and (39c) on the stream surface

S_1 in Reference [1]. In other words, compared to the equations on a steady stream surface S_1 , besides the extra $\frac{\partial}{\partial t}$ term in the non-steady stream surface equations, time related terms $\frac{UN_t}{N_r} \frac{\partial \ln \rho}{\partial r}$ and $\frac{UN_t}{N_r} \frac{\partial W}{\partial r}$, are included in the expression of $\frac{\partial \ln b}{\partial t}$ and f and terms like J appear in the energy equation.

We see that, different from solving the basic equations of transonic flow with shock discontinuity on S_1 stream surface, in the equations (12)-(16), b includes non-steady terms which change with time in the form of $\frac{\partial}{\partial t}$; at the same time in f and J there are effects of non-steady factors. These are results due to the adoption of the model of a non-steady stream surface in 4-dimensional "space" when we derive these equations by treating the 3-dimensionality of shock discontinuity in this paper.

Taking the fact into consideration that in the process of numerical solutions, it is more accurate to use the difference scheme in conservative forms through the shock discontinuity, we transform equations (12)-(16) into the following weak divergence form (corresponding equations may be obtained by using I and S)

$$\frac{\partial(rbp)}{\partial t} + \frac{\partial(b\rho W_n)}{\partial \varphi} + \frac{\partial(rbpW_n)}{\partial z} + \frac{UN_t}{N_r} b\rho = 0 \quad (18)$$

$$\frac{\partial(rbm)}{\partial t} + \frac{\partial}{\partial \varphi} \left(b \frac{mn}{\rho} \right) + \frac{\partial}{\partial z} \left(rb \frac{ml}{\rho} \right) + b \left[\frac{UN_t}{N_r} m - \rho \left(\frac{n}{\rho} + \omega r \right)^2 - r\rho f_r \right] = 0 \quad (19)$$

$$\begin{aligned} \frac{\partial(rbn)}{\partial t} + \frac{\partial}{\partial \varphi} \left[b \left(\rho + \frac{n^2}{\rho} \right) \right] + \frac{\partial}{\partial z} \left(rb \frac{nl}{\rho} \right) - \rho \frac{\partial b}{\partial \varphi} + b \left(\frac{mn}{\rho} + 2\omega r m \right. \\ \left. + \frac{UN_t}{N_r} n - r\rho f_n \right) = 0 \end{aligned} \quad (20)$$

$$\frac{\partial(rbl)}{\partial t} + \frac{\partial}{\partial \varphi} \left(b \frac{nl}{\rho} \right) + \frac{\partial}{\partial z} \left[rb \left(\rho + \frac{l^2}{\rho} \right) \right] - rb \frac{\partial b}{\partial z} + b \left(\frac{n_l}{n_r} \rho + \frac{UN_t}{N_r} l - r\rho f_z \right) = 0 \quad (21)$$

$$\frac{\partial}{\partial t} \left[rbp \left(1 - \frac{p}{\rho} \right) \right] + \frac{\partial(bnl)}{\partial \varphi} + \frac{\partial(rbl)}{\partial z} \quad (22)$$

$$+ r\rho \frac{\partial b}{\partial t} + b\rho \left[\frac{UN_t}{N_r} \left(1 - \frac{p}{\rho} \right) - rJ \right] = 0 \quad (23)-(25)$$

$$m = \rho W_r, \quad n = \rho V_r, \quad l = \rho W_z.$$

4. BASIC EQUATIONS ON THE NON-STEADY STREAM SURFACE S_2

By extending the steady S_2 stream surface in 3-dimensional space to the 4-dimensional "space", it may be written as

$\bar{s}_2(r, \varphi, z, t) = 0$. On this surface any function q may be expressed as $q = q(r, \varphi, z, t) = q[r, \varphi(r, z, t), z, t]$, and the partial derivative on the stream surface may be transformed into

$$\frac{\partial q}{\partial r} = \frac{\partial q}{\partial r} - \frac{n'_r}{n'_{s,r}} \frac{\partial q}{\partial \varphi}, \quad \frac{\partial q}{\partial z} = \frac{\partial q}{\partial z} - \frac{n'_z}{n'_{s,z}} \frac{\partial q}{\partial \varphi}, \quad \frac{\partial q}{\partial t} = \frac{\partial q}{\partial t} - \frac{\omega N'_r}{N'_s} \frac{\partial q}{\partial \varphi} \quad (26)$$

Introducing

$$\frac{d \ln b'}{dt} = \frac{1}{n'_{s,r}} \left(n'_r \frac{\partial W_r}{\partial \varphi} + n'_s \frac{\partial W_s}{\partial \varphi} + n'_z \frac{\partial W_z}{\partial \varphi} \right) + \frac{\omega N'_r}{N'_s} \frac{\partial \ln \rho}{\partial \varphi} + \frac{W_r}{r} \quad (27)$$

we may write the continuity equation (3) as

$$\frac{\partial(b'\rho)}{\partial t} + \frac{\partial(b'\rho W_r)}{\partial r} + \frac{\partial(b'\rho W_z)}{\partial z} = 0 \quad (28)$$

Similarly, equations (4)-(7) are respectively

$$\frac{\partial W_r}{\partial t} + W_r \frac{\partial W_r}{\partial r} + W_s \frac{\partial W_r}{\partial z} - \frac{V_s^2}{r} = -\frac{1}{\rho} \frac{\partial p}{\partial r} + F_r \quad (29)$$

$$\frac{\partial W_s}{\partial t} + W_r \frac{\partial W_s}{\partial r} + W_s \frac{\partial W_s}{\partial z} + \frac{W_r W_s}{r} + 2\omega W_r = F_s \quad (30)$$

$$\frac{\partial W_z}{\partial t} + W_r \frac{\partial W_z}{\partial r} + W_s \frac{\partial W_z}{\partial z} = -\frac{1}{\rho} \frac{\partial p}{\partial z} + F_z \quad (31)$$

$$\frac{\partial I}{\partial t} - \frac{1}{\rho} \frac{\partial p}{\partial t} + W_r \frac{\partial I}{\partial r} + W_s \frac{\partial I}{\partial z} = J \quad (32)$$

where

$$F = -\frac{1}{n'_{s,r}} \frac{1}{\rho} \frac{\partial p}{\partial \varphi} n'_r - \frac{\omega N'_r}{N'_s} \frac{\partial W_r}{\partial \varphi}, \quad J = -\frac{\omega N'_r}{N'_s} \left(\frac{\partial I}{\partial t} - \frac{1}{\rho} \frac{\partial I}{\partial \varphi} \right) \quad (33)$$

Just as the case of the \bar{S}_1 stream surface in steady flow the above equations are transformed into equations (100), (98),

/12

(99a), (96a), (96b) and (96c) in Reference [1]; and the difference between the steady S_2 stream surface and the non-steady \bar{S}_2 stream surface is also similar to the case of the \bar{S}_1 stream surface.

The continuity equation (28) is already at the strong divergence type. The other equations may be transformed into the following weak divergence form (also expressible in terms of I and S):

$$\frac{\partial(b'm)}{\partial t} + \frac{\partial}{\partial r} \left[b' \left(p + \frac{m^2}{\rho} \right) \right] + \frac{\partial}{\partial z} \left(b' \frac{ml}{\rho} \right) - p \frac{\partial b'}{\partial r} \quad (34)$$

$$- b' \rho \left[\frac{1}{r} \left(\frac{n}{\rho} + \omega r \right)^2 + F_r \right] = 0$$

$$\frac{\partial(b'n)}{\partial t} + \frac{\partial}{\partial r} \left(b' \frac{mn}{\rho} \right) + \frac{\partial}{\partial z} \left(b' \frac{nl}{\rho} \right) + b' \left(\frac{mn}{r\rho} + 2\omega m - \rho F_u \right) = 0 \quad (35)$$

$$\frac{\partial(b'l)}{\partial t} + \frac{\partial}{\partial r} \left(b' \frac{ml}{\rho} \right) + \frac{\partial}{\partial z} \left[b' \left(p + \frac{l^2}{\rho} \right) \right] - p \frac{\partial b'}{\partial z} - b' \rho F_z = 0 \quad (36)$$

$$\frac{\partial}{\partial t} \left[b' \rho \left(i - \frac{p}{\rho} \right) \right] + \frac{\partial}{\partial r} (b'ml) + \frac{\partial}{\partial z} (b'll) + p \frac{\partial b'}{\partial t} - b' \rho f = 0 \quad (37)$$

We should point out that the basic equations on a binary non-steady stream surface above are suitable for both solving the non-steady flow and the steady flow with shock. The difference in the solutions of these 2 problems is in different boundary conditions.

5. BOUNDARY CONDITIONS AND INITIAL CONDITIONS

In the previous 2 sections, we have established the hyperbolic partial differential equations on the binary non-steady stream surface. In the following, the corresponding boundary and initial conditions for solving steady motion are given. In initial value — boundary value computations, the parameters, on the object surface and the up and down stream boundaries are related to those in the flow field at a previous instant. Thus, one should derive the characteristic consistency relations according to the characteristic curve theory [3] of hyperbolic equations and then determine the appropriate boundary conditions [4-7].

(1) Boundary conditions on the \bar{S}_1 stream surface.

The following consistency relations may be obtained on the \bar{S}_1 stream surface:

$$\begin{aligned} \frac{\partial p}{\partial t} + \frac{W_u}{r} \frac{\partial p}{\partial \varphi} + W_z \frac{\partial p}{\partial z} - a^2 \left(\frac{\partial \rho}{\partial t} + \frac{W_u}{r} \frac{\partial \rho}{\partial \varphi} + W_z \frac{\partial \rho}{\partial z} \right) \\ = \frac{UN_t}{N_r} \left(a^2 \frac{\partial \rho}{\partial r} - \frac{\partial p}{\partial r} \right) \end{aligned} \quad (38)$$

$$\begin{aligned} \sin \mu \left(\frac{\partial W_z}{\partial t} + \frac{W_u}{r} \frac{\partial W_z}{\partial \varphi} + W_z \frac{\partial W_z}{\partial z} + \frac{1}{\rho} \frac{\partial p}{\partial z} \right) \\ - \cos \mu \left(\frac{\partial W_u}{\partial t} + \frac{W_u}{r} \frac{\partial W_u}{\partial \varphi} + W_z \frac{\partial W_u}{\partial z} + \frac{1}{r\rho} \frac{\partial p}{\partial \varphi} \right) \\ = f'_z \sin \mu - \left(f'_u - \frac{W_r W_u}{r} - 2\omega W_r \right) \cos \mu \end{aligned} \quad (39)$$

$$\begin{aligned} \frac{\partial p}{\partial t} + (W_u \pm a \sin \mu) \frac{1}{r} \frac{\partial p}{\partial \varphi} + (W_z \pm a \cos \mu) \frac{\partial p}{\partial z} \pm \rho a \left(\sin \mu \frac{\partial W_u}{\partial t} + \cos \mu \frac{\partial W_z}{\partial t} \right) \\ \pm \rho a \left[(W_u \sin \mu \pm a) \frac{1}{r} \frac{\partial W_u}{\partial \varphi} + (W_z \cos \mu \pm a) \frac{\partial W_z}{\partial z} + W_z \sin \mu \frac{\partial W_u}{\partial z} \right. \\ \left. + \frac{W_u}{r} \cos \mu \frac{\partial W_z}{\partial \varphi} \right] = \rho a^2 c \pm \rho a (f'_z \cos \mu + f'_u \sin \mu) \end{aligned}$$

$$\mp \rho a W_r \left(\frac{W_u}{r} + 2\omega \right) \sin \mu + \frac{UN_t}{N_r} \left(a^2 \frac{\partial \rho}{\partial r} - \frac{\partial p}{\partial r} \right) \quad (40)-(41)$$

where μ represents the angle between the z axis and the exterior normal at a point on the boundary. Equations (38) and (39) are the flow characteristic consistency relations, while (40) and (41) are respectively the wave characteristic consistency relations of propagation with velocity $-a$ and $"a"$ relative to the gas.

For the upstream boundary: When the meridional plane velocity $W_{1,0} < a$, only (40) may be used. Thus 3 parameters need be specified and the other parameter should be derived from (40). Notice that now $\mu = \pi$, and the 3 specified parameters (e.g., p_0, T_0 and air stream angle) do not vary with time while the parameters are all uniform along the φ direction. Equation (40) will be greatly simplified.

For the down stream boundary: Here, if the outlet air stream is subsonic, then eg. (38), (39) and (41) are usable consistency relations. We need to specify another parameter (i.e. the reverse

pressure p). Notice that $\mu = 0$ and the 3 equations above may be greatly simplified. If the outlet air stream is transonic, the 4 consistency relation can all be used and no parameters can be specified.

For the blade surface: The relations (38), (39) and (41) can all be used. The specified condition is that the stream velocity should be tangential to the surface.

Besides, there is still the periodic condition for the \bar{S}_1 stream surface calculation which may proceed in a way similar to an interior point. Of course, when the shock extends beyond the passage way, we need to analyse more concretely whether to choose periodic conditions for pressure surface or for suction surface.

(2) Boundary conditions on the \bar{S}_2 stream surface.

Similarly the consistency relations now are

$$\begin{aligned} \frac{\partial p}{\partial t} + W_r \frac{\partial p}{\partial r} + W_z \frac{\partial p}{\partial z} - a^2 \left(\frac{\partial p}{\partial t} + W_r \frac{\partial p}{\partial r} + W_z \frac{\partial p}{\partial z} \right) \\ - \frac{\omega N'_t}{N'_s} \left(a^2 \frac{\partial p}{\partial \varphi} - \frac{\partial p}{\partial \varphi} \right) \end{aligned} \quad (42)$$

$$\begin{aligned} \sin \mu' \left(\frac{\partial W_r}{\partial t} + W_r \frac{\partial W_r}{\partial r} + W_z \frac{\partial W_r}{\partial z} + \frac{1}{\rho} \frac{\partial p}{\partial z} \right) - \cos \mu' \left(\frac{\partial W_r}{\partial t} + W_r \frac{\partial W_r}{\partial r} \right. \\ \left. + W_z \frac{\partial W_r}{\partial z} + \frac{1}{\rho} \frac{\partial p}{\partial r} \right) = F_s \sin \mu' - \left(F_s + \frac{V_s^2}{r} \right) \cos \mu' \end{aligned} \quad (43)$$

$$\begin{aligned} \frac{\partial p}{\partial t} + (W_r \pm a \sin \mu') \frac{\partial p}{\partial r} + (W_z \pm a \cos \mu') \frac{\partial p}{\partial z} \pm \rho a \left(\sin \mu' \frac{\partial W_r}{\partial t} + \cos \mu' \frac{\partial W_r}{\partial t} \right) \\ \pm \rho a \left[(W_r \sin \mu' \pm a) \frac{\partial W_r}{\partial r} + (W_z \cos \mu' \pm a) \frac{\partial W_r}{\partial z} + W_r \cos \mu' \frac{\partial W_r}{\partial r} \right. \\ \left. + W_z \sin \mu' \frac{\partial W_r}{\partial z} \right] = \rho a^2 \left(c' - \frac{W_r}{a} \right) \pm \rho a F_s \cos \mu' \pm \rho a \left(F_s + \frac{V_s^2}{r} \right) \sin \mu' \\ + \frac{\omega N'_t}{N'_s} \left(a^2 \frac{\partial p}{\partial \varphi} - \frac{\partial p}{\partial \varphi} \right) \end{aligned} \quad (44)-(45)$$

where μ' represents the angle between the z axis and the exterior normal at a point on the boundary. Equations (42) and (43) are the

flow characteristic consistency relations while (44) and (45) are, respectively, the wave characteristic consistency relations with propagation velocity $-a$ and a relative to the gas.

For up stream boundary: When $W_{1,2} < a$, only (44) applies. Thus, 3 parameters need be specified with the other parameter derived from (44). Notice that now $\mu' = \pi$ and the 3 specified parameters (e.g. $P, T,$ and M number) do not vary with time, while the parameters along the 4 direction are all uniform. E.g. (44) will be greatly simplified.

For down stream boundary: Now if the outlet air stream is subsonic, then (42), (43) and (45) are usable consistency relations. One parameter needs by specified (e.g. inverse pressure p or $V_{x,r}$). Notice that now $\mu' = 0$ and the above 3 equations will also be greatly simplified. If the outlet air stream is transonic, the 4 consistency relations can all be used and no parameters can be specified.

For wall surface: (42), (43) and (45) all apply. The specified boundary condition is that the air stream velocity should be tangential to the wall surface.

/126

(3) Initial conditions

It has been proved in theory [8] that the choice of initial conditions does not affect the final steady state solution. But, if the choice is not proper at all, then an excessive oscillation may be induced and the stability of the numerical solution will be destroyed. Also, the choice of initial conditions will affect the speed of reaching stable solutions. Taking these factors into consideration, one may choose the subsonic solution or the parameter distribution that satisfies the continuity equation on the geometrical center line while smoothly varying elsewhere as the initial condition.

6. PROCEDURES FOR A COMPLETE SOLUTION OF 3-DIMENSIONAL FLOW

In the above we have transformed the problem of solving steady state 3-dimensional flow with shocks in turbomachines into the initial boundary value problem for 2 families of 3 variable hyperbolic equations, and suggested the way to specify initial and boundary conditions. From these we have completely established the problem of finding solutions on the binary non-steady stream surface in 4-dimensional "space". To obtain the solution to the 3-dimensional problem, besides obtaining respectively the stable solutions of the initial value-boundary value problem on the 2 families of stream surfaces, it is also necessary to iterate them until convergent.

To save time, the solution process may adopt the method of both time step and stream surface iteration: After each time step Δt , or several steps $\Sigma \Delta t$, an iteration of the 2 stream surface families is carried out, i.e., taking the result of each stream surface calculation and the shape of the 4-dimensional stream surface [e.g. (1)] and using them in the calculation of the next time step length for the other stream surfaces. This is re-cycled whether the solution in each calculation has reached stability or not. When a stable solution is approached at each time step length one must iterate the stream surfaces. Finally, when a stable solution is obtained on each stream surface, the final solution for the whole 3-dimensional flow is found. This solution procedure clearly shows that transonic flow with shock cannot be solved on a specified stream surface as pointed out in Reference [2]. In other words, it is precisely through the continuous adjustment of the stream surface position and shape during the solution process that one can obtain the 2-dimensional shock in agreement with the spatial shock on the binary stream surface. The above solution procedure closely correlates the calculated shock on a single stream surface and the spatial approximation of the shock which shortens the time required to reach a stable solution.

7. CONCLUSIONS

Based on the extension of the stable stream surface model in 3-dimensional space to the unstable stream surface in 4-dimensional "space", in this paper we transformed the partial differential equations of non-viscous gas absolute thermal motion in turbomachines into the binary non-steady stream surfaces \bar{S}_1 and \bar{S}_2 , and established the corresponding basic equations. Compared to the equations on stable stream surfaces, in these equations, there is a contribution to b (or b') and "stream slab force" due to the shape of non-steady stream surface, besides the partial derivatives which include the thickness of the stream slab in 4-dimensional "space". In the energy equation related terms J (or J') also appear. These equations are suitable for both 3-dimensional non-steady flow and steady flow with shocks.

It should be pointed out that the equations for solving transonic flow on stream surfaces (mainly surface of revolution) in both domestic and foreign references are all established on steady stream surfaces that do not vary with time. The thickness of the stream slab is also independent of time. Hence, the shock thus calculated is not part of the real spatial shock. In fact, the basic equations in these references are not obtained from the basic equations for solving spatial shocks. Their results fail to consider the close relationship between stream surfaces of the same family and between the stream surfaces of the 2 families induced by the 3 dimensionality of the shock.

According to characteristic theory, we have derived the characteristic consistency relation on binary stream surfaces and the boundary conditions for steady flow. After suitably choosing the initial conditions, the problem of finding solutions for transonic flow with shocks on binary stream surfaces is completely established.

Taking into consideration the tight correlation between stream surfaces with shocks, for obtaining the solution of 3-dimensional flow, we may use the method of simultaneous time step and stream surface iteration. It can save computation time. Thus, one may find the numerical solution after suitably selecting the difference scheme.

REFERENCES

/127

- [1] Wu Chung-hua: A general theory of three-dimensional flow in sub-sonic and supersonic turbomachines of axial, radial, and mixed-flow types, ASME paper 50-A-79, Trans. ASME, Nov. 1952, or NACA TN 2604, 1952.
- [2] Xu Jianzhong: Shock Relations in Turbomachines. Journal of Mechanical Engineering, Vol. 15, #3, 1979.
- [3] Courant R. and Hilbert D.: Methods of mathematical physics, vol. II, Interscience, 1962.
- [4] Gang A. and Serra R.: Boundary conditions and uniqueness in internal gas dynamic flows, AIAA J., vol. 12, No. 3, Mar. 1974, p. 263.
- [5] Gopalakrishnan S. and Bozzola E.: Numerical representation of inlet and exit boundary conditions in transient cascade flow, ASME paper 73-GT-55.
- [6] Борода А. Б., Замфорт Б. С., Назнов М. Я. и Крайнов А. Н.: Об использовании процесса установления по времени при решении задач стационарного обтекания газом решеток профилей, Механика Жидкости и Газы, №. 4, 1974, стр. 118.
- [7] Veuillet J.-P.: Calcul numérique de l'écoulement transsonique d'un fluide parfait dans une grille d'aubes, La Recherche Aéronautique, No. 6, 1975, p. 327.
- [8] Lax P.: Weak solutions of nonlinear hyperbolic equations and their numerical computation, Comm. Pure Appl. Mech., Vol. 7, No. 1, 1954, p. 159.

AN EXPERIMENT TO IMPROVE THE SURGE MARGIN BY USE OF CASCADE WITH SPLITTER BLADES

Tsui Chih-ya, Zhou Sheng, Lu Ren-fu, Zhang Lian-chi
(Beijing Institute of Aeronautics and Astronautics)

Abstract

Through experimental comparison on a basis of equal profile sectional area per unit frontal length, which implies a basis of equal weight, a cascade with splitter blades is found to give a maximum deflection 3.5 degrees greater than an ordinary cascade tested. The corresponding incidence angle is 6.5 degrees greater, thus markedly improving the surge margin. The nominal deflection and thus work addition ability also increase.

Prediction is also made on a basis of equal solidity that the use of splitter blades would give about the same nominal work addition ability as an ordinary cascade, but weight is substantially reduced to 70% approximately.

1. FORWARD

It is well known that the maximum deflection may be increased by increasing the solidity of the pressure-resisting cascade, hence improving the surge margin; however, the weight also increases and the efficiency decreases due to greater flow resistance. The basic mechanism is mainly due to the fact that with a high solidity and closer blade separation, the pressure difference decreases when the same air stream turns and the minimum pressure at the rear side of the blades together with the reverse pressure gradient is more gradual, so that separation will only occur at higher attack angle and rotation angle, hence the increase in maximum angle of rotation and surge margin.

It often happens that the minimum pressure point of a low speed cascade blade back shifts forward. This offers a clue. But, then why should the solidity be increased along the entire

*This paper has been presented in November, 1978 at the Second National Engineering Thermal Physics Conference in Hangzhou.

blade chord?

In this investigation, we want to study: for a cascade with splitter blades which has the same profile sectional area per unit frontal length as an ordinary cascade (Figure 1) i.e.

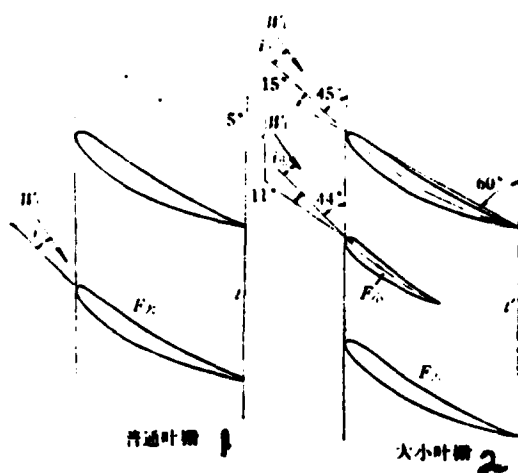


Figure 1. Ordinary cascade and cascade with splitting blades.

Key: 1--ordinary cascade;
2--cascade with splitting blades.

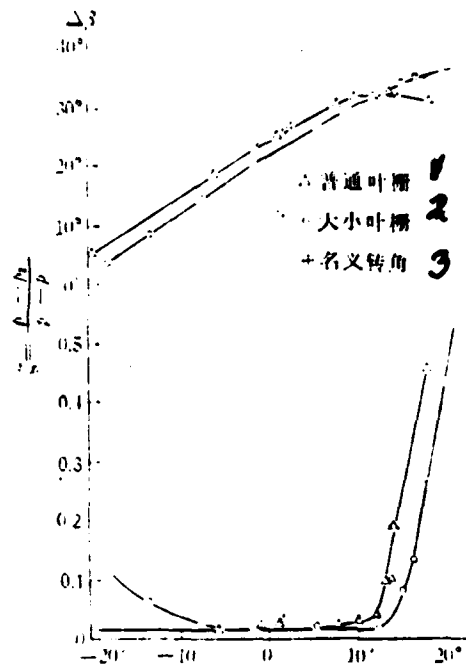


Figure 2. The attack angle characteristics of 2 types of cascade.

Key: 1-- Δ ordinary cascade;
2-- \circ cascade with splitting blades;
3-- $+$ angle of rotation.

$$\frac{F_{*} + F_{*}}{l'} = \frac{F_{*}}{l}$$

/129

whether the maximum angle of rotation and the corresponding angle of attack will increase for the same weight of the blades.

2. EXPERIMENTAL SET-UP

The experimental horizontal type cascade test outlet 120 X 490, and front blade $M_1 = 0.3$, $Re = \delta W_1 / \nu = (2.5-4) \times 10^5$. The middle section 40mm blade front and rear total static pressure non-uniformity is less than 1.5% and the non-uniformity of the blade front and rear air stream angle is less than 1° . The periodicity of the 3 central channels along the cascade distance is good, which provides reliability for the comparison study.

The ordinary cascade consists of 10 blades with blade type 10C4/30C50, chord length 60mm, cascade distance 46.2mm (solidity 1.30), angle of incidence 60° and is made of glass epoxy with an epoxy coating.

Two blades are removed from the ordinary cascade and replaced by 7 small 131 blades with chord 36mm, inserted uniformly. The distances from the end to the large blades on the 2 sides are both 31.4mm. The angle between the blade chord and the large blade chord is 5° which makes the angle of attack $i_{\text{small}} = i_{\text{large}} - 1^\circ$. The 1 dimensional divergence angles on the 2-side channels are approximately equal. The small blade is made of aluminum or brass.

When the 4-hole sensing head is adjusted in the 32 m/s wind tunnel, the error in the total pressure 1.5%, the error in static pressure 4.3% and the error in the direction 0.25° . The positions of measurement are respectively at 2 chord lengths in front of the cascade and one chord length behind the cascade. Measurements at many points along the cascade are averaged. Pressure distribution is measured at the central cross-section of the central blade.

3. RESULTS AND DISCUSSIONS

The characteristics of the attack angles of the 2 cascades are shown in Figure 2. The typical blade surface pressure distribution $\bar{p} = \frac{p - p_\infty}{p_0 - p_\infty}$ is shown in Figure 3 a,b,c,d.

Compared to that of the ordinary cascade, the maximum angle of rotation of the cascade with splitting blades is 35.3° , i.e. 3.5° more, and the angle of attack is 19.8° , i.e., 6.5° more. Although the loss coefficient ζ of 0.435 is .103 larger than that of the ordinary cascade due to the increase of frictional surface and of wake mixing, yet the separation is apparently delayed and surge margin improved. The tendency of the pressure distribution curve is also concrete evidence. As pointed out by the experiment in Reference [1], the larger the axial flow is than $W_{L\gamma_1}/W_{L\gamma_2}$, the greater will be the reverse pressure gradient on the back side of the blade and the easier will the air stream separate. Now $\frac{W_b}{W_\infty} = 0.780$ at maximum angle of rotation for the cascade with splitting blades is slightly greater than $\frac{W_b}{W_\infty} = 0.745$ at maximum angle of rotation for the ordinary cascade which demonstrates that when compared according to the same flow ratio, the advantages of the cascade with splitting blades will be slightly enhanced.

The nominal angle of rotation for the ordinary cascade $\Delta\beta^* = 0.8 \times 31.8 = 25.5^\circ$. Here $i^* = 2.5^\circ$, $\beta_1^* = 42.5^\circ$, $\beta_2^* = 68^\circ$. From the curve for synthetic nominal angle of rotation according to this β_2^* and solidity 1.3 (as in Reference [2]), $\Delta\beta^*$ is also 25.5° , just as in our experiment.

The nominal angle of rotation for the cascade with splitting blades $\Delta\beta^* = 0.8 \times 35.3 = 28.3^\circ$, which is 2.8° greater than that of the ordinary cascade. The loss coefficients, however, are basically the same as can be seen from Figure 2. Hence, the work addition capability of the nominal angle of rotation is also improved.

Another very meaningful comparison may be predicted. If we replace the small blades with large ones, then the solidity $\frac{60}{31.4} = 1.9$. The airstream off-path angle may be found by using the empirical formula

$$\beta^* = (75^\circ - 68^\circ) \sqrt{\frac{1.3}{1.9}} = 5.8^\circ$$

/131

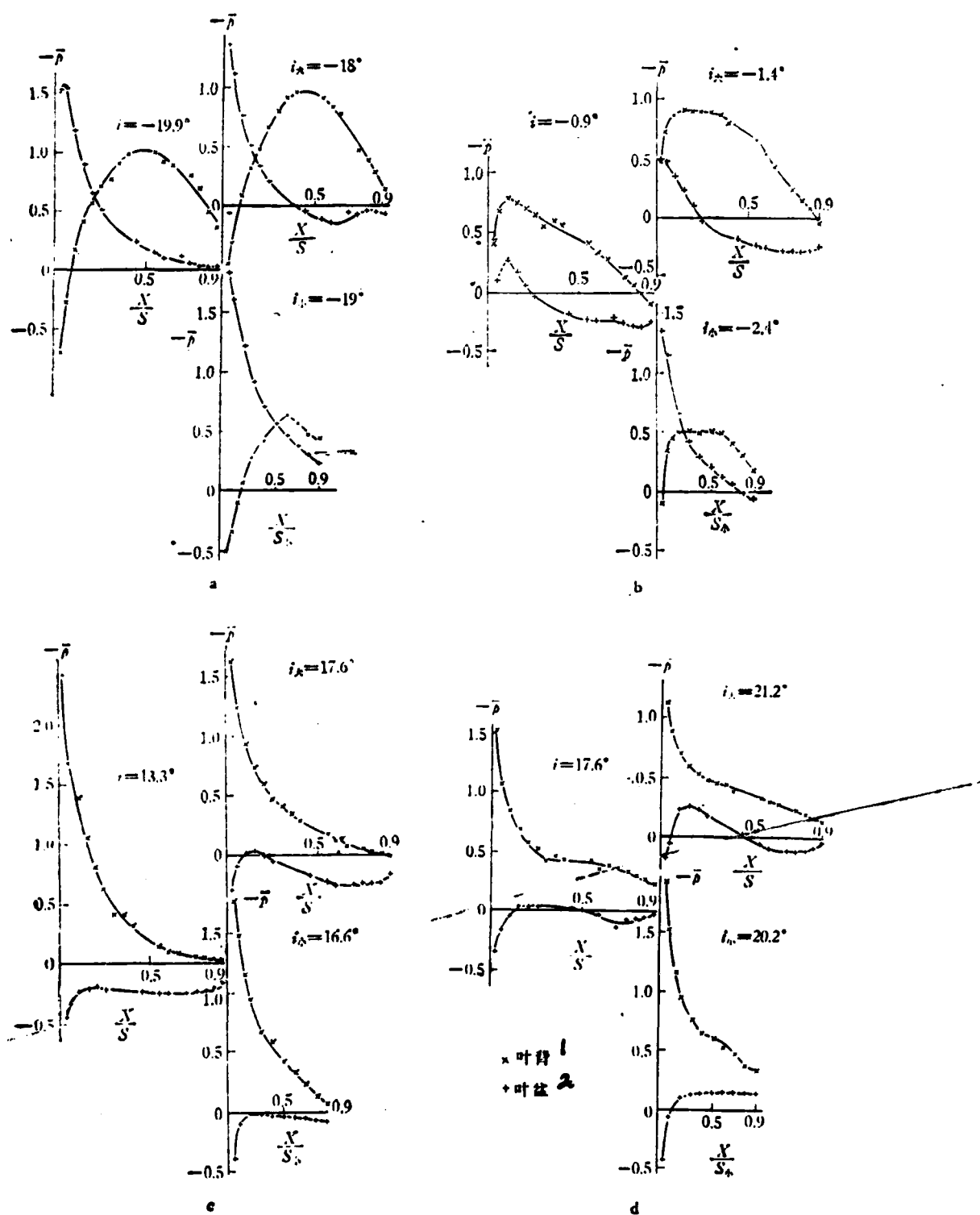


Figure 3. Comparison of pressure distributions on blade surface.

Key: 1--x back of blade; 2--+ bowl of blade.

i.e. $\beta_1^* = 75^\circ - 5.8^\circ = 69.2^\circ$

. From Reference [2], we find

$\Delta\beta^* = 29.5^\circ$, close to that for the cascade with splitting blades, while the cross-section (or weight) of the cascade with splitting blades reduction ratio is $(10^3 + 6^3):(10^3 + 10^3) = 0.68$.

This has raised some new questions: Is it possible that by changing every other blade in an ordinary cascade which has been in use for years to a small one, the work addition will remain the same, while the weight and cost will be much reduced?

The only experiment independently carried out in the sixties is in Reference [3]. They tried to use small blades at different positions in the middle, or rear, of the passage, but the chord length is only 25% of that of the big blade. The practicality of technology and strength is far inferior to that in our paper. The characteristics of the attack angle are not given, and the pressure distribution of the small blade is not measured.

In the seventies, Reference [4,5] experimented with supersonic extended pressure cascades with small blades added from axial chord length 50% to rear edge. At air intake Mach number about 1.46, the air outlet angle is made to be 8-9% closer to the axis, but the loss is increased to 25%. In Reference [6], a supersonic compressor is designed with small blades added in the rear half of the passage to reduce the air outlet, off-path angle of the rotor, and to strive toward a single stage, total pressure ratio of 3.0. There is a preliminary report (Reference [7]), but the intention there, is apparently different from our paper.

All in all, our study is only a comparison experiment at low speed for cascade distance, angle of bending, angle of attack, relative size and position of the small blade. The result is encouraging. It is necessary to further develop experiments to compare things in more detail so as to provide a practical reference in the design for compressors.

REFERENCES

- [1] U. Stark: VDI Bericht Nr. 193'1973, Effect of Cascade Front and Rear Axial Velocity Ratio on the Aerodynamic Parameters of Plane Compressor Cascade with Frictional Flow.
- [2] IO. C. et. al.: Theory and Computation of Axial Flow and Centrifugal Compressor. Mashgiz, 1957.
- [3] O. Scrofanì: VKI TN IN-18 1966. Improving Flow in Speed-Reducing Blades with Large Bending By Using Auxilliary Cascades.
- [4] R.L. Holtman: AD774454. Experiment on Supersonic Compressor Cascade with Splitting Blades Plus Vortex Generator, 1973.
- [5] R.L. Holtman: AD774549. Experiment on Supersonic Compressor Cascade with Splitting Blades, 1973.
- [6] A.J. Wennerstrom: AD786025. Design of Rotor with Small Blades in High Pressure Ratio Supersonic Axial Flow Compressor Stage, 1974.
- [7] A.J. Wennerstrom: AD-A014732/2GA. Experiment on Supersonic Axial Flow Compressor Stage Having Rotor with Some Small Blades, 1975.

THE PERFORMANCE CALCULATION OF AN AXIAL FLOW COMPRESSOR STAGE

Zhang Yu-jing

Abstract

Based on the simplified two-dimensional flow equations, the computer program for the direct problem is developed. By means of this program several subsonic axial flow compressor stages are calculated. The calculated results are compared with experimental data. This calculation method is evaluated and problems to be solved in the performance calculation are presented.

1. FORWARD

The calculation of the axial flow compressor problem means the calculation of compressor characteristics when all the geometrical parameters of the compressor are known. This kind of calculation is important and meaningful whether to determine the combined operation line of the compressor and the turbine, or to understand the properties of the rotatable airfoil. If the characteristics can be computed with good enough accuracy, then less effort can be spent on testing and adjusting or tuning the compressor. Because of our research on the attached surface layer, the surge and the properties of the cascade, etc. are not enough. Therefore, the compressor characteristics are still estimated approximately, or obtained from experiment. There are many problems requiring further studies in the method of calculating the characteristics of the whole machine based on the binary relative flow surface theory [1,2]. There is still a considerable distance before actual engineering applications of that method. However, this is a general method

* This paper was presented at the 2nd National Engineering Thermodynamics Conference at Hangzhou in November, 1978.

to understand the gas flow inside the compressor, and is the direction in which the computation of compressor characteristics moves.

To study problems in this area, we developed a computer program in 1975 for the compressor problem, carried out some calculations for some subsonic compressor stages, and compared the computational results to the current experimental results. This was a preliminary attempt to calculate the characteristics with the simplified 2 dimensional flow method. Thus, we did not place as much weight on the equations themselves, and instead we concentrated on such problems as the convergence rate in the calculation, the effect of the wrong choice of some empirical laws (e.g. determination of the reference attack angle) in the design and in the computation, etc. This made us realize that, in order to obtain reliably computed characteristics, one must have complete information on the accurate cascade reference attack angle and the corresponding angle of lag, as well as the computational method for the cascade characteristics under reasonable work conditions. These two aspects are more important than an accurate loss model.

According to the results of calculations in this paper, it is feasible to use the computational method for subsonic compressor stage characteristics. Further computations and experimental verification are needed for making calculations on the whole compressor.

2. BASIC ASSUMPTIONS AND EQUATIONS

In this calculation, we assume the flow to be stable, axial symmetric and adiabatic. The fluid is perfect; viscosity is neglected but the change in the entropy due to it is taken into consideration. The rotating angular speed of the rotor is constant. This greatly simplifies the problem.

In the (r, φ, z) coordinate system, the continuity equation and equation of motion are respectively /133

$$\frac{1}{r} \frac{\partial(\rho W_r r)}{\partial r} + \frac{\partial(\rho W_z)}{\partial z} = 0 \quad (1)$$

$$W_r \frac{\partial(c_u r)}{\partial r} + W_z \frac{\partial(c_u r)}{\partial z} = 0 \quad (2a)$$

$$W_r \frac{\partial W_r}{\partial r} + W_z \frac{\partial W_r}{\partial z} - \frac{c_u^2}{r} = - \frac{g_0}{\rho} \frac{\partial p}{\partial r} \quad (2b)$$

$$W_r \frac{\partial W_z}{\partial r} + W_z \frac{\partial W_z}{\partial z} = - \frac{g_0}{\rho} \frac{\partial p}{\partial z} \quad (2c)$$

The energy equation is:

$$\text{Flowing through a moving airfoil: } DI/Dt = 0 \quad (3)$$

$$\text{Flowing through a stationary airfoil: } DH/Dt = 0 \quad (3')$$

The equation of state is

$$p = \rho RT \quad (4)$$

According to the continuity equation, equation of motion, and the equation of state, we can derive the radial equation of motion:

$$\begin{aligned} \frac{g_0}{\rho} \frac{\partial p}{\partial r} = & \left(\frac{1 - M_m^2}{1 - M_m^2} \right) \left(\frac{c_u^2}{r} + \sec^2 \varphi \frac{c_z^2}{r_m} \right) + \frac{c_z^2 \tan \varphi}{1 - M_m^2} \frac{\partial(r \tan \varphi)}{r \partial r} \\ & - \frac{c_r}{1 - M_m^2 c_p} \frac{1}{Df} \frac{Df}{Dt} \end{aligned} \quad (5)$$

This is e.g. (31) of Reference [3] which has taken into account the entropy change.

To make the computation easier, we introduce the stream line parameter A, $A = 1 + \tan^2 \varphi + \tan^2 \beta$,

Here $\tan \beta = W_z / W_r$.

Equation (5) may be written as follows:

$$\begin{aligned} \frac{\partial W_z^2}{\partial r} = & \frac{2g_0}{A} \left\{ \frac{\partial l}{\partial r} - T \left[\frac{\partial s}{\partial r} - (k-1) \frac{M_m^2}{1-M_m^2} \sin \varphi \frac{\partial s}{\partial m} \right] + \frac{\omega^2 r}{g_0} \right\} \\ & - \frac{2W_z^2}{A} \left\{ \frac{1}{2} \frac{\partial A}{\partial r} + \frac{1}{1-M_m^2} \left[(1-M_m^2) \left(\left(\frac{\omega r}{W_z} - \tan \beta \right)^2 / r + \frac{\sec^2 \varphi}{r_m} \right) \right. \right. \\ & \left. \left. + \frac{\tan \varphi}{r} \frac{\partial(r \tan \varphi)}{\partial r} \right] \right\}. \end{aligned} \quad (6)$$

For the computational cross-section behind a stationary airfoil, it is only necessary to take $l = H, \omega = 0, \beta = \alpha$.

Eq. (6) is the radial equation of motion which is to be solved in the characteristic calculation.

3. SOLVING THE EQUATIONS

We use the iteration method to solve the equations. Some explanations of the problem in the solution are as follows:

1. Initially when the stream line is assumed, the radial point is determined according to the equal ring surface.

2. When φ and r_m are calculated, the shape of the stream line is taken to be a cubic function. In each stage of the calculation, there are 3 known positions for the cross-sectional area computational points. The boundary is taken to be at the compressor outlet and in front of the inlet airfoil. The boundary conditions are: in front of the inlet airfoil, $(dr/dz)_{\text{along stream line}} = 0$, at the outlet of the compressor, $(dr/dz)_{\text{along stream line}} = 0$.

3. Computation of the reference attack angle is based on the principle in Reference [4], but the original airfoil type of the sample compressor is A40. Due to the lack of experimental data, we assume temporarily the reference attack angle to be 2° smaller than that of the NACA-65 series of airfoils.

4. The angle of lag the reference attack angle is also computed according to the principle in Reference [4]. When the

/134

attack angle deviates from the reference attack angle, the change in the angle of lag may be corrected according to the principles of Reference [5]. The corrected curve is as shown in Figure 1.

5. Below the reference attack angle, the loss calculation is based on the principles of Reference [4] — namely, calculating the loss with the pressure expansion factor and relative blade height as parameters. When the attack angle deviates from the reference attack angle, the loss is also calculated according to the principles of Reference [5]. The increase in entropy may be calculated according to the following equation from the total pressure loss coefficient $\bar{\omega}$:

$$\frac{\Delta s}{R} = \ln \left\{ 1 - \left\{ 1 + \frac{k-1}{2} \bar{\omega}^2 \left[\frac{(r_{i,i}^2 - r_{i-1,i}^2)}{k g_0 R T_{p,i-1,i}} \right] \right\}^{-\frac{k}{k-1}} \right. \\ \left. \cdot \omega \left[1 - \left(1 + \frac{k-1}{2} M_{i,i}^2 \right)^{-\frac{k}{k-1}} \right] \right\}^{-1}$$

Where ω is the angular velocity of the rotor, $T_{p,i-1,i}$ is the relative stagnant temperature of the preceding cross-sectional area. For a stationary airfoil: $\omega = 0$, we get

$$\frac{\Delta s}{R} = \ln \left\{ 1 - \omega \left[1 - \left(1 + \frac{k-1}{2} M_i^2 \right)^{-\frac{k}{k-1}} \right] \right\}^{-1}$$

6. The effect of the inner and outer wall boundary layers on the flow is taken into account by coefficient KB. And in this calculation, the first stage KB is taken to be 0.99, the second stage 0.98, for the 3rd stage and beyond 0.96, and kept constant.

7. When calculating the characteristics properties of a level, the mean value of the level is calculated according to the flow rate mean value for parameters at various streamlines.

4. COMPUTATIONAL PROCESS

For our sample calculation, since $(k-1)\sin\varphi \cdot M_{\infty}^2/(1-M_{\infty}^2)$ is far less than 1, by assuming $\partial s/\partial r$ and $\partial s/\partial m$ as quantities of the same order, then the $\partial s/\partial m$ term may be neglected. After Eq. (6)

is dispersed we get:

$$W_{i,i+1}^1 = WW - (2g_0/l_i)T_i(s_{i+1} - s_i)$$

where

$$\begin{aligned} WW = W_{i,i}^1 + \frac{2g_0}{A} \left[(l_{i+1} - l_i) + \frac{\omega^2 r_i}{g_0} (r_{i+1} - r_i) \right] \\ - \frac{2W_{i,i}^1}{A_i} \left\{ \frac{1}{2} (A_{i+1} - A_i) + \frac{1}{1 - M_{m,i}^2} \left[(1 - M_{i,i}^2) \left(\left(\frac{\omega r_i}{W_{i,i}} - \tan \theta_i \right)^2 / r_i \right. \right. \right. \\ \left. \left. \left. + \sec^2 \theta_i / r_{m,i} \right) (r_{i+1} - r_i) + \frac{\tan \theta_i}{r_i} (r_{i+1} \tan \theta_{i+1} - r_i \tan \theta_i) \right] \right\}. \end{aligned}$$

When calculating along the radial direction, we first assume the axial velocity for the root cross-section area, and gradually calculate toward the head section to find W_z and ρ of each point. When the whole cross-section is calculated, the flow rate is obtained by integration. If the flow rate does not satisfy the requirement, then the root velocity is corrected. The correction formula is

$$W_{i,i}^{(n+1)} = W_{i,i}^{(n)} \{ 1 - k_g [(G^{(n)} - G_0)/G_0] \}$$

where k_g is the iteration factor of the flow rate iteration. When the flow rates of each cross-sectional area are all satisfactory, then stream line iteration is carried out. During stream line iteration, the correction formula for the stream line radial position is

$$r_{i,j}^{(n+1)} = r_{i,j}^{(n)} + k_r (\bar{r}_{i,j}^{(n+1)} - r_{i,j}^{(n)})$$

Where $r_{i,j}^{(n)}$: is the radial position of the stream line at the n iteration, $\bar{r}_{i,j}^{(n+1)}$: the current value of the stream line radial position, $r_{i,j}^{(n+1)}$: the radial position of the stream line at the $n + 1$ iteration, and k_r is the stream line iteration factor.

In this calculation, we take the relative error satisfied by the flow rate and stream line to be 10^{-3} . /135

5. DISCUSSIONS

We carried out computations for subsonic compressor stages with the computer program. Two of the sample calculations have the flow through part shown in Figure 2 and Figure 8. The low speed experimental results for the stage as shown in Figure 2 are given in Reference [6]. We discuss below several problems based on the computed results.

1. Loss model: To obtain results in conformity with practical results, one must have a reasonable loss model. Here we choose the loss model given in Reference [5]. The loss given in Reference [7] and [4] is larger than that in Reference [5], especially in the head section. For single stage test compressor (channel shown in Figure 2), the stage characteristics calculated according to the loss model in Reference [5] and [7] are shown in Figure 3. Generally speaking, under an ordinary attack angle, although the effect of these two loss models on efficiency and pressure ratio is not large, it is still apparent. From the comparison before, we know that the effect of the loss model on the characteristics is weaker than that of other factors.

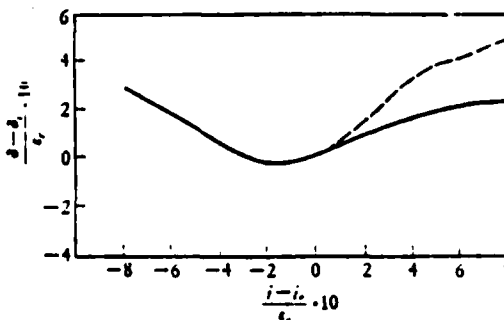
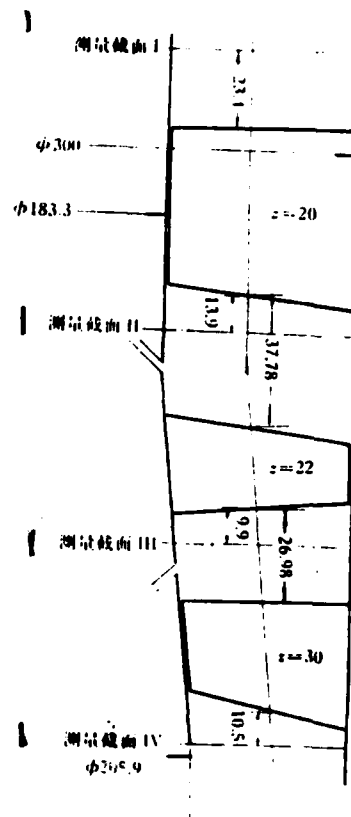


Figure 1. Calculation of the angle of lag under varying working conditions. The solid line is from Reference [5]. The dashed line is the correction to Reference [5]
 $M = 0.5 \sim 1.1$, the subscript r is the reference work condition parameter.

Figure 2. Diagram of single stage test compressor flow channel and measured cross-section.

Key: 1--measured cross-section.



2. The reference angle of attack and the angle of lag under the reference angle of attack: The effect of these 2 factors on the computed results of the stage characteristics is shown in Figure 3. From the diagram, it can be seen that the unsuitable choice of reference angle of attack has a greater effect on efficiency, and the angle of lag affects both pressure ratio and efficiency, significantly, and its effect on the stage characteristics is far greater than that on efficiency. Hence, only by determining accurately the reference attack angle of the cascade and its corresponding angle of lag will realistic characteristics be found.

3. Convergence of stream line iteration: For different stream line iteration factors, the number of iterations satisfying the same accuracy vary widely. For simple stage test compressor, when $k_r = 0.1$, 54 iterations are needed to satisfy an accuracy of 10^{-4} while for $k_r = 0.4$, only 13 iterations are needed. For subsonic stages with a flow channel which is not too steep, within a wide range, all iteration factors are convergent, but when the

flow channel shape varies more greatly, the iteration factor needs to be chosen small to guarantee stability. Thus, selection of the stream line iteration factor should be determined by the change in stream line and the combination of various parameters (such as slope, curvature, etc.). Hence, varying the iteration factor to affect iteration seems to be more effective.

/136

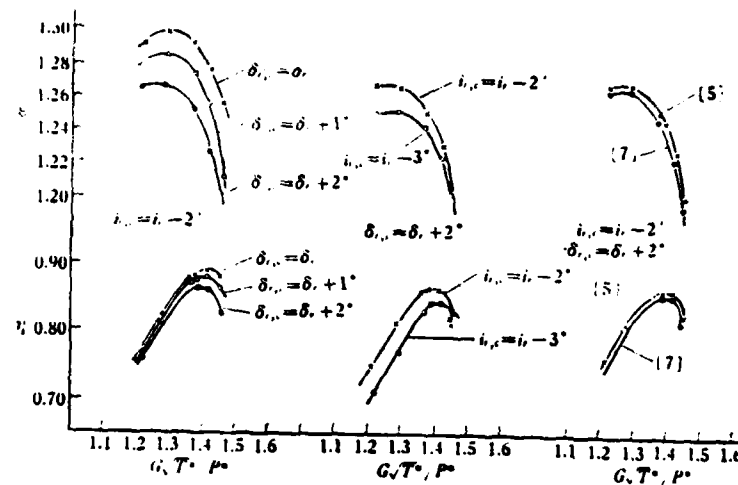


Figure 3. Effect of reference attack angle, reference lag angle, and selection of loss model on stage characteristics. Single stage test compressor, $n=19000$ revolution/min.

4. Effect of different computational methods of the curvature and slope of stream lines on the characteristics: Besides representing the stream line with a cubic representation, it can also be represented as a multi-nomial. If we still use the 2 cross-sectional areas at the inlet of the compressor and in front of the inlet airfoil as the reference cross-sectional areas, then in the case of our sample calculation, the characteristics obtained by calculating the slope and curvature of the stream line with a multi-nomial yield the same result as with a cubic representation. The difference is negligible.

5. Effect of the radial distribution of curvature, slope and entropy on the radial equation of motion: Figure 4 is the calculated results of the radial distribution of curvature, slope, and entropy on the axial velocity distribution. From this one can see that generally for the first few stages of the subsonic compressor, not only is there not much effect on the axial velocity distribution due to the non-uniformity of entropy, but for ordinary channels, there is not much effect due to stream line curvature or slope either, (generally less than 5%).

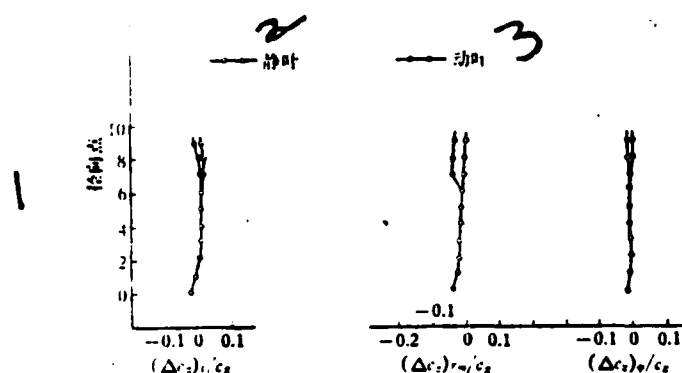


Figure 4. In a completely radial equation of motion, the effect of the variation of entropy, curvature and slope in axial velocity calculation. (sample computation 2)

Key: 1--radial point; 2--stationary airfoil; 3--moving airfoil.

In addition, if only the axial gap dimensions of the channel are changed and not the radial dimension of the various calculated cross-sectional areas or the geometric parameters of the airfoil, calculation shows that there is very little difference between the characteristics obtained and the original characteristics. This also shows that the curvature and slope of the stream line has little effect on the subsonic stage. Hence, in simulation testing, to make the measurement more convenient, increasing the axial dimensions will still give usable experimental results for the subsonic stage. /13

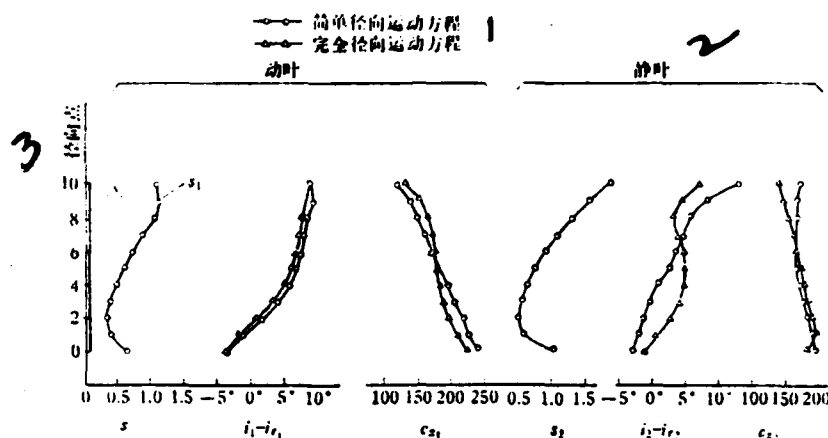


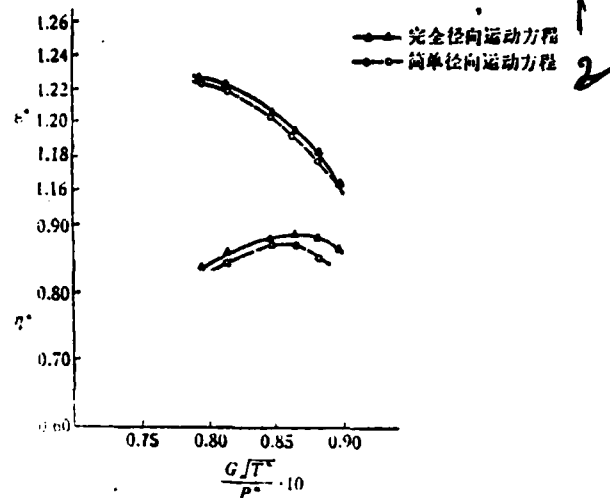
Figure 5. Comparison of perfect radial equation of motion and simple radial equation of motion — with the outlet entropy, axial velocity and change in attack angle of sample calculation 2.

Key: 1-- -o-o- simple radial equation of motion
 -Δ-Δ- perfect radial equation of motion;
 2--stationary airfoil; 3--radial point.

6. Comparison of simple radial equation of motion and perfect radial equation of motion: For sample calculation 2, Figure 5 shows the results calculated for the simple radial equation of motion and perfect radial equation of motion, including the entropy behind a moving airfoil and behind a stationary airfoil, axial velocity and the attack angle of a moving airfoil and of a stationary airfoil, etc. From the diagram, it can be seen that there is definitely a difference in the 2 attack angles calculated. This is also reflected in the radial distribution of the axial velocity and the stage characteristics. But, if the slope of the passage way is not large, this difference is small. But, if the slope of the passage way is large, then it is better to calculate according to the perfect radial equation of motion. Figure 6 gives the difference between the characteristics for these 2 methods of calculations.

Figure 6. Comparison of characteristics for the perfect radial equation of motion and the simple radial equation of motion.
(sample calculation 2 - $n = 8600$ rev/min)

Key: 1 - $\Delta-\Delta-$ perfect radial equation of motion,
2 - $o-o-$ simple radial equation of motion.



6. COMPARISON WITH TEST RESULTS

Figures 6-8 gives the diagrams of the stage characteristics and stream line in the 2 sample calculations. Figure 9 gives the air stream exit angle inlet leading airfoil, moving airfoil and stationary airfoil. Figure 7 and Figure 9 also show the experimental results. From the diagrams, it can be seen that: in the vicinity of the reference attack angle, the calculation agrees with the experiment, but when we deviate from the reference attack angle region, there is a larger difference between calculation and experiment in the characteristic, especially in the pressure ratio. For positive attack angle, the calculated pressure ratio is higher than the experimental value. One may regard this as due to the angle of lag and loss under changed working conditions in Reference [5], especially due to the unreasonable calculation of the angle of lag. We made corrections to the curve of Reference [5] based on this (see Figure 1) and increased the change in the angle of lag below the positive attack angle. The characteristics calculated from the curve of corrected lag angle changes are also plotted in Figure 7 which shows good agreement with experiment. From Figure 9, we see that in the vicinity of the design point, the calculated lag angle value also agrees with the experimental value.

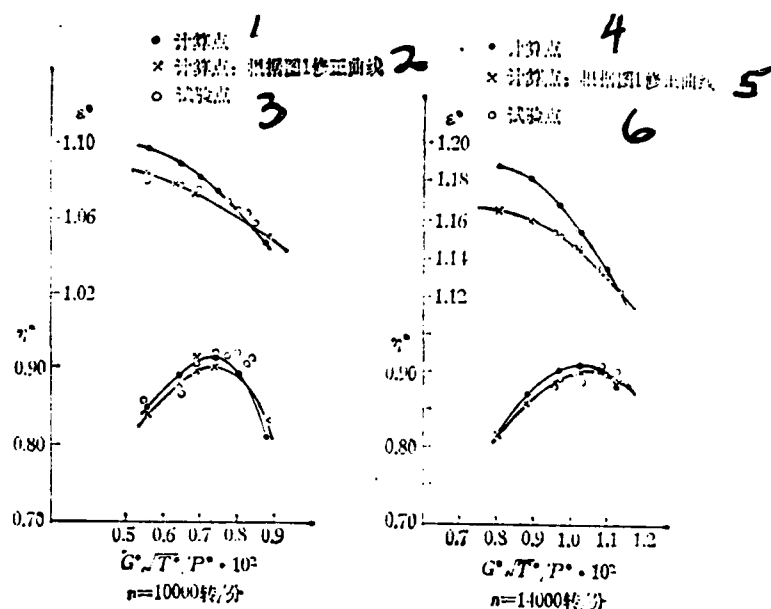


Figure 7. Characteristics of single stage test compressor ($n=10000$ and $n=14000$ rev/min.)

———— perfect radial equation of motion.

----- simple radial equation of motion.

Key: 1--● calculated point; 2--x calculated point, from corrected curved in Figure 1; 3--o experiment point; 4--● calculated point; 5--x calculated point, based on corrected curve in Figure 1; 6--o experiment point.

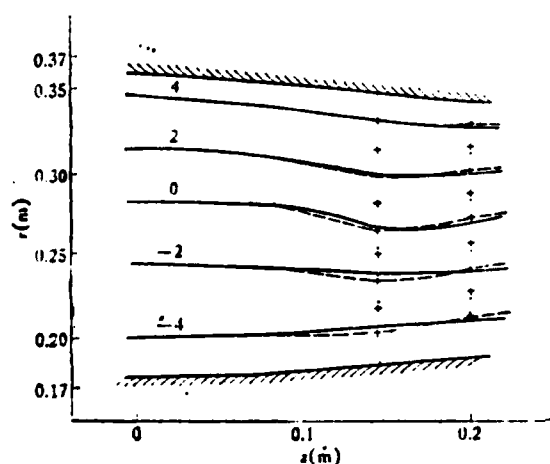


Figure 8. Channel shape and stream line distribution in sample calculation 2. ($n=8600$, $G=48.5$ kg/sec)

—○— experimental $\varphi = 0.781$
 —●— calculated $G = 5.0$ kg/sec.

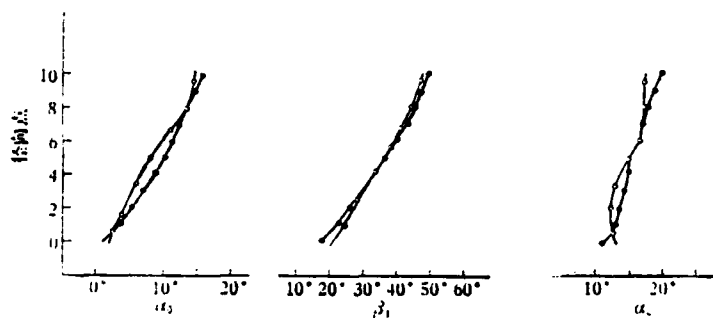


Figure 9. Single stage test compressor air stream exit angle — comparison between calculated and experimental results. ($n=10000$ rev/min.)

7. CONCLUSIONS

1. For subsonic stage with small channel slope, there is not much difference in the calculated results between a perfect radial equation of motion and simple radial equation of motion. But when the slope is larger, one should calculate with the perfect radial equation of motion.

2. For the calculation of compressor characteristics, the degree of accuracy of the reference angle of attack and its corresponding angle of lag is more important than the choice of loss model.

3. A problem requiring immediate solution in characteristic calculations is the method of calculating the angle of lag and loss under changing working conditions.

4. In order to apply 3 dimensional flow theory effectively to engineering, the most pressing task currently is to strengthen experimental research. It will not only provide experimental data for the proposed physical models, but also will give the criteria for judging whether a physical model is good or bad.

REFERENCES

- [1] Wu Chung-hua: A General Theory of Three-Dimensional Flow in Subsonic and Supersonic Turbomachines of Axial, Radial, and Mixed-Flow Types, ASME Paper No. 50-A-79, 1950; Trans ASME Nov. 1952, or NACA TN 2604, 1952.
- [2] Wu Zhonghua: Basic Equations of 3-Dimensional Flow of Turbo-Machine and Their Solutions with Non-Orthogonal Curvilinear Coordinates and Non-Orthogonal Velocity Components. Paper presented at the 3rd International Air Jet Engine Conference, Munch, Germany, 1976, Journal of Mechanical Engineering, Vol. 15, #1, June, 1979.
- [3] T. H. Smith, Jr. "The radial-equilibrium Equation of Turbomachinery" Journal of Engineering for Power, Trans. ASME, Series A, Vol. 88, 1966.
- [4] "Aerodynamic Design of Axial-Flow Compressor" NASA SP-36, 1965.
- [5] H. F. Creveling, et al. "Axial Flow Compressor Computer Program for Calculating Off-design Performance (Program IV)" NASA-CR-72427, 1968.
- [6] Zhang Cuenlin: Summary of Compressor First Stage Simulation Testing (Schedule 1), Work Report, May, 1966.
- [7] T. Hiroki & H. Jshizawa. "Some Problems Encountered in the Design and Development of a Transonic Compressor" Gas Turbine Paper Presented at Tokyo Joint International Gas Turbine Conference and Products Show, 1971.

APPLICATION OF THE FINITE ELEMENT METHOD TO THE
SOLUTION OF TRANSIENT TWO-DIMENSIONAL
TEMPERATURE FIELD FOR AIR-COOLED
TURBINE BLADE

Guo Kuan-liang Ge Xin-shi Sun Ziao-lan
(The Chinese University of Science of Technology)

Abstract

To assure air-cooled turbine blade of being able to operate safely and reliably during continuous variation of mechanical, particularly thermal loads, it is necessary to calculate the transient temperature field of blades. In this paper the finite element method for computation of transient two-dimensional temperature distribution is discussed. the calculation of transient temperature field for a middle cross section of air-cooled blade is made and discussed.

1. INTRODUCTION

The adoption of air-cooled blades has increased the inlet temperature of turbines and provided a powerful measure in improving the performance of jet engines. To make sure that the air-cooled blades work safely and reliably at high temperatures, high pressure, burning gas, the calculation of the temperature field is a vital link in the research and development of air-cooled blades. Especially when the engine is working under acceleration or deceleration, the mechanical and thermal loads of the blades change drastically and the blades are working under extremely severe conditions. Hence, the calculation of a transient temperature field is even more important.

* This paper has been presented at the Second National Engineering Thermal Physics Conference of Hangzhou in November, 1978.

As far as we know, there is a large quantity of work on the finite element method for solving problems involving thermal conduction of solids in foreign countries, but very little has been reported on using the finite element method to calculate the transient temperature field of air-cooled blades and the treatment of boundary parameters.

In recent years, works have been started domestically in applying the finite element method to calculate the steady state temperature field of air-cooled blades. In Reference [1], a method of air-cooled blade boundary parameter treatment is presented, and a special computer program in ALGOL-60 language on the DJS-21 computer is given. Reference [2] summarized how to establish the variational principles thorough analyzing the physical phenomena from which the equations for the finite element method of solving the steady state and transient thermal conductivity problems are derived. Reference [3] proposed the computational method for the transient temperature field of the air stream in the passageway of air-cooled blades.

In this paper, we have compared the effects of various time step sizes on computational results and presented a FORTRAN program on the DJS-8 computer for calculating the 2-dimensional transient temperature field of air-cooled blades.

2. FINITE ELEMENT METHOD FOR 2-DIMENSIONAL TRANSIENT THERMAL CONDUCTIVITY PROBLEMS

For 2-dimensional transient thermal conductivity problems with boundary conditions of the 3rd kind, the differential equation is

$$\frac{\rho c}{\lambda} \frac{\partial T}{\partial t} - \left(\frac{\partial^2 T}{\partial x^2} + \frac{\partial^2 T}{\partial y^2} \right) = 0 \quad \text{on region } \Omega \quad (1)$$

The boundary condition is

/141

$$\partial T / \partial n = (\alpha_s / \lambda)(T_s - T) \quad \text{on boundary } \Gamma \quad (2)$$

For air-cooled blades, both the inner and outer walls will exchange heat convectionally with the fluid. The corresponding boundary condition may be written as

$$\frac{\partial T}{\partial n} = \begin{cases} (\alpha_g / \lambda)(T_{sg} - T) & \text{on the burning gas side} \\ (\alpha_c / \lambda)(T_{sc} - T) & \text{on the cool gas side} \end{cases}$$

The initial condition is

$$T(0, x, y) = T_0(x, y) \quad (3)$$

where: ρ, c, λ are respectively the density, specific heat and average thermal conductivity of the blade material. α_g, α_c are, respectively, the convectional heat exchange coefficients of the burning gas and the cool gas on the blade wall. T_{sg}, T_{sc} are, respectively, the absolute thermal recovery temperatures of the burning and cooled gas. Since the stream velocity of the cool gas is rather low, therefore $T_{sc} \approx T_{sg}$ where the subscript s denotes air streams.

To use the finite element method for solving the transient temperature field, we must first obtain the equivalent starting equations of the finite element method for the above problem. This is usually done through the mathematical treatment of the relatively simple method of the weighted residual (e.g., Galerkin method) on from the variational principle which is more intuitive in its physical meaning [2].

Here, we present the result derived with the Galerkin method [4,5]

$$\begin{aligned} & \iint_V \delta T \frac{\rho c}{\lambda} \frac{\partial T}{\partial t} dx dy + \iint_V \left(\frac{\partial \delta T}{\partial x} \frac{\partial T}{\partial x} + \frac{\partial \delta T}{\partial y} \frac{\partial T}{\partial y} \right) dx dy \\ & + \int_\Gamma \delta T \frac{\alpha_s}{\lambda} (T - T_s) dl = 0 \end{aligned} \quad (4)$$

1. Spatial discretization:

When we discretize equation (4), we assume that the thermal expansion of the solid may be neglected.

We divide the solution region Ω into NE triangular surface elements, and represent respectively, with NP and NL, the number of nodal points (i.e., the total number of vertices of the triangles) and the line element on the boundary Γ . Consider the linear interpolation function of an arbitrary triangular surface element (with vertices i,j,m)

$$T = (N_i, N_j, N_m) \begin{pmatrix} T_i \\ T_j \\ T_m \end{pmatrix} \quad (5)$$

where N_i, N_j and N_m are the shape function and

$$N_k = (a_k + b_k x + c_k y) / 2\Delta \quad k = i, j, m; \quad \Delta = (b_i c_j - b_j c_i) / 2 \quad (6)$$

$$\begin{aligned} a_i &= x_j y_m - x_m y_j; & b_i &= y_j - y_m; & c_i &= x_m - x_j \\ a_j &= x_m y_i - x_i y_m; & b_j &= y_m - y_i; & c_j &= x_i - x_m \\ a_m &= x_i y_j - x_j y_i; & b_m &= y_i - y_j; & c_m &= x_j - x_i \end{aligned} \quad (7)$$

Take δT with the same functional form as T, i.e.

$$\delta T = (\bar{T}_i, \bar{T}_j, \bar{T}_m) \begin{pmatrix} N_i \\ N_j \\ N_m \end{pmatrix} \quad (8)$$

where $\bar{T}_i, \bar{T}_j, \bar{T}_m$ are respectively, the value taken by the arbitrary function δT at nodal points i,j, and m. Similarly for a line element on the boundary Γ (let its end points be i and j) we may take

$$T = (N_i, N_j) \begin{pmatrix} T_i \\ T_j \end{pmatrix}; \quad \delta T = (\bar{T}_i, \bar{T}_j) \begin{pmatrix} N_i \\ N_j \end{pmatrix} \quad (9) \quad /142$$

By using eq. (5)-(9), we may discretize the terms in eq. (4) as

$$\begin{aligned}
\iint_{\Omega} \delta T \frac{\rho c}{\lambda} \frac{\partial T}{\partial t} dx dy &= \sum_{k=1}^{NS} \iint_{\Omega_k} \delta T \frac{\rho c}{\lambda} \frac{\partial T}{\partial t} dx dy = \dot{T} C \dot{T} \\
\iint_{\Omega} \left(\frac{\partial \delta T}{\partial x} \frac{\partial T}{\partial x} + \frac{\partial \delta T}{\partial y} \frac{\partial T}{\partial y} \right) dx dy &= \sum_{k=1}^{NS} \iint_{\Omega_k} \left(\frac{\partial \delta T}{\partial x} \frac{\partial T}{\partial x} + \frac{\partial \delta T}{\partial y} \frac{\partial T}{\partial y} \right) dx dy = \dot{T} K_1 T \\
\int_{\Gamma} \delta T \frac{\alpha_L}{\lambda} (T - T_i) dl &= \sum_{l=1}^{NL} \int_{L_l} \delta T \cdot \frac{\alpha_L}{\lambda} (T - T_i) dl = \dot{T} (HT - R)
\end{aligned}$$

and also get

$$C\dot{T} + KT - R = 0 \quad (10)$$

where $K = K_1 + H$.

After eq. (4) is spatially discretized, we obtain a set of equations including NP first order ordinary differential equations as mentioned above. The appearance of the matrix C is related to the thermal capacity term; the K_1 in the K matrix has nothing to do with time while H is related both to space and to time (it contains the local thermal radiation coefficient and thermal conductivity); R is a column vector, and is homogeneous; the column vector T is the temperature function yet to be found.

2. Time discretization

To convert (10) into linear algebraic equations, we may use different methods of time discretization. Three discretization schemes are presented here:

(1) By using the method of a weighted residual with linear approximation for the temperature function, etc., it is easy to show that

$$\begin{aligned}
&[(2/\Delta t)(C_1 + 2C_2) + K_1 + 3K_1]T_1 \\
&- [(2/\Delta t)(C_1 + 2C_2) - K_1 - K_1]T_2 + (2R_1 + 4R_2)
\end{aligned} \quad (11)$$

where $\Delta t = t_1 - t_0$ is the time step.

(2) By using the method of weighted residual with quadratic approximation for the temperature function, etc. [6,7], we can derive

$$\begin{bmatrix} M_{11} & M_{12} \\ M_{21} & M_{22} \end{bmatrix} \begin{bmatrix} T_1 \\ T_2 \end{bmatrix} = \begin{bmatrix} G_1 - M_{13} & T_0 \\ G_2 - M_{23} & T_0 \end{bmatrix} \quad (12)$$

where

$$M_{ij} = KL_{ij}K_i + KA0_{ij}H_0 + KA1_{ij}H_1 + KA2_{ij}H_2 + CE_{ij}C/\Delta t/2$$

$$G_i = -(RE_{i1}R_0 + RE_{i2}R_1 + RE_{i3}R_2)$$

$$KL = \begin{bmatrix} 224 & 28 & 28 \\ 28 & 56 & -14 \end{bmatrix} \quad KA0 = \begin{bmatrix} 16 & -8 & 20 \\ -8 & -3 & 3 \end{bmatrix}$$

$$KA1 = \begin{bmatrix} 192 & 16 & 16 \\ 16 & 20 & -8 \end{bmatrix} \quad KA2 = \begin{bmatrix} 16 & 20 & -8 \\ 20 & 39 & -3 \end{bmatrix}$$

$$CE = \begin{bmatrix} 0 & 140 & -140 \\ -140 & 105 & 35 \end{bmatrix} \quad RE = \begin{bmatrix} 28 & 224 & 28 \\ -14 & 28 & 56 \end{bmatrix}$$

(3) C-N scheme [8,9,10]

Let us assume that within the time step Δt , the derivative \dot{T} of temperature wrt time varies linearly with time, then

$$(T_1 - T_0)/\Delta t = (\dot{T}_0 + \dot{T}_1)/2$$

Assume also that $(\rho c/\lambda)_0/(\rho c/\lambda)_1 = 1$, i.e., $C_1^{-1}C_0 = 1$ (one may not make this assumption) the subscript 1 means the inverse matrix of the labeled matrix. Then we may transform eq. (10) into

$$[(2C_1/\Delta t) + K_1]T_1 = [(2C_1/\Delta t) - K_1]T_0 + R_0 + R_1 \quad (13)$$

It is worth while to point out that since in eq. (10), C, K, and R are all functions of temperature, it is a set of non-linear ordinary differential equations. When making use of the C-N scheme, we have considered the non-linearity of the equations. The result obtained (13) is an improvement over the usual linear approximations.

(4) Comparison of the 3 schemes above

The results of 3 discretization processes, i.e., eq. (11), (12), and (13) are all implicit and are unconditionally stable. When the 3 schemes are composed, we may for convenience assume eq. (10) is linear and homogeneous. Then it is not difficult to prove that: Eq. (11) is accurate to order $O(h)$ (h being the time step length) and eq. (12) and (13) are both accurate to order $O(h^2)$ (better than eq. (11), but since the latter is much simpler to calculate than the former, we shall use eq. (13) in our calculation.

3. COMPUTATION OF BOUNDARY PARAMETERS

In order to calculate the various instantaneous C , K , and R in eq. (13), and then solve for the transient temperature field of the air-cooled blade, we must first know the instantaneous values of the boundary parameters α_1 , α_2 , T_{s1} and T_{s2} and the average thermal conductivity λ and specific heat C of the blade material. In this work, we calculated a transient process, starting with the initial state of the air-cooled blade (assumed to be a steady state) and gradually accelerating for a given period time until the parameters of the burning gas and cool gas stream no longer change and finally after a period of "stagnation" reaching the steady state at the end. Of course, the finite element method and the method of treating boundary conditions as mentioned above are also applicable to other state-changing situations. In the following, we shall briefly introduce the method of treating the parameters. For a detailed calculation, see Reference [3].

1. If we denote by ξ_i (the subscript i indicates the parameter under discussion) the ratio of the various instantaneous parameters of the burning gas and cool gas stream to the corresponding parameter at the final steady state, then α_1 , α_2 and T_{s1} can be conveniently obtained from the known value of ξ_i and the steady state values of α_{s1} , α_{s2} and T_{s1} already obtained in Reference [1],

and there is no need to go through the complicated computation according to the original standard formulas one by one.

For example:

$$\begin{aligned} \alpha_s &= \alpha_{s0} \cdot \xi_{s0} (\xi_{w0} / \xi_{s0})^{1/2} \\ \alpha_r &= \alpha_{r0} \cdot \xi_{r0} (\xi_{a0} / \xi_{r0})^{1/2} \end{aligned}$$

2. The thermal capacity of the blade must be taken into account in calculating the transient temperature of the cool gas stream along the blade wedge direction. Here the basic equations treating by sections according to one dimensional problem should be

$$\begin{cases} \alpha_s F_s (T_{s0} - \bar{T}_s) = \sum_{k=1}^4 \alpha_{rk} F_{rk} (\bar{T}_s - \bar{T}_{rk}) + 7200 \gamma c V (\bar{T}_s - \bar{T}_m) / \Delta t \\ \alpha_{rk} F_{rk} (\bar{T}_s - \bar{T}_{rk}) = G_{rk} C_{rk} (T_{rk}^0 - T_{rk}^i) & k = 1, 2, 3, 4 \\ \bar{T}_{rk} = (T_{rk}^i + T_{rk}^0) / 2 & k = 1, 2, 3, 4 \\ T_{rk}^0 = T_{rk-1}^i & k = 4, 3, 2 \end{cases}$$

where: T_{ck} is the cool gas stream temperature in the k th channel; γ is the specific gravity of the blade material; V is the volume of each blade section; F_s, F_{rk} are respectively, the outer area of the blade and the inner area of the k th channel; \bar{T}_m is the average temperature of each blade section at the beginning instant of the time step Δt , its initial value being calculated from the initial steady state; the subscripts i and o denote, respectively, the parameters at the outlet and inlet of each section.

Since \bar{T}_m and T_{rk}^i of the above equations are already known, by solving the above equations, we can then get the temperature variation of the cooling gas stream in the passages of the blade at each instant, and also the average temperature \bar{T}_s of the blade cross-section from which the corresponding ρ, c and λ , may be found and $\rho c / \lambda$ and α_s / λ computed.

/144

4. THE COMPUTER PROGRAM AND ITS EXPLANATION

From eq. (13) it is not difficult to see that although T_0 is given by the initial conditions (3) and the initial state R_0 and K_0 can be calculated from known parameters, yet R_1 , C_1 and K_1 are both functions of T_1 . Hence, it is necessary to use the iteration method to solve for T_1 . Since we have already obtained the cross-sectional average temperature of the blade at each instant when we calculate T_{ck} , it may be used as a very good approximation of the cross-section average of T_1 . With it we can calculate a prior R_1 , C_1 and K_1 and the R_1 , C_1 and K_1 at each instant. Eq. (13) may then be transformed to the following form

$$KT - R$$

and may be solved by using the direct matrix analysis method. This will not only satisfy the demand of engineering computations, but also reduce greatly the amount of computation.

Because of the limitation of space, we shall omit the computational flowchart, the FORTRAN program and explanations in this paper.

5. COMPUTATIONAL RESULT AND ANALYSIS

In this work, we have calculated the temperature distribution of the blade at each instant of an accelerated working state. For an intuitive understanding, Figure 1 and 2 show the instantaneous temperature distribution at 5 different instants at the periphery on the burning gas side of the blade middle cross-section (i.e., blade back and blade bowl). In Figure 3, the time variation of the average temperature of the middle cross-section calculated by the finite element method is plotted. Also for comparison, the cross-sectional average temperature curve obtained from one dimensional sectional treatment is also plotted.

1. The point of maximum temperature on the air-cooled blade is located at the boundary of the tail section on the burning gas side, and the point of lowest temperature is located at the boundary of the internal cooling orifice. This is quite reasonable. The isothermal distribution curve at each instant also agrees with physical law.

It can be seen from Figure 1 and 2 that the temperature at the front edge and tail edge is higher and that at the middle of the blade back and bowl is relatively lower. When the blades are continuously accelerated, their temperatures continue to rise. The tendency of the temperature distribution at different instants is basically the same.

2. From Figure 3, comparing the cross-sectional average temperature calculated from the finite element method and that from one dimensional treatment by sections, the maximum difference is below 2%. This shows that when solving eq. (13), by calculating a priori C_1 , K_1 and R_1 with the various instantaneous cross-sectional average temperatures obtained by sectional treatment and reducing the non-linear problem to linear equations, it is definitely possible to provide the accuracy required.

3. To compare the effect of various time step length Δt , in this calculation, we use respectively, 0.02, 0.5, 1 and 2 seconds as the time step length. The results indicate that the time step lengths used have little effect on the cross-sectional average temperature. For example, when $\Delta t = 0.02$ sec, $\bar{T}_b = 1008.2$ K at 16 seconds which for $\Delta t = 2$ second, $\bar{T}_b = 1011.4$ K at 16 seconds. Thus when the time step length is increased 100 times, the blade cross-sectional average temperature only varies by 3.2 degrees. The relative difference is only 0.3% (the other cases are even better than this).

4. Similar to the situation of finding the 2 dimensional steady state temperature field of air-cooled blades with finite element method [1], the accuracy of the transient temperature field

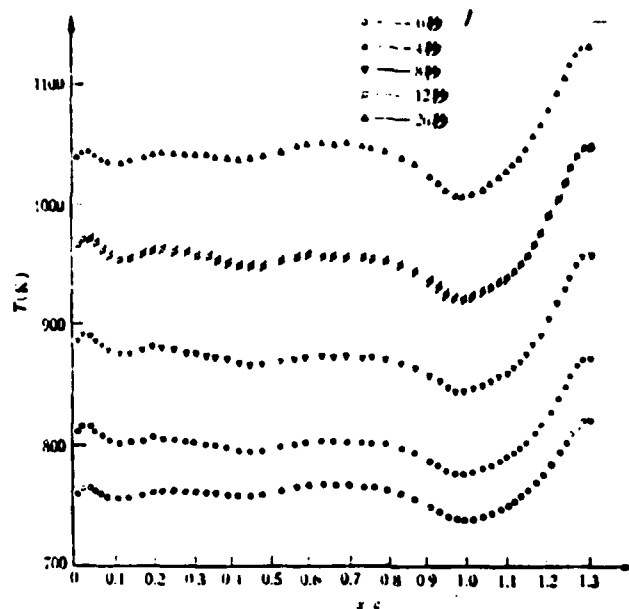


Figure 1. Blade back temperature distribution at different times.

Key: 1--second.

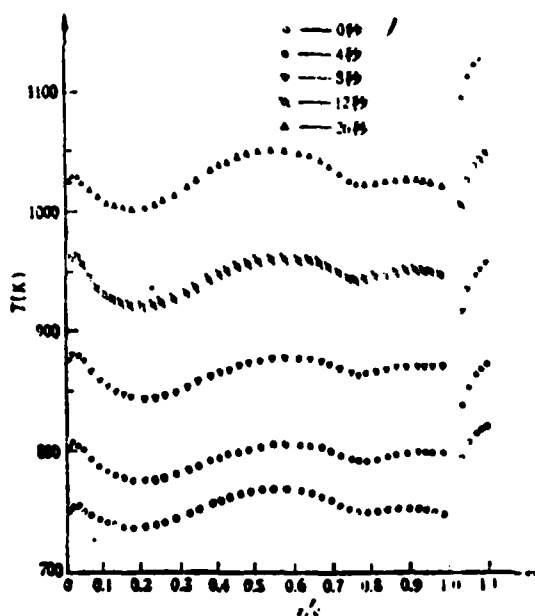


Figure 2. Blade bowl temperature distribution at different times.

Key: 1--second.

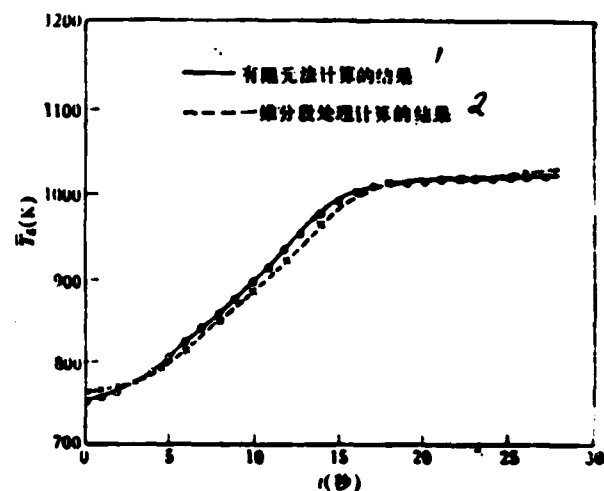


Figure 3. Time variation curve of blade cross-sectional average temperature \bar{T}_B .

Key: 1--results calculated by finite element method; 2--results calculated by one dimensional sectional treatment.

calculation is also determined basically by the calculation of the boundary parameters. Hence, accurate determination of the local convective heat exchange coefficient α , on the burning gas side, the convective heat exchange coefficient α , of each internal cooling passages and the cool air flow rate G , of the air-cooled blade requires further investigation.

/14

In completing this work, we have received the earnest support of the Research Institute of Shenyang Aeronautic Engine Company. Comrades Li Yishen, and Huang Kecheng of our university also gave us helpful support. We would like to express our gratitude to all of them.

REFERENCES

- [1] Chinese University of Science and Technology: Calculation of 2-Dimensional Steady State Temperature Field of Turbine Air-cooled Blade with the Finite Element Method, Chinese Science, (1976), #3.
- [2] Geo Xinshi, Guo Kuanliang, Sun Xiaolan: Variational Principle of Thermal Conducting Problem in Solids, (1978) Second National Engineering Thermal Physics Conference Report.
- [3] Guo Kuanliang, Ge Xinshi, Sun Xiaolan: Computation of Air Stream Transient Temperature Field in Internal Passages of Air-Cooled Blades. (1978) Second National Engineering Thermal Physics Conference Report.
- [4] Douglas, H. Norrie, Gerard de Vries, The Finite Element Method—Fundamentals and Applications (1973).
- [5] Kenneth, H. Huebner, The Finite Element Method for Engineers (1975).
- [6] G. Warzee "Finite Element Analysis of Transient Heat Conduction Application of the Weighted Residual Process" Computer Methods in Applied Mechanics and Engineering, Vol. 3, (1974), 255—268.
- [7] W. Köhler and J. Pitt, "Calculation of Transient Temperature Fields with Finite Elements in Space and Time Dimensions" International Journal for Numerical Methods in Engineering Vol. 8 (1974), 625—631.
- [8] O. C. Zienkiewicz and Y. K. Cheung, The Finite Element Method in Structural and Continuum Mechanics (1967).
- [9] A. F. Emey and W. W. Carson, "Evaluation of Use of the Finite Element Method in Computation of Temperature" ASME Paper 69 WJ/HT-37, (1969).
- [10] W. G. Strang and G. J. Fix, An Analysis of the Finite Element Method (1973), 241—251.

COMPUTERIZED LASER THERMAL DIFFUSIVITY MEASUREMENT APPARATUS *

Xi Tung-geng, Zhou Sin-yu, Li Zong-jie, Ni He-line, Gu Zong-yi**
(Shanghai Institute of Ceramics, Academia Sinica)

Abstract

This article discussed the physical model for thermal diffusivity measurement by pulsed laser technique, and described the fundamentals of data processing and control by a computer. Several boundary conditions must be satisfied in the measurement. The thermal diffusivities of standard specimens—Armeo iron and α -Al₂O₃, as well as other materials were determined by the apparatus. Data obtained from the standard specimens were compared with recommended values in the literature and found to be in good agreement. The r.m.s. errors of Armeo iron and α -Al₂O₃ specimen measurements amount to $-3.2 - +3.3\%$ and $-2.4 - +5.6\%$ respectively. This apparatus features automatic and high speed measurement, and is recommended to be operated in the temperature range of 300 to 1800°C. The interval between laser emission and display of result is approximately 5 seconds.

1. INTRODUCTION

The pulsed laser technique to measure thermal diffusivity λ as developed in the sixties has overcome the limitations of other methods, and provides the advantages of small sample size, high speed, high precision and is applicable to the measurement of a wide variety of materials. Hence, it attracts close attention and develops very rapidly. According to reports [1,2], 75% and more of the thermal diffusivity data have been measured with this method after 1973. In the seventies, after the incorporation of computer technique, the precision and speed of laser thermal

* This paper has been presented at the Second National Engineering Thermal Physics Conference in Hangzhou, in November, 1978.

** Tan Chenxi, Wu Shanyu and Shao Jiesun also participated in this work.

diffusivity measurement apparatus have pronouncedly improved [2].

Our Institute, together with the Shanghai Laser Station, Shen Yang Metal Institute, Academia Sinica and Shanghai Steel Institute, jointly researched and developed the laser thermal diffusivity measurement apparatus in 1973. In April of 1978, our institute also successfully developed a computerized laser thermal diffusivity measurement apparatus and improved its various characteristics.

2. METAL PHYSICS MODEL AND PRINCIPLE OF MEASUREMENT

The physical foundation of the steady state method and transient method for measuring the thermal diffusivity λ is the differential equation of thermal diffusion. This equation may be solved by using various specific boundary conditions. The solution obtained is generally related to the thermal properties of matter [4].

The physical model of the pulsed laser measurement technique for λ is to radiate normally on the front surface of a thin circular disc (the sample) insulated at the periphery, with a uniform laser pulse beam and then by measuring the temperature rise curve on the back side of the sample under one dimensional heat flow conditions, to find the temperature diffusivity α from which the λ value may be deduced.

Let the initial temperature distribution at any point X on a circular disc with sample thickness L be $T(x,0)$, then the temperature distribution $T(x,t)$ [5] at any time t is

$$T(x,t) = \frac{1}{L} \int_0^L T(x,0) dx + \frac{2}{L} \sum_{n=1}^{\infty} \exp\left(\frac{-n^2 \pi^2 \alpha t}{L^2}\right) \cos \frac{n \pi x}{L} \int_0^L T(x,0) \cos \frac{n \pi x}{L} dx. \quad (1)$$

At the instant $t_0 (t_0 \rightarrow 0)$, when the sample absorbs the laser the temperature distribution at X within a very small distance E from the front surface ($x=0$) of the sample is

/148

$$T(x, t_0) = Q/D \cdot c \cdot g, \quad \text{当 } 0 < x < g; \quad (2)$$

$$T(x, t_0) = 0, \quad \text{当 } g < x < L. \quad (3)$$

where D and c are respectively the density and specific heat of the sample, Q the radiation intensity of the laser pulse absorbed by the sample and T(x, t₀) is the temperature rise of the sample relative to the experimental store temperature.

Substituting eq. (2), (3) into (1), because $t_0 \rightarrow 0$, $T(x, t_0) \approx T(x, 0)$ then

$$\begin{aligned} T(x, t) = & \frac{Q}{L \cdot D \cdot c} + \frac{2}{L} \sum_{n=1}^{\infty} \exp\left(\frac{-n^2 \pi^2 \alpha t}{L^2}\right) \cos \frac{n \pi x}{L} \cdot \frac{Q}{D \cdot c \cdot g} \cdot \frac{L}{n \pi} \sin \frac{n \pi g}{L} \\ & - \frac{Q}{L \cdot D \cdot c} \left[1 + 2 \sum_{n=1}^{\infty} \exp\left(\frac{-n^2 \pi^2 \alpha t}{L^2}\right) \cos\left(\frac{n \pi x}{L}\right) \cdot \frac{L}{n \pi g} \cdot \sin \frac{n \pi g}{L} \right]. \end{aligned} \quad (4)$$

To simplify the temperature measurement, we choose for the back side of the sample (x=L) the following special case:

$$x = L, \quad \cos \frac{n \pi x}{L} = \cos n \pi = (-1)^n; \quad (5)$$

$$\frac{g}{L} \rightarrow 0, \quad \sin \frac{n \pi g}{L} \approx \frac{n \pi g}{L}. \quad (6)$$

Substituting (5), (6) into (4), we get

$$T(L, t) = \frac{Q}{L \cdot D \cdot c} \left[1 + 2 \sum_{n=1}^{\infty} (-1)^n \cdot \exp\left(\frac{-n^2 \cdot \pi^2 \alpha \cdot t}{L^2}\right) \right], \quad (7)$$

To simplify matters, define 2 dimensionaless parameters ω and V(L, t) and let

$$\omega = \frac{\pi^2 \alpha t}{L^2}, \quad (8)$$

$$V(L, t) = \frac{T(L, t)}{T_M}. \quad (9)$$

where T_M is the maximum temperature rise after the sample is radiated by the laser, and

$$T_m = Q/L \cdot D \cdot c. \quad (10)$$

Substituting (8)-(10) into (7), we get

$$V(L, t) = 1 + 2 \sum_{n=1}^{\infty} (-1)^n \exp(-n^2 \omega). \quad (11)$$

with $V(L, t)$ and ω as coordinate, then the curve in Figure 1 represents eq. (11). From eq. (11) and Figure 1, we can fix the value of α . When $V(L, t) = 0.5$, $\omega = 1.38$, then Reference [8] becomes

$$\alpha = \frac{0.138 \cdot L^2}{t_1} \quad (12)$$

where t_1 is the time required for the back side temperature of the sample to reach $\frac{1}{2}$ its maximum value, and may be found from the temperature increase curve of the back side of the sample from which thermal conductivity α may be found.

The boundary conditions required by eq. (12) must be satisfied during the measurement: we must establish a one dimensional heat flow along the sample axis; the laser pulse time must be far smaller than the time for the sample to reach thermal equilibrium; the laser pulse should be uniformly distributed; the heat loss of the same should be minimized. Otherwise corrections must be made. Under the condition of second apparatus permit, the temperature rise on the backside of the sample should be as small as possible so that α may be treated as constant.

After α is measured, we may find λ from the following equation. /149

$$\lambda = \alpha \cdot c \cdot D \quad (13)$$

The error of C value as measured by the ice calorimeter or copper calorimeter is generally less than $1-1.5\%$ ^(6,7); hence, according to the usual way, the value of C may be found usually in handbooks.

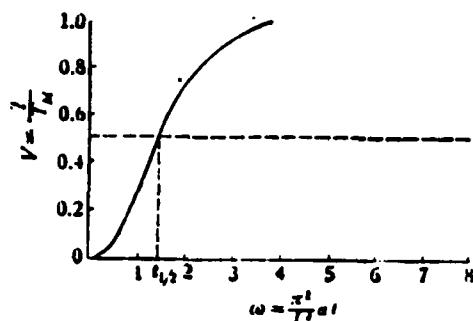


Figure 1. Curve of eq. (11).

3. STRUCTURE OF THE APPARATUS AND THE COMPUTER CONTROLLED MEASUREMENT SYSTEM

The apparatus basically consists of 4 parts (see Figure 2 and Figure 3).

1. Laser source: a Nd glass laser with xenon lamp excitation is used. The wavelength is 1.06μ , Each pulse is about 0.6 ms with an energy of about 20 Joules.

2. Vacuum carbon tube oven: the oven is insulated by carbon fibre and heated with a 10 KVA high current heater. The oven cavity contains graphite sample stand. A three-support point ZrO_2 ring is used in the oven support to fix the sample and to reduce heat loss. The vacuum chamber is water cooled and is capable of automatic elevation.

3. Optoelectric measuring system. The sample back side temperature rise is measured with a light sensitive PbS resistor. It is installed in a blackened tube with adjustable grating, Infrared lens with adjustable focus, and filter. The optically sensitive resistance is one arm of a bridge. When the laser



Figure 2. Picture of the apparatus.

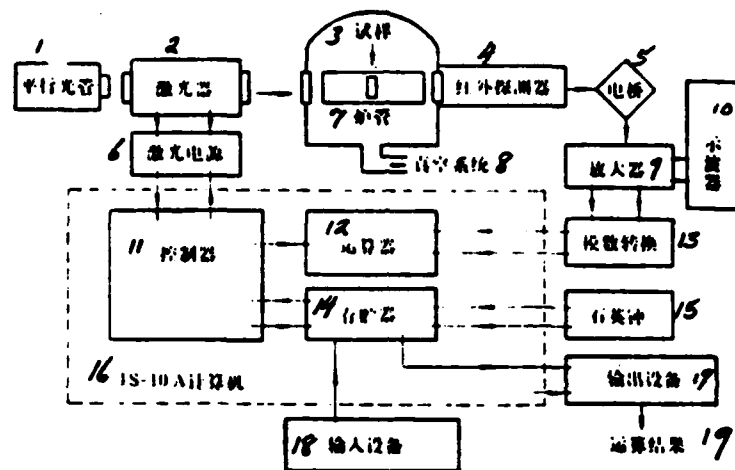


Figure 3. Block diagram of apparatus.

Key: 1--parallel lamp; 2--laser; 3--sample; 4--infrared detector; 5--electric bridge; 6--laser power supply; 7--oven tube; 8--vacuum system; 9--amplifier; 10--oscilloscope; 11--CPU; 12--ALU; 13--A to D converter; 14--memory; 15--quartz clock; 16--38-10A computer; 17--output device; 18--input device; 19--result of computation.

radiates on the front side of the sample, the temperature rise on the back side increases the light sensitive resistance. The bridge becomes unbalanced and outputs a small voltage on the load which after direct current differential amplification is sent to the oscilloscope with the time marker. The temperature increase curve is photographed on ultra-violet film or the signals can be sent to the computer. In both cases, a value may be calculated.

4. Computer control system: we used a JS-10A computer for the control. It has a computational speed of 30000 computations/second and a memory of 4K. To satisfy the special requirements of thermal diffusivity apparatus control, we made some modifications to the computer system as well as the electronic circuitry. The main control program designed by us consists of 5 sub programs:

1. Recharging and starting the pulsed laser power supply;
2. Collecting and storing sample back side temperature rise curve through A to D converter;
3. Processing and analyzing the temperature rise curve;
4. Calculating the values of $t_{\frac{1}{2}}$ and α ;
5. Automatic printout of experimental results and all the original data.

Before testing, the above programs are input into the computer from paper tape; then the data, and sample thickness are entered into the computer display. The main switch of the computer is then pressed and in 5 seconds the laser is charged up and activated. In another 5 seconds or so, the experimental results will be displayed on the printer.

4. THEORETICAL ANALYSIS OF THE VARIOUS BOUNDARY CONDITIONS IN THE TEST

1. Criteria on the degree of satisfaction of boundary conditions.

(1) Analyzing the characteristics of the temperature rise curve on the back side of the sample: Figure 1 is the sample temperature rise curve under the circumstance that the experiment satisfies all the boundary conditions. Compared to the actually measured temperature rise curve, if the latter reaches the final equilibrium temperature very slowly after a rapid temperature rise, it may be due to the non-uniformity in the radiation heating of the sample front side. The result will lead to a higher value for α . If there is a

serious radial heat flow in the sample, then the temperature rise curve will be twisted. If the temperature rise curve decreased with a large slope immediately after reaching the maximum, then it indicates a large radiation heat loss, causing a higher value for α . When the boundary conditions are satisfied, the temperature rise on the back side of the sample will be greater than 99% of the maximum temperature rise after $4 t_{\frac{1}{2}}$.

(2) Relation between measured α and Q : From the mathematical derivation in section 2, we know that irradiating the same sample with lasers of different Q should give the same value of α and the degree to which the boundary conditions are satisfied during the test may be judged from this. With multiple hole carbon as a sample, for instance, at 1420°C we have irradiated with 3 different values of Q . The $t_{\frac{1}{2}}$ and α obtained are all the same. (see figure 4). The capacitances of the 3 experimental lasers are all 2000 μf . The voltage values are respectively, 1300V, 1400V and 1500V.

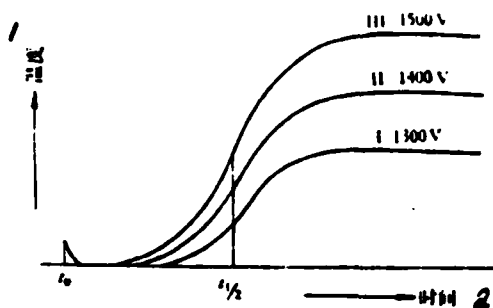


Figure 4. Experimental curve to verify the independence of α , from Q .

Key: 1--temperature;
2--time.

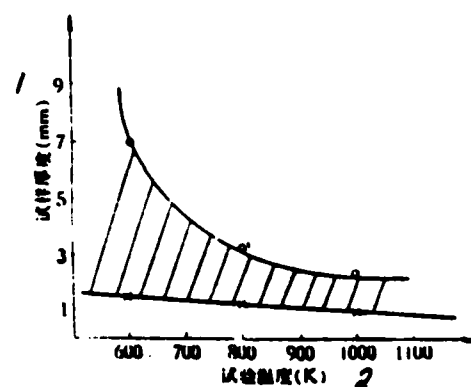


Figure 5. The optimum thickness range of pure iron at various temperatures.

Key: 1--sample thickness (mm); 2--experimental temperature (K).

2. Selection of sample optimum thickness: To better satisfy the boundary conditions at testing time, we must select the optimum

sample thickness. Too thick a sample will increase the time for the temperature rise to reach thermal equilibrium, increase the heat loss and lead to a larger value for α . Too thin a sample will not satisfy the boundary condition that the laser pulse time τ should be much less than the time for the sample to reach thermal equilibrium, and lead to a smaller value for α . Now by using pure iron samples as examples, we shall calculate the range of the optimum thickness.

(1) Calculation indicates that when the ratio of τ to the characteristic time τ_c is less than 10^{-2} , the effect of the time limitation on pulse length may be neglected [8] namely

$$\tau/\tau_c = \frac{\tau}{(L/\pi)^2 \cdot \sigma^{-1}} < 10^{-2}. \quad (14)$$

From the above equation, for pure iron samples at experimental temperatures 600 K, 800 K and 1000 K, we calculate the optimum thickness at ≥ 1.5 , 1.3 and 0.98mm, respectively.

(2) Thermal diffusivity calculation indicates that the radiation heat loss value is determined by the radiation parameter y . When $y = 5 \times 10^{-3}$, the error introduced by radiation heat loss is $< 1\%$. Also

$$y = y_r + (L/r)^2 y_s, \quad (15)$$

$$y_s = 4\sigma \cdot \epsilon_r T_0^3 L, \quad (16)$$

$$y_r = 4\sigma \epsilon_s \cdot T_0^3 \cdot r, \quad (17)$$

then

$$y = 4\sigma \epsilon_s T_0^3 L [1 + (L/r)]. \quad (18)$$

Where σ is the Steffan-Boltzmann constant, r is the sample radius, ϵ_x and ϵ_r are respectively sample axial and radial emissivity. If we are to satisfy $y = 5 \times 10^{-3}$, then at testing temperatures of

1000 K, 800 K and 600 K, the sample optimum thicknesses are respectively $\leq 2.3, 3.15$ and 7mm.

Hence, the optimum thickness range of pure iron at various temperatures lies in the shaded region in Figure 5.

5. EXPERIMENTAL RESULTS

The following are the experimental results for 3 types of samples representative of the large number of samples measured with our apparatus:

1. Armco pure iron: is the standard sample for measuring the thermal diffusivity of metals, and is supplied by the Metal Institute of Academia Sinica. The measured results agree with the recommended values of T.P.R.C. [9] and those of Powell [10] (see Table 1 and Figure 6). /15

Table 1. Percentage difference between measured values of ARMCO pure iron and the recommended values of T.P.R.C.

Temperature (K)	600	700	800	900	1000
Percentage Difference (%)	+4	+2.7	+2	+2.3	+2.6

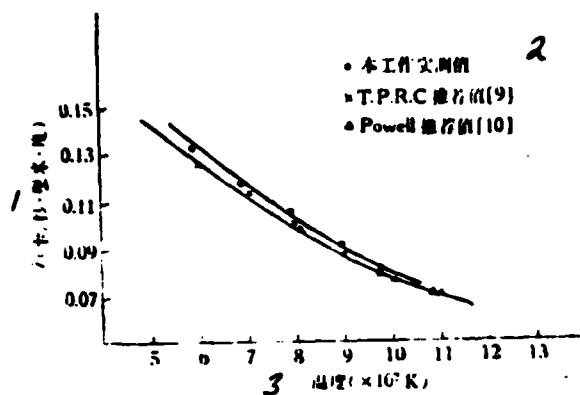


Figure 6. Thermal diffusivity curve for ARMCO pure iron.

Key: 1--(cal/sec cm deg)
 2--● our measured value
 x T.P.R.C. recommended value [9]
 ▲ Powell recommended value [10];
 3--temperature.

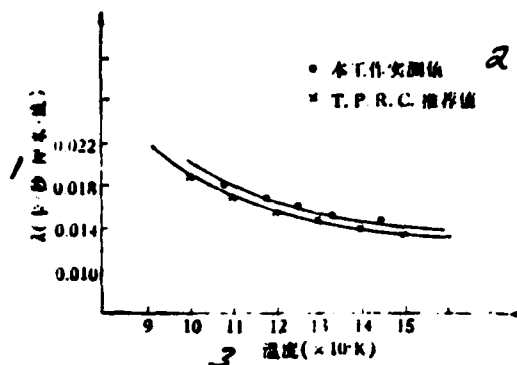


Figure 7. Thermal diffusivity curve for $\alpha\text{Al}_2\text{O}_3$.

Key: 1--(cal/sec cm deg);
 2--o our measured value
 x T.P.R.C. recommended value;
 3--temperature.

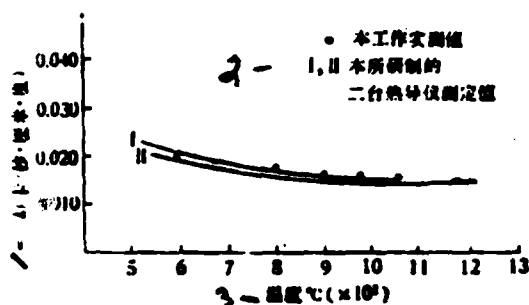


Figure 8. Thermal diffusivity curve for $\alpha\text{-Al}_2\text{O}_3$.

Key: 1-- (cal/sec cm deg);
 2-- Our measured value;
 I, II - the measured valves from 2 thermal diffusivity apparatus developed at our institute;
 3-- Temperature $^{\circ}\text{C}(10^2)$.

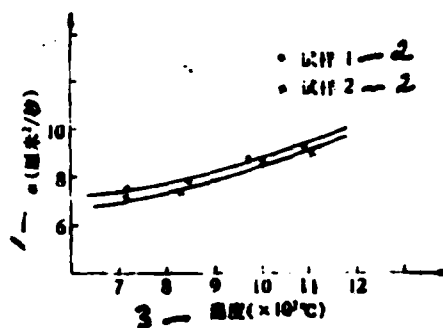


Figure 9. Thermal diffusivity curve of plasma sprayed Cr_2O_3 coating.

Key: 1-- CM^2/sec ; 2--Sample;
 3-- Temperature ($\times 10^2 ^{\circ}\text{C}$).

(2) $\alpha\text{-Al}_2\text{O}_3$: is the standard sample for thermal diffusivity measurement of non-metallic materials and is prepared by our Institute. The density is 3.96 gm/cm^3 , purity $\geq 99.5\%$. The measured results agree with the T.P.R.C. recommended values and other thermal diffusivity measurements made at our Institute [11,12] (see Figure 7, Figure 8, and Table 2).

Table 2. Experimental values of λ for $\alpha\text{-Al}_2\text{O}_3$ and the percentage difference from T.P.R.C. recommended values.

Temperature (K)	1000	1100	1200	1300	1400
Percentage difference (%)	+4.8	+4.7	+5.7	5.5	5.7

(3) Plasma sprayed with Cr_2O_3 coating: Sample air orifice rate and density are respectively 5% and 5.7 gm/cm^3 . The measured values are shown in Figure 9.

6. ERROR ANALYSIS

The weights of total error in measurement of each single term errors are all different for different samples at different temperatures. We shall now analyze the error in the measurement for pure iron at 971K.

/153

1. The measurement error introduced by secondary apparatus:

(1) Error $|e_1|$: is measuring the thickness L : $L = 2\text{mm}$

Thickness is measured with a 0 level one thousandth meter bar with maximum error $\pm 2\mu$, i.e., $\Delta L = 0.002\text{mm}$ hence,

$$|e_1| = 2|\Delta L/L| = \pm 0.2\%.$$

(2) Error $|e_2|$ in measuring λ : it includes 5 terms namely

(1) Error in the quartz crystal clock 10^{-6} sec. It may be neglected compared to the value of 110 ms for $t_{1/2}$;

(2) A to D converter error $\pm 0.5\%$;

(3) DC amplifier error, including the DC enhanced precision, enhanced stability and DC enhanced linearity are respectively $\pm 0.1\%$, with a total of $\pm 0.3\%$;

(4) The computer stores one data point every 5 ms, introducing in $t_{1/2}$ an error of 2.5 ms. Since $t_{1/2} = 110$ ms, the error introduced is $\pm 2.27\%$;

(5) Light sensitive resistor and differential amplifier time constants are of the order of micro-seconds. The error introduced in $t_{1/2}$ may be neglected.

The maximum relative error in the above 5 terms $|e_2| = \pm 3.1\%$.

2. Error introduced because the boundary conditions of Equation (12) cannot be completely satisfied:

(1) Error introduced by the effect of time-limited pulse $|e_3|$: calculation indicates that when $\tau/\tau_c < 10^{-1}$, this error may be neglected. From measurement, $\tau \approx 0.6$ ms, τ_c may be found from the equation below

$$\tau_c = (L/\pi)^2 \cdot \alpha^{-1} = 250 \text{ ms}$$

Thus $\frac{\tau}{\tau_c} < 10^{-1}$, therefore $|e_3| \approx 0$.

(2) Error introduced by sample heat loss $|e_4|$: since the experiment is carried out in vacuum, the heat loss due to air convection and conduction may be neglected. However, radiation heat loss increases with the rise of temperature and may be calculated from Equation (18), where $T_0 = 971 \text{ K}$, $\epsilon = 0.0805 \text{ cal/sec cm}^2 \text{ } ^\circ\text{C}$, $\epsilon \approx 0.3$, $L = 0.2 \text{ cm}$, $r = 0.5 \text{ cm}$. Hence, $y = 5.4 \times 10^{-1}$. From the relationship [8] between y and t_4/t_c , the constant term

in Equation (12) may be found as 0.137. Since the constant term used in Equation (12) is 0.138, the error introduced $|\epsilon_1| \approx 0.73\%$.

(3) Error introduced by the non-uniform heating of the laser beam $|\epsilon_1|$: it is difficult to measure accurately the uniformity of the beam. Analyzing the photograph we took of the beam, the beam energy is quite uniform. Besides, smoothing of the curve is considered in the computer program. According to the estimate of Taylor [2], the error in this part $|\epsilon_1| < \pm 1\%$.

In the 5 error terms above, with the exception that the radiation heat loss is a positive error, the others are all positive and negative errors. Treating them by using the root mean square error, we get the total error as $\epsilon_{\text{total}} = -3.2 - +3.3\%$.

Similarly $\alpha\text{-Al}_2\text{O}_3$ sample at 1448°K has a radiation error $|\epsilon_1| = 5\%$. With the other terms respectively $|\epsilon_1| \approx \pm 0.32\%$, $|\epsilon_2| \approx \pm 2.2\%$, $|\epsilon_3| = 0$, $|\epsilon_4| \approx \pm 1\%$. The total root mean square error is

$$\epsilon_a = -2.44\% \sim +5.6\%.$$

The root mean square errors of the 2 standard samples, and the measured values and the recommended values from foreign sources

for the percentage errors are shown in Table 3.

Table 3 shows that compared to the recommended values from foreign sources, the positive error in the measured value of λ and its magnitude is in agreement with the result of our error analysis.

/154

Table 3. Measurement error in the 2 standard samples.

T.P.R.C. recommended error [9]		Percentage error between our measured value and T.P.R.C. recommended value		Our measured error	
Pure iron		Pure iron		Pure iron	
(971K)	$\alpha\text{-Al}_2\text{O}_3$ (1448K)	(971K)	$\alpha\text{-Al}_2\text{O}_3$ (1448K)	(971K)	$\alpha\text{-Al}_2\text{O}_3$ (1448K)
$\pm 2\%$	$\pm 6-10\%$	2.6%	5.7%	-3.2% - +1.3%	-2.44% - +5.6%

7. RESULTS AND DISCUSSION

1. After our apparatus is controlled by the computer, the precision of measurement repeatability and speed of measurement degree of automation have all pronounced improved.

2. Since the emissivity of the non-metal ϵ is large, and its thermal diffusivity λ small, therefore at the same measurement temperature the error introduced by heat loss is larger than that of the metallic material. There are two ways to reduce this error: deposit carbonized tungsten with small ϵ on the sample or correct by using correction formula for radiation heat loss.

3. Since the $t_{\frac{1}{2}}$ for metal is smaller, the error introduced in $t_{\frac{1}{2}}$ when the computer takes in data is greater than that for non-metallic material. The way to reduce this error is to increase the data sampling rate of the computer, or to increase the sample

thickness without increasing significantly the radiation heat loss, i.e. to use the upper limit value of the best thickness.

REFERENCES

- [1] Taylor, R. E., "Critical Evaluation of Flash Method for Measuring Thermal Diffusivity", *PRF* 6764; PB225591/7.4S, Oct., (1973).
- [2] Taylor, R. E., "Improvements in Data Reduction for the Flash Diffusivity Methods", *Proc. 13th Inter. Conf. on Thermal Conductivity*, p.416, (1973).
- [3] Shanghai Silicate Salt Institute Laser Heat Diffusivity Apparatus Research Group, Academia Sinica: Pulsed Laser Thermal Diffusivity Apparatus. *New Inorganic Materials* Vol. 3, [3] p. 37 (1974).
- [4] Parker, W. J., Jenkins, R. J., Butler, C. P., and Abbott, G. I., "Thermal Diffusivity Measurements Using the Flash Technique", *J. Appl. Phys.*, Vol. 32, p. 1679, (1961).
- [5] H. S. Carslaw and J. C. Jaeger, *Conduction of Heat in Solids*, Oxford University Press (New York, 2nd ed., p.101, (1959).
- [6] D. C. Ginnings and R. J. Corruccini, "An Improved Ice Calorimeter—the Determination of Its Calibration Factor and the Density of Ice at 0°C", *J. Research, N. B. S.*, Vol. 38, [6] p. 591, (1964).
- [7] Xi Tonggeng, Yan Huangxiung, Ni Helin, Zu Hongfu, Cheng Ru guang: Precision Measurement Apparatus of the Specific Heat of Inorganic Non-Metallic Materials Below 1400°C and the Measurement of the Specific Heat and Heat Content of α -Al₂O₃, Collection of papers from the National High Temperature Measurement Conference. (1964).
- [8] J. A. Cape and G. W. Lehman, "Temperature and Finite Pulse-Effects in The Flash Method for Measuring Thermal Diffusivity", *J. Appl. Phys.*, Vol. 34, [7] p. 1909 (1963).
- [9] Touloukian, Y. S., Powell, R. W., Ho, C. Y., and Klemens, P. G., *Thermal Conductivity, Thermophysical Properties of Mater*, Vol. 1, IFI/Plenum, New York and Washington, p. 156 (1970).
- [10] Powell, R. W., "Progress in International Research on Thermodynamic and Transport Properties" (editors J. F. Masl) p. 454, (1962).
- [11] Su Zhengin, XuXiulan: Apparatus for Measuring the High Temperature Steady State Radial Thermal Diffusivity of Cylindrical Inorganic Non-Metal. Shanghai Silicon Salt Institute Report (1965), Academia Sinica.
- [12] Zi Tonggeng, Zu Xiulan, Ni Helin, Li Minghua, Miao Zialan: Study on a Small Flat Plate Thermal Diffusivity Measuring Apparatus of Inorganic Non-Metal below 1200°C. Shanghai Silicon Salt Institute Report (1965), Academia Sinica.

EXPERIMENTAL INVESTIGATION OF SIMULATING
IMPINGEMENT COOLING OF CONCAVE SURFACES
OF TURBINE AIRFOILS

Cheng-Ji-rui Wang Bao-guan

(Nanjing Institute of Aeronautics and Astronautics)

Abstract

Presented in this paper are the experimental results of impingement cooling of two aluminum targets of different size with six impingement tubes. The target simulating the leading edge of a turbine airfoil is preheated and cooled by jets of different impingement tubes at various flow rates and distances. The lumped-capacity method is used to determine the cooling rate of the aluminum target and the mean heat transfer coefficients which are in turn correlated in dimensionless parameters. Satisfactory results are obtained when Nu numbers calculated from the recommended expression are compared with those by experiments. The recommended expression is further compared with the correlated formula of Arizona State University by Metzger and those of University of Cincinnati by Ravuri and Tabakoff together with the experimental data, and it is found that the expression correlated by this paper is more or less reasonable.

FORWARD

For an aeronautical jet engine, the thrust-to-weight ratio is an important index for judging the design standard. In order to improve the thrust-to-weight ratio, it is necessary to increase the front inlet temperature of the turbine. Because the blade material cannot endure too high a temperature, it is often necessary to employ cooling techniques so that the temperature in front of the turbine can be raised as far as possible while still staying within a temperature endurable by the blade material. Air convection cooling has been the basic method for cooling the aeronautical combustion turbine blades, but for some severely heated regions on the blade (e.g. the front and rear edge of the blade) convection cooling alone is not enough. Other cooling techniques must be incorporated for local cooling. The usual

* This paper was presented at the 2nd National Engineering Thermal Physics Conference at Hangzhou in November, 1978.

method is to use local air film cooling (external cooling) or by using air jets for impingement cooling (internal cooling) directly on the front edge of the blade, or by using both. Using impingement air jet to reinforce the local cooling of the leading edge is a structurally simple, practical and easy method.

The theory of jets and experimental study has long been discussed, but the discussions are usually limited to free jet or wall jet and not about impingement jets normal to flat plates or concave surfaces. In some papers, only the flow characteristics of flat plate impingement jets are supplied while the heat exchange problems of impingement jets on plane or concave surfaces are not discussed.

From the end of the sixties to the beginning of the seventies, in order to apply impingement jets to the cooling of the leading edge of turbine airfoil some research was carried out [5-12] on the impingement cooling of concave surfaces, the majority of which was basically experimental studies. Among these experimental studies, the research works of D.E. Metzger of the University of Arizona and those of W. Tabakoff of the University of Cincinnati in the U.S. are more outstanding.

Metzger did some experimental studies on the impingement cooling of a row of circular jets on concave surfaces [6,7]. He analyzed the effect of the parameters Re , c_n/d_n , l/d , and Z_n/b on the Stanton number St (for the meaning of symbols, see the symbol explanation) and finally proposed the empirical formula [6]

$$St_{max} Re^{0.27} (l/b)^{0.52} = 0.355 \quad (1)$$

The range of applicability is $4.65 \leq l/b \leq 55.6$, $1.67 \leq c_n/d_n \leq 6.67$, $1150 < Re < 6300$. He did not include in eq. (1) quantitatively the effect of c_n/d_n and Z_n/b , but only used l/b to implement indirectly the effect of c_n/d_n and to eliminate the effect of Z_n/b by taking the

/16

maximum value of St number.

Tabakoff, et al., also carried out a more thorough analysis and study [9-12] over a period of time on the impingement cooling of semi-spherical concave surfaces. In Reference [10] he proposed

$$Nu_{d_n} = c Re_{d_n}^{0.89} Pr^{1/3} (c_n/d_n)^q (F/f) \quad (2)$$

as the standard relationship for impingement cooling of semi-spherical concave surfaces by multiple array of circular jets. In Reference [11] he proposed

$$Nu_p = 0.9113 Re_p^{0.715} (d_n/D)^{0.799} (c_n/d_n)^{-0.125} (Z_n/d_n)^{-1.15} \quad (3)$$

as the standard relationship for the impingement cooling of semi-spherical concave surface by single array of circular jets. In the above 2 equations,

$$Re_{d_n} = V \rho d_n / \mu \quad (4)$$

$$Re_p = V \rho W / \mu \quad (5)$$

where W is the length of the curved surface of the impinged concave plate, i.e.

$$W = \pi D / 2 \quad (6)$$

In eq. (2), the coefficient c and the index q are both functions of Z_n/d_n :

$$c = 1.36 \exp(-\sqrt{Z_n/d_n}) - 0.002(Z_n/d_n) - 0.153, (Z_n/d_n) \quad (7)$$

$$q = 1.159(Z_n/d_n) - 3.23 \quad (8)$$

In the formulae proposed in Reference [10,11], the diameter of the jet orifice or the length of the curved surface W of the

impinged concave surface are taken respectively as the formative dimension of Re and Nu , while the parameters such as the number of jet orifices n and the center distance c_n have not been taken into consideration. This seems to be a lack of completeness.

In this paper, we synthesized the results of the papers mentioned above and simulated the impingement cooling of the leading edge of the airfoil by cooling air by impinging against the semi-spherical concave surface with a single array of circular air jets. The experimental set up is basically based on the University of Arizona method while the data are treated primarily according to the University of Cincinnati method.

EXPERIMENT AND MEASUREMENT SET UP AND THE EXPERIMENTAL PROCEDURE

Figure 1 shows the diagram of the air passage system in the experimental set up. The air stream from the pressure stilling chamber passes through the regulator valve 4, the rotor flow rate meter 7, the air storage chamber 10 and impingement tube 17 and impinges on the test sample 16 to simulate cooling of the leading edge of the airfoil. Finally the cooling air stream is expelled to the surrounding environment. The rotor flow rate meter and the nickel-chromium-copper thermal couple have all been calibrated.

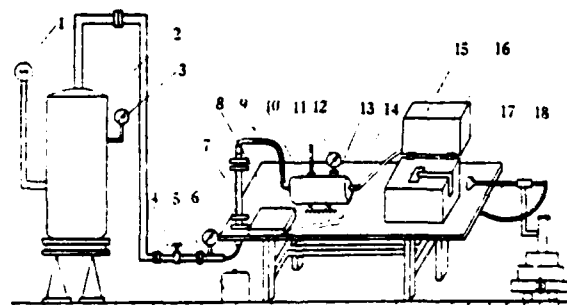


Figure 1. Diagram of the experimental set up.

Key: 1--source of air; 2--pressure-stilling chamber; 3--pressure gauge; 4--regulating valve; 5--heating oven; 6--pressure gauge; 7--rotor flow rate meter; 8--digital voltmeter; 9--soft turbine;

Key to Fig. 1 cont.: 10--air storage chamber; 11--thermometer;
12--pressure gauge; 13--work bench; 14--thermal couple;
15--insulated chamber; 16--test sample; 17--impinge tube;
18--coordinate regulating stand.

Figure 2 shows the diagram of the test piece, the impingement tube and their set up. The semi-circular concave surface on the test piece is impinged directly by the cooling air stream. Our experiment used 2 test pieces with semi-circular concave surfaces of different diameters D : $D=15\text{mm}$ and $D=11\text{mm}$. The test piece is heated first in a small electric heater. Its temperature is determined by the nickel-chromium-copper thermal couple buried in the test piece with a PZ8 digital DC voltmeter. After being heated, the test piece is removed from the electric heater and placed into the cavity of an insulated box made from Tung wood. The cover of the insulated box is then closed with only the semi-circular concave surface of the test piece exposed to the jet of the impingement tube and cooled by it. The temperature change of the test piece is displayed on the PZ8 digital voltmeter through the thermal couple. After the impingement air stream flow rate is stabilized and fixed at a required volume by adjusting the regulating valve, the instantaneous test piece temperatures are recorded with the timer and the digital voltmeter so that the variational relationship between the instantaneous temperature of the piece and time t is obtained, from which the heat exchange coefficient α of the impingement jet on the test piece averaged over the semi-circular concave surface is found. This α value corresponds to the average heat exchange coefficient at a certain flow rate. Thus different α values for different flow rates are obtained. /167

The width d of the impingement tube is $1/2$ of the diameter of the semi-circular concave surface of the corresponding test piece, i.e. $d/D=1/2$. Hence there are 2 different widths for the impingement tube: $d=7.5$ and $d=5.5\text{mm}$. The orifice diameter of

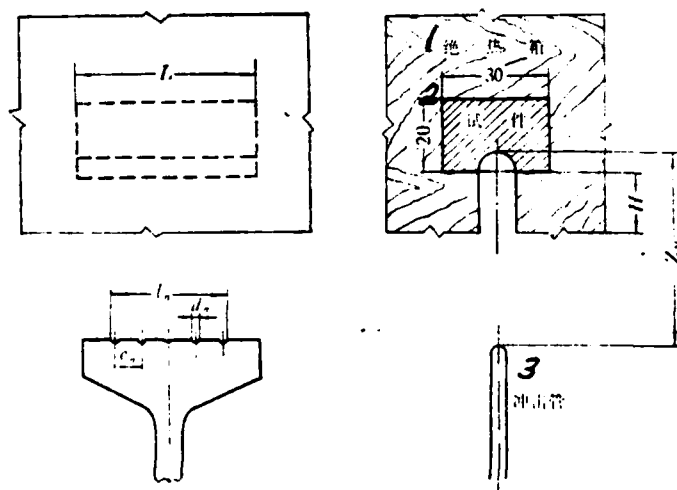


Figure 2. Diagram of test piece and impingement tube arrangement.

Key: 1--insulating box; 2--test piece; 3--impingement tube.

the impingement tube is determined by a tool microscope and an average value d_n is then obtained. For an impingement tube of the same width, there are 3 different center distances C_n i.e., $C_n/d_n = 1.67, 3.33$ and 6.67 . The impingement tube is fixed on a tri-directional coordinate regulator stand 18 so that the distance Z_n from the impingement tube to the semi-circular concave surface of the test piece may be adjusted at will. Each impingement tube is first adjusted to be at the given distance Z_n . Then a set of average heat exchange coefficients corresponding to a given flow rate is measured and their average value is taken to be the average heat exchange coefficient at that flow rate to reduce accidental error. This is done for different flow rates. Then the above experiment is repeated for another Z_n value. In our experiment there are 2 test pieces and for each test piece, there are 3 impingement tubes. Five Z_n values are used for each tube and for each Z_n value, experiments are carried out for five different flow rates. Hence, one empirical formula may be found for each Z_n value, for a total of 30 empirical formulae. (for detail, see Table 1).

TREATMENT OF EXPERIMENTAL DATA

The test pieces are made from pure aluminum. As the thermal conductivity of aluminum blocks is large and the test piece dimension is small, the average heat exchange coefficient obtained from this experiment is mainly between 170 to $1200 \text{ Kcal/m}^2 \cdot \text{time} \cdot \text{degree}$. Preliminary estimation gives Biot number $B_i = 0.025 \sim 0.175$, averaging about 0.1 . The non-uniformity in temperature is no more than 2.5% . The characteristic dimension of the aluminum block is obtained from the ratio of the aluminum block volume to the cooled heat exchange surface. We may assume that the spatial temperature distribution of the aluminum block is basically uniform so that the cooling rate of the aluminum block may be calculated from the concentrated total thermal capacity method. The thermal equilibrium equation of the test piece during cooling is

$$-G_{AL}C_{AL} \cdot dT/dt = \alpha F(T - T_\infty) \quad (9)$$

Integrating the above equation, we get

$$\ln[(T_i - T_\infty)/(T - T_\infty)] = \alpha F(t - t_i)/G_{AL}c_{AL} \quad (10)$$

where T_i is the initial temperature at the initial instantaneous time t_i , G_{AL} and c_{AL} are respectively the weight and specific heat of the aluminum block. Let

$$c = G_{AL}c_{AL}/F,$$

and take into account of heat loss by leakage, the above equation may be re-written as

$$\alpha = [c/(t - t_i)] \ln[(T_i - T_\infty)/(T - T_\infty)] - \quad (11)$$

The leakage heat loss is measurable: Place the aluminum block into the insulated box after heating, block the semi-circular concave surface with Tung wood and let it cool by itself. The required time interval for T_i to decrease to T is measured and the leakage heat loss is estimated from it. Experiment indicates that the leakage heat loss is very small, about 3% of the heat exchange coefficient at the minimum flow rate. It may be neglected within the accuracy of our experiment, when the impingement jet flow rate has stabilized, time measurement with the second timer is started (take $t_i=0$) and simultaneously the instantaneous temperature T_i of the aluminum block is also recorded. Then the aluminum temperatures at a sequence of pre-arranged time intervals are recorded and a set of heat exchange coefficients for a given value of impingement jet flow rate is calculated according to Eq. (11) from which the arithmetic average value is taken to be the average heat exchange coefficient at this flow rate. The Nu number is then calculated

$$Nu = \alpha d_e/\lambda = \alpha \cdot 2b/\lambda \quad (12)$$

where d_e is the equivalent diameter when the single array circular

hole is converted into the equivalent 2-dimensional jet channel and b is the width of the equivalent 2-dimensional jet channel, i.e.

$$b = n(\pi/4)d_n^2/l_n \quad (13)$$

The Re number of the jet is

$$Re = V\rho d_n/\mu = (G \cdot 2b)/\mu g \quad (14)$$

The volume flow rate measured by the rotor flow rate meter is standardized by the standard state $P_0=10332 \text{ kg/m}^2$, $T_0=293\text{K}$. This volume flow rate value should be corrected according to the air stream state during experiment and converted to the weight flow rate G according to the current air stream pressure and temperature with the following equation:

$$G = 0.2029 Q_0 \sqrt{P/T} \quad (15)$$

where P is the absolute pressure (kg/m^2) of the air storage chamber, T the absolute temperature (K) of the air storage chamber and Q_0 the volume flow rate at STP.

According to similarity theory, the heat exchange coefficient may be expressed with the following equation

$$Nu = f(Re, Pr, \varphi_1, \varphi_2, \varphi_3, \dots) \quad (16)$$

For air, the Prandtl number Pr basically does not vary very much. We may take its value as fixed. $\varphi_1, \varphi_2, \varphi_3, \dots$ are geometrical similarity standards. According to experimental analysis, we take the following similarity standards:

$\varphi_1 = Z_n/b$, the relative distance between the test piece and jet orifice;

$\rho_2 = c_n/d_n$, the relative center distance of the jet orifices;

$\phi = F/f$, ratio of the semi-circular concave surface area to the total cross-sectional area of the jet orifice, which reflects the effect of the diameter of the concave surface on α . Eq. (16) may be written as

$$Nu = A_1 Re^{1/2} (c_n/d_n)^{1/2} (Z_n/b)^{1/2} (F/f)^{1/2} \quad (17)$$

For a given impingement tube and test piece, c_n/d_n and F/f 's values are all fixed. For a given Z_n/b Eq. (17) may be re-written as

$$Nu = A_0 Re^{1/2} \quad (18) \quad /169$$

where

$$A_0 = A_1 (c_n/d_n)^{1/2} (Z_n/b)^{1/2} (F/f)^{1/2} \quad (19)$$

EXPERIMENTAL RESULTS AND ANALYSIS

Table 1 shows the empirical formulae obtained from the data of 6 impingement tubes at 5 different Z_n/b values for 5 different flow rates in the experiment, after re-ordered into the form of $Nu = A Re^m$. Because of the effects of different experimental conditions and measurement errors, etc., the A and m values of each formula will not be the same.

Figures 3 through 7 show the comparison between experimental data and the empirical formula obtained from them for the 6 impingement tubes at a fixed Z_n/b value (3 types with $c_n/d_n = 1.67, 3.33, 6.67$) Details about the meaning of the symbols in the figures may be found in Table 1. Generally speaking, Nu number decreases with the increase of Z_n/b , but Z_n/b 's value varies from 3 to 80 while c_n/d_n from 1.67 to 6.67. Hence, relatively speaking, the effect of Z_n/b on the Nu number is not as large as that of c_n/d_n .

Table 1. Detailed table of Figures 3-6.

Impingement tube no.	Line Number	Symbol	c_n/d_n	F/f	Z_n/b	Coeff. A	Index m
1 $D = 11 \text{ mm}$, $F = 854.9 \text{ mm}^2$	1	○	1.67 ($n = 25$)	36.7	5	0.0384	0.784
	2	●			10	0.265	0.537
	3	◐			20	0.165	0.596
	4	◑			40	0.0374	0.772
	5	⊖			80	0.0121	0.871
2	6	△	3.33 ($n = 13$)	70.5	5	0.0344	0.741
	7	▲			10	0.0618	0.667
	8	▲			20	0.0464	0.702
	9	▲			40	0.0531	0.670
	10	▲			80	0.0412	0.687
3	11	◇	6.67 ($n = 7$)	124	5	0.0415	0.674
	12	◆			10	0.0464	0.657
	13	◊			20	0.0761	0.593
	14	◊			40	0.0673	0.604
	15	◊			80	0.0561	0.619
4 $D = 15 \text{ mm}$ $F = 1175.5 \text{ mm}^2$	16	⊙	1.67 ($n = 19$)	36	3	0.0596	0.724
	17	⊖			5	0.0416	0.767
	18	●			10	0.0580	0.728
	19	◐			20	0.0841	0.670
	20	⊖			40	0.0254	0.796
5	21	△	3.33 ($n = 10$)	68.3	5	0.0600	0.671
	22	▲			10	0.0445	0.699
	23	▲			20	0.0500	0.686
	24	▲			40	0.0280	0.754
	25	▲			80	0.0432	0.678
6	26	⊙	6.67 ($n = 5$)	135	5	0.0478	0.648
	27	◆			10	0.0260	0.715
	28	◊			20	0.0410	0.657
	29	◊			40	0.0276	0.701
	30	⊙			80	0.0409	0.648

In Figure 7, with the exception of line 16 labeled with the experimental value of $Z_n/b=3$, the other 5 lines all are the experimental data at $Z_n/b=80$.

From Figures 3 through 7, we can observe the effect of c_n/d_n on Nu: the Nu number decreases significantly with the increase of c_n/d_n . Under the condition of equal c_n/d_n value, the Nu numbers of test pieces are relatively close. The Nu number of the test piece with D-11mm is slightly higher than that of the test piece with D-15mm. From this it can be seen that Nu number is related to the heat exchange surface area of the test piece, and hence, related to the radius of the semi-circular concave surface of the simulating airfoil's leading edge.

Metzger [6] has pointed out that the average heat exchange coefficient of the impingement jet varies with Z_n/b ; for a fixed value of c_n/d_n , a maximum heat exchange coefficient is found for some Z_n/b value. After passing through the value, α decreases with increment of Z_n/b .

Figure 3. Diagram of Nu-Re for various impingement tube.

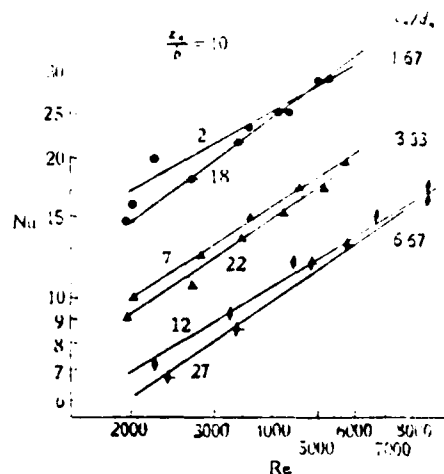
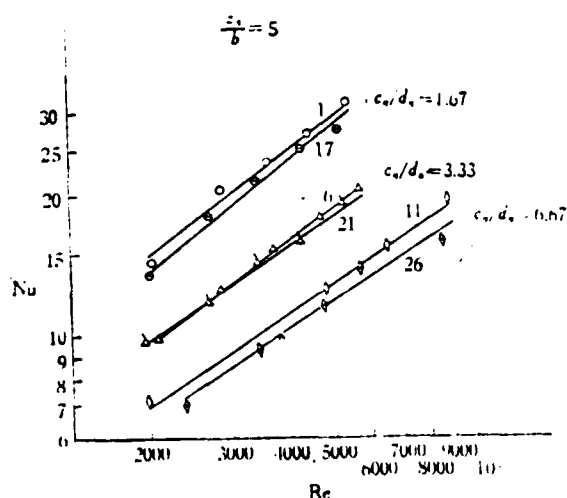


Figure 4. Diagram of Nu-Re for various impingement tube.

Figure 5. Diagram of Nu-Re
for various impingement tube.

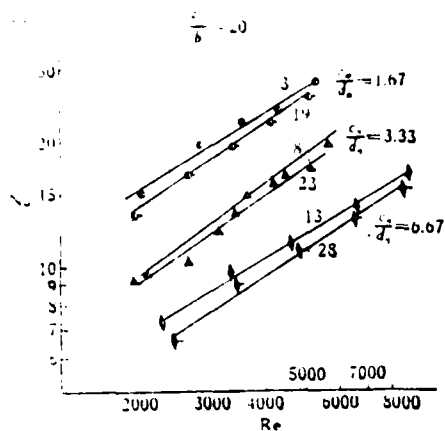


Figure 6. Diagram of Nu-Re
for various impingement tube.

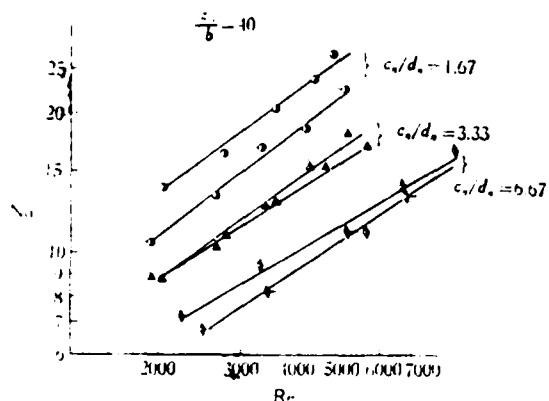


Figure 7. Diagram of Nu-Re
for various impingement tube.

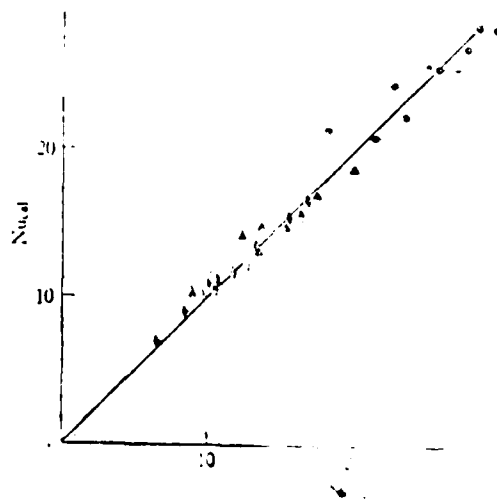
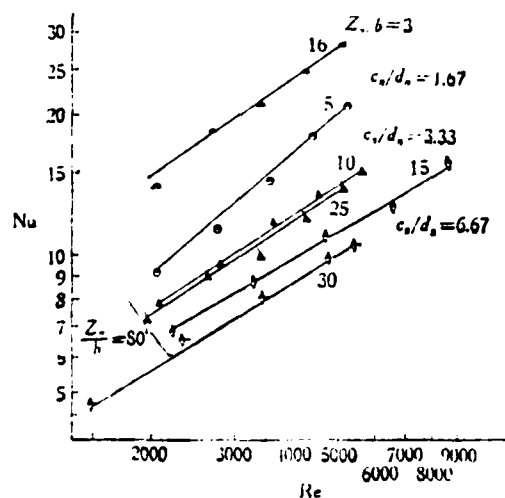


Figure 8. Experimental
data for
(21) $Re = 10$

AD-A122 037

JOURNAL OF ENGINEERING THERMOPHYSICS (SELECTED
ARTICLES)(U) FOREIGN TECHNOLOGY DIV WRIGHT-PATTERSON
AFB OH 04 NOV 82 FTD-ID(RS)T-1011-82

272

UNCLASSIFIED

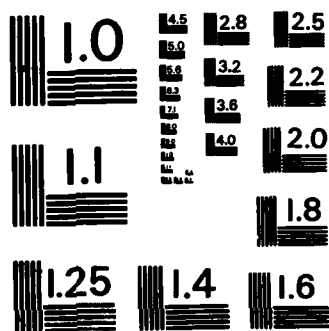
F/G 13/7

NL

END

FORMED

PTD



MICROCOPY RESOLUTION TEST CHART
NATIONAL BUREAU OF STANDARDS-1963-A

The value of Z_n/b producing the maximum heat exchange coefficient is related to c_n/d_n . When $c_n/d_n = 1.67$, the maximum value of heat exchange coefficient occurs at $1 \leq Z_n/b \leq 3$; when $c_n/d_n = 3.33$, it occurs at $2 \leq Z_n/b \leq 5$ and when $c_n/d_n = 6.67$, it occurs at $5 \leq Z_n/b \leq 11$. In our experiment, only for the test piece with $D=15\text{mm}$ did it reach $Z_n/b=3$ once when $c_n/d_n = 1.67$. With the exception of this, it is very difficult to achieve $Z_n/b=3$ in the experiment; therefore it is not possible to determine the Z_n/b value through experiment that produces the maximum heat exchange coefficient. The above is the empirical formulae obtained for each impingement tube at a given value of Z_n/b in the experiment: /171

$$Nu = ARe^m,$$

The values of A and m vary for various values of c_n/d_n and Z_n/b ; hence, 30 empirical formulae are obtained. They are not convenient to use although it is easier to compare them to experimental data. Hence, we took all the data (150 experimental points) obtained from experiment and put them in a matrix form according to the least square method based on Eq. (17) and finally find the solution through the electronic computer with a program (which is here omitted). The coefficients and indices in Eq. (17) are obtained respectively as

$$A_1 = 0.269, A_2 = 0.666, A_3 = -0.401, A_4 = -0.065, A_5 = -0.201. \quad (20)$$

i.e.

$$Nu = 0.269Re^{0.666}(c_n/d_n)^{-0.401}(Z_n/b)^{-0.065}(F/f)^{-0.201} \quad (21) \quad /17$$

The applicable ranges of the above equation are:

$$1950 < Re < 8900, 1.67 \leq c_n/d_n \leq 6.67, 3 \leq Z_n/b \leq 80, 36 \leq F/f \leq 135.$$

The qualitative temperature is taken as the total temperature (air temperature of the air storage chamber) of the impingement air stream in front of the orifice. From the index of Eq. (21) one can see intuitively that besides Re , the factor that affects

the heat exchange coefficient the most is c_n/d_n while the effect due to Z_n/b is the least. To test the agreement of the composite relation (21) with experimental data, we compare the Nu_{cal} calculated from Eq. (21) to the corresponding Nu_{exp} measured from experiment. The experimental data points are shown with the symbols in Table 1, as shown in Figure 8. From Figure 8, it can be seen that the maximum deviation between Nu_{cal} and Nu_{exp} is within $\pm 17\%$. 90% of the experimental points fall within $\pm 8\%$. This result is satisfactory. The index of Re in the composite formula (17) is precisely the middle value of the 30m values in the empirical formula listed in Table 1. The size of the index shows that the flow state of the jet stream is close to turbulent flow.

If the Eq. (21) is to be extended to the impingement cooling by other fluid, it can be done by the traditional method by adding on the LHS of the equation a factor $Pr^{1/3}$ as a correction. The coefficient A_1 should be changed to 0.326 namely

$$Nu = 0.326 Re^{0.666} Pr^{1/3} (c_n/d_n)^{-0.401} (Z_n/b)^{-0.065} (F/f)^{-0.211} \quad (21a)$$

COMPARISON EQ.(21) OF THIS PAPER TO REFERENCE [6] AND [11]

Metzger pointed in Reference [6] that the average heat exchange coefficient varies with Z_n/b . Yet when the data are organized, only the largest heat exchange coefficient value for each Z_n/b value and the effect of Z_n/b is not incorporated with the formula. The formula realizes the effects of c_n/d_n and F/f indirectly through the parameter $1/b$. In practical applications, the value of Z_n/b that gives the maximum heat exchange coefficient is usually unknown and the effects of c_n/d_n and F/f cannot be expressed in the formula.

In order to make it easier to compare Eq. (1) to the Eq. (21) recommended in our paper and to the experimental data, it is necessary to transform the equation as follows:

$$Nu_{max} Re^{0.2} (1/b)^{0.2} = 0.355 Re Pr$$

or

$$Nu_{max} Re^{0.77} (l/b)^{0.52} = 0.355 Re Pr \quad (22)$$

Combining the case of $D=15\text{mm}$ in our experiment, in air $Pr=0.7$ in Eq. (22)

$$l = (1/2)(1/2)(\pi D) = 11.76\text{mm},$$

b is related to the impingement tube used. Substituting the b values corresponding to the 3 c_n/d_n values into Eq. (22), the Metzger equation may be changed to:

$$\left. \begin{array}{l} \text{(a) 当 } c_n/d_n = 1.67 \text{ 时, } Nu_{max} = 0.0577 Re^{0.73} \\ \text{(b) 当 } c_n/d_n = 3.33 \text{ 时, } Nu_{max} = 0.04025 Re^{0.73} \\ \text{(c) 当 } c_n/d_n = 6.67 \text{ 时, } Nu_{max} = 0.0307 Re^{0.73} \end{array} \right\} \quad (23)$$

Figure 9 shows the comparison of Eq. (21) in this paper to the Metzger Eq.(23). In the diagram, it can be seen that: When $c_n/d_n = 1.67$, Eq. (23) is close to Eq. (21) and to the experimental data in this paper. When $c_n/d_n = 3.33$, Eq. (23) is slightly higher than our Eq. (21) or (18) at $Z_n/b=5$, and when $c_n/d_n = 6.67$, Eq. (23) deviates more from (21) or (18). This is because the heat exchange coefficient in Eq. (23) is meant to be the maximum value. When $c_n/d_n = 1.67$, the maximum value occurs when Z_n/b is between 1 and 3; hence, Eq. (23) is closer to Eq. (21) at $Z_n/b=3$. When $c_n/d_n = 6.67$, the maximum value situation did not occur and Eq. (23) is higher than Eq. (21). Through comparison, it is recognized that it is impossible to include all the different geometrical conditions with a single geometric parameter l/b .

Figure 9. Comparison of Eq. (21) and Eq. (23) of Reference [6].

Key: 1--our Eq. (21);
2--Eq. (23), Ref. [6].

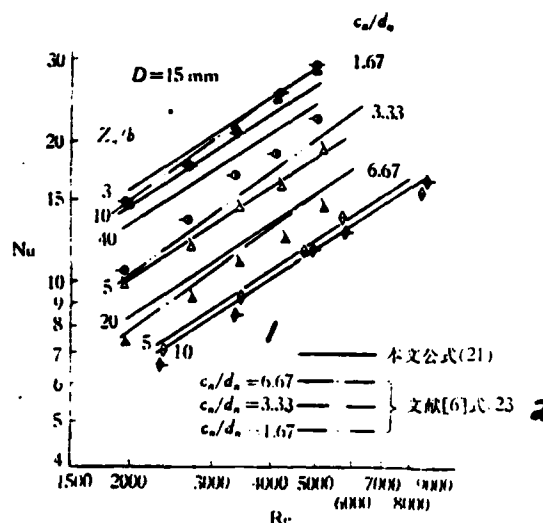
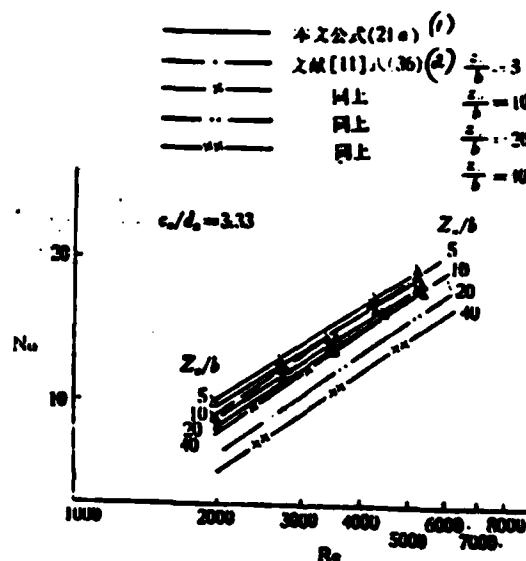


Figure 10. Comparison of Eq. (21a) and Eq. (3b) of Ref. [11].

Key: 1--our Eq. (21a);
2--Eq. (3b, Ref. [11].



The empirical Eq. (3) proposed in Reference [11] covers the experimental range

$$c_a/d_a = 2.5-5.0 \quad Z_a/d_a = 2-6$$

For the convenience of making comparisons, we choose our experimental data closer to the experimental range of Eq. (3):

$$D = 15\text{mm}, c_a/d_a = 3.33, Z_a/b = 5, 10, 20$$

and 40 (corresponding to

the cases of $Z_n/d_n = 1.25, 2.5, 5.0$ and 10.0 in Reference [11]. Eq. (3) must also be changed to the dimension $2b$ adopted in our paper:

$$Nu = 0.8113Re^{0.715}(W/2b)^{-0.285}(d_n/D)^{0.790}(b/d_n)^{-0.135}(Z_n/b)^{-0.135}(c_n/d_n)^{-0.126} \quad (3a)$$

Since

$$\begin{aligned} \bar{W} &= \pi D/2 = 3.14 \times 15/2 = 23.55 \text{ mm} \\ d_n &= 1.48 \text{ mm}, \quad b = 0.37 \text{ mm}, \quad F/f = 68.3 \end{aligned}$$

Substituting the above values in Eq. (3a) and simplifying, we get

$$Nu = 0.0589Re^{0.715}(c_n/d_n)^{-0.126}(Z_n/b)^{-0.136} \quad (3b)$$

Substituting again $F/f=68.3$ into Eq. (21), we get after simplification

$$Nu = 0.1153Re^{0.666}(c_n/d_n)^{-0.401}(Z_n/b)^{-0.065} \quad (21a)$$

Figure 10 shows the comparison between our (21a) and 3b) of Reference [11] with the experimental data in our paper also indicated in the diagram. From the diagram it can be seen that Eq. (3) of Reference [11] is lower than Eq. (21) recommended in our paper and the experimental data, and is close only for the cases of $Z_n/b=5$ and 10. This is apparently due to the fact that Eq. (3) in Reference [11] is only applicable for $Z_n/d_n = 2-6$ which corresponds to the case of $Z_n/b = 8-24$. Therefore when $Z_n/b > 20$, Eq. (3) is not really applicable.

Since the impingement jets introduced in Reference [10] have been multiple array orifices, it is too different from our experimental environment and no comparison can be made.

Our major conclusions are as follows:

1. The major parameters affecting the impingement heat exchange coefficient are Re , c_n/d_n , Z_n/b and F/f . The geometric parameters having the largest effect on Nu number is c_n/d_n , next is Z_n/b and the least is Z_n/b .

2. When the experimental data are treated with the least square method through computer calculations, the standard relational equation obtained is

$$Nu = 0.269 Re^{0.444} (c_n/d_n)^{-0.401} (Z_n/b)^{-0.065} (F/f)^{-0.201}$$

3. When the results calculated with the above equation are compared to the experimental data in this paper, basic agreement is obtained. When the above equation is compared to those recommended in Reference [6] and [11], our equation is considered to be closer to the experimental data.

4. The equation proposed in our paper basically includes a number of factors affecting the heat exchange coefficient of impingement jet in a composite, standardized relational formula. It has a definite practical value.

SYMBOL EXPLANATION

A, \bar{A}_0, A_1, \dots constant	P absolute pressure
b equivalent 2-dimensional jet	Pr Prandtl number $Pr = \mu g c_p / \lambda$
c coefficient $c = G_{ALCAL}/F$	Q_0 Volume flow rate at STP ($P_0 = 10332$, $T = 293K$)
c_n center distance of impingement tube orifice	q index, see Eq. (2) and (8)
c_{AL} specific heat of aluminum	Re Reynold number $Re = V \rho d_n / \mu = G \cdot 2b / \mu g$
D diameter of semi-circular concave surface of test piece	Re_p $Re_p = V \rho W / \mu$
	T instantaneous time

d	impingement tube thickness	St	Stanton number $St = \alpha / V \sqrt{c_p} (3600)$
d _e	equivalent diameter		$St_{max} St_{max} = \alpha_{max} / V \sqrt{c_p} (3600)$
d _n	jet orifice diameter	T _i	initial temperature of test piece
F	heat exchange surface area	T _∞	total temperature or ambient temperature of jet in the air storage chamber
f	jet orifice total cross-sectional area	t	time
G	jet flow rate by weight	V	velocity
G _{AL}	weight of aluminum block (test piece)	W	arc length of semi-circular concave surface of the test piece $W = \pi D/2$
g	gravitational acceleration	Z _n	distance from jet orifice outlet to test piece
L	length of test piece	α	average heat exchange coefficient
l	length of semi-circular arc of the heat exchange surface of test piece $l = (1/2)(\pi D/2)$	λ	thermal conductivity
l _n	outer distance between the 2 ends of the impingement tube	ρ	density
m	power index	μ	dynamic viscosity
Nu	Nusselt number $Nu = \alpha \cdot 2b/\lambda$		
n	number of jet orifices on the impingement tube		

REFERENCES

- [1] W. Tollmien, "Calculation of Turbulent Expansion Process" NACA TM-1085, 1945.
- [2] Xie Xiangchuen: Theory and Computation of Turbulent Jet Stream, Science Publishing House, 1975.
- [3] J. W. Gaunter et al., "Survey of Literature on Flow Characteristics of A Single Turbulent Jet Impinging on a Flat Plate" NASA TN D-5652, 1970.
- [4] H. Hrycak et al., "Experimental Flow Characteristics of a Single Turbulent Jet Impinging on a Flat Plate" NASA TN D-5690, 1970.
- [5] R. E. Chupp, et al., "Evaluation of Internal Heat Transfer Coefficient for Impinging Cooled Turbine Airfoils" J. Aircraft, Vol. 6, 1969, pp. 203-208.
- [6] D. E. Metzger, et al., "Impingement Cooling of Concave Surfaces With Lines of Circular Air Jets", J. Eng. for Power, Vol. 91, 1969, pp. 149-158.
- [7] D. E. Metzger, et al., "Impingement Cooling Performance in Gas Turbine Airfoils Including Effects of Leading Edge Sharpness" J. Eng. for Power, Vol. 94, 1972, pp. 216-225.
- [8] C. dup Donaldson, et al., "A Study of Free Jet Impingement" J. Fluid Mechanics, Vol. 45, Part 3, 1971, pp. 477-512.
- [9] W. Clewenger and W. Tabakoff, "Investigation of Heat Transfer Characteristics of Two-Dimensional Jet Impinging on a Semi-Cylinder" AD-697165, 1969.
- [10] W. Tabakoff, et al., "Heat Transfer by a Multiple Array of Round Jets Impinging Perpendicular to a Concave Surfaces" AD-727730, 1971.
- [11] B. Ravuni and W. Tabakoff, "Heat Transfer Characteristics of a Row of Air Jet Impinging on the Surfaces on the Inside of a Semi-circular Cylinder" AD-718794, 1971.
- [12] W. Tabakoff and W. Clewenger, "Gas Turbine Blade Heat Transfer Augmentation by Impingement of Air Flowing Various Configurations" ASME Paper No. 71-GT-9, 1971.

EXPERIMENTAL INVESTIGATION OF TOTAL-PRESSURE
LOSS AND AIRFLOW DISTRIBUTION FOR GAS
TURBINE COMBUSTORS

Fan Zuo-min, Chao Zhi-fang
(China Gas Turbine, Establishment)

Abstract

A lot of theoretical and experimental investigations in relation to the subject have been done, and the results demonstrate that the present solution for the one dimensional simultaneous equations is reasonable. Both the widely current flow drag calculating method and the hole blank off experimental method which was developed on the base of the above said method have some defects.

This paper provides a simple calculating method which utilizes the mean flow coefficient. The method is simple in calculation, clear in concept and has a wide range of applications. The calculating result is in good agreement with the solution for the one dimensional simultaneous equations.

1. EXPERIMENTAL SET UP, TEST PIECE AND MEASUREMENT SCHEME

/185

This experiment was carried out on a water flow-simulation experimental unit. The test piece is a 2-dimensional test section made of organic glass with the 2 passages separated from the flame tube with a separator.

The flow field of the 2 passages is measured by the total static pressure difference. On each cross-sectional area, total pressure is measured at 9 points. The flow rate coefficient over the cross-sectional area is standardized a priori with Venturi tube flow rate; then the flow rate through each cross-section may be measured during the actual experiment. The flow rate through a small orifice is determined by the difference between the flow rates of the passage cross-section before and after the orifice.

This paper was presented at the 2nd National Engineering Thermophysics Conference at Hangzhou in November, 1978.

The orifice jet velocity and orifice flow rate coefficient are treated according to the cross-section area parameter before the orifice.

2. EXPERIMENTAL RESULTS AND ANALYSIS

Figure 1 shows the relation between the orifice flow rate coefficient c and flow rate parameter F_p . This result is very close to the data given in most papers (e.g. Reference [1]) with the c value at large F_p slightly higher. (Note: the internal flow of the flaming tube in our experiment is not zero.)

Figure 2 shows the relation between the orifice flow rate coefficient c^0 and area parameter. The curve given in Reference [2] is also drawn in this diagram (Miller curve). From the diagram, it can be seen that for small G_p values, the experimental values of the orifice flow rate coefficient are far lower than the Miller values.

The variational relations between the flow rate distribution W_1 of various test pieces and the relative area of the orifice of the flaming tube \bar{A} are shown in Figure 3 and Figure 4. We only emphasize one point here: namely that for a fixed a_1 value, the bigger the curve X_{\max} , the more curved is the curve $W_1 = f(\bar{A})$. The smaller the value of X_{\max} , the more $W_1 = f(\bar{A})$ approaches a straight line of 45° .

Figures 5 and Figure 6 respectively, show the value of the combustion chamber friction coefficient ξ_a . It can be seen that in general, the total pressure loss of the combustion chamber is usually larger than the velocity head at the inlet of the 2 passages.

Now we shall discuss an experimental method introduced in some references to measure the flow rate distribution in a

/186

combustion chamber by a orifice-blocking method which is the so-called orifice blocking method. The method is as follows: the total friction coefficient ξ in the combustion chamber is measured first. Then the i th row of orifices is blocked and the friction coefficient ξ is again measured. From the equation in Reference [2], we should mention that this method is quite questionable. In fact, we can easily see that this method basically is incapable of showing the difference of the flow rate coefficient C corresponding to the different orifice arrays at positions in front of or behind the flaming tube. Experimental results verified this completely. From Table 1 we see that the flame tube flow rate distribution measured by the orifice blockage method is basically the same for each array of orifices. In other words, the flow rate distribution measured by the orifice blockage method is in fact distributed according to area. It deviates quite severely from accurately measured experimental results (respectively, 0.013 and 0.504). Of course, when the total orifice area of the flaming tube is very small, the law of actual flow rate distribution is very close to be law of distribution by area. Here the orifice block method naturally agrees with the experimental value, but what meaning does this agreement have?

Figure 1. Relation between orifice flow rate coefficient and flow parameter.

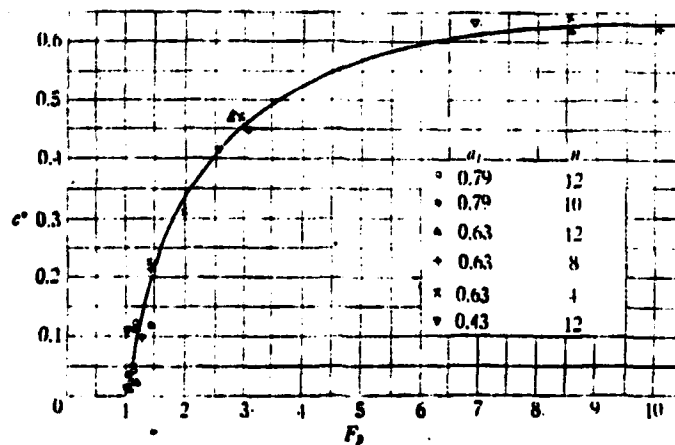


Figure 2. Relation between orifice flow rate and area parameter.

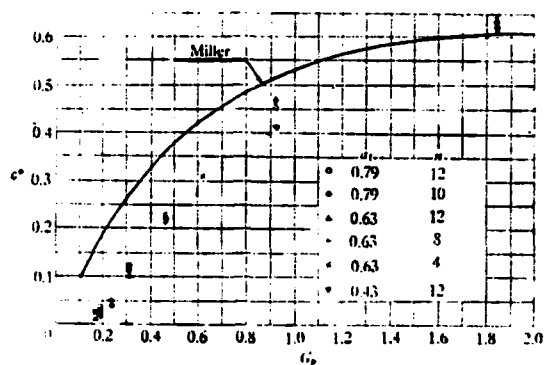


Figure 3. Variation of flow rate vs \bar{A} ($\sigma_t = 0.63$)

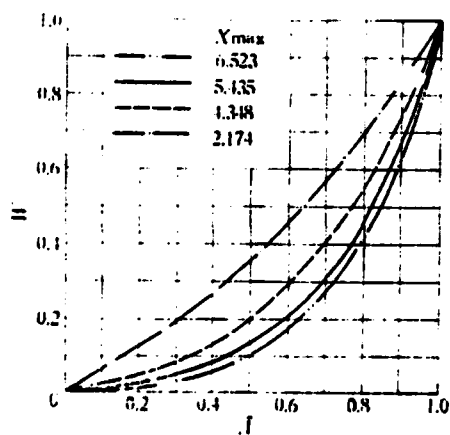
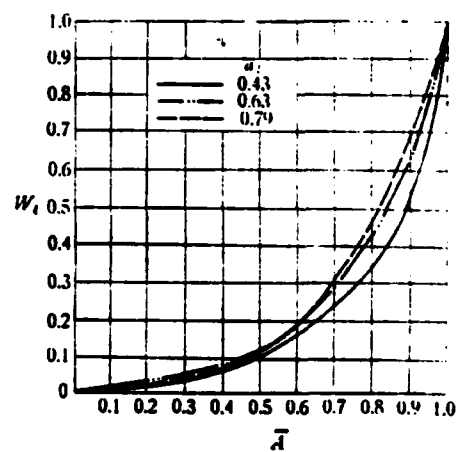


Figure 4. Variation of flow rate distribution with \bar{A} ($X_{max} = 6.523$)



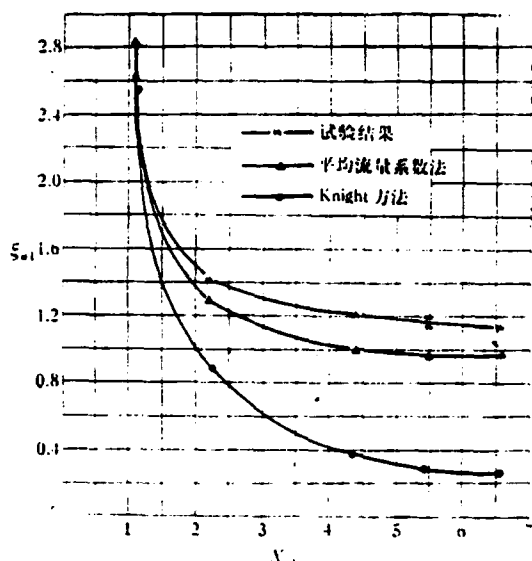


Figure 5. Relation between friction coefficient ξ_{a1} and V_{max} ($d_1=0.63$).

Key: —x— experimental result
 —▲— average flow rate coefficient method
 —●— Knight method

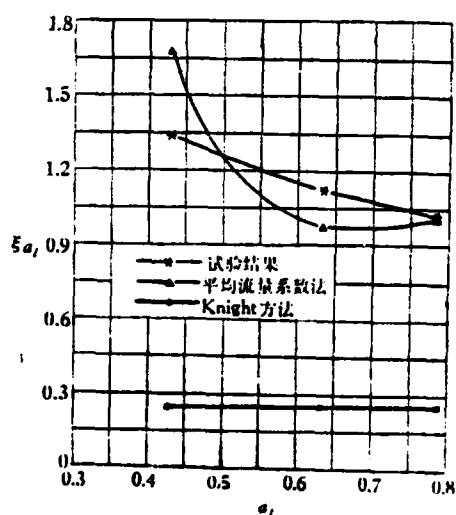


Figure 6. Comparison between calculated values and experimental values of ξ_{a1} ($X_{max}=6.523$).

Key: —x— experimental result
 —▲— average flow rate coefficient method
 —●— Knight method

$$\Delta Q_i = 1 - (\xi/\xi')^{0.5}$$

Table 1. Experimental result of orifice blockage method

($a_t = 0.63$, $X_{max} = 6.523$)

parameter experimental method	ξ	ξ'	$\Delta W_{1,2}$	$\Delta W_{11,12}$
no orifice is blocked	1.13	--	0.0420	0.504
1st and 2nd row of orifices blocked	--	1.18	0.0214	--
11th & 12th row of orifices blocked	--	1.16	--	0.013

METHOD OF CALCULATING THE COMBUSTION CHAMBER FLOW RATE DISTRIBUTION AND THE AVERAGE FLOW RATE COEFFICIENT OF TOTAL PRESSURE LOSS

The relative flow rate inside the flame tube of the i cross-section combustion chamber is

$$W_{ii} = 1 - V_{ai}A_{ai}/V_rA_r = 1 - v_{i0}\omega a_{ai} \quad (3-1)$$

here

$$\omega = v_{ai}/v_{i0} \quad (3-2)$$

nce

$$v_{i0}c_0a_{i0} + v_{a1}a_{a1} = 1$$

/1

herefore

$$v_{i0} = 1/(c_0a_{i0} + \omega_{max}a_{a1}) \quad (3-3)$$

From Eq. (3-1) and (3-3), we know that we only need to know the ω_1 value in order to compute the W_{11} value. It is not hard to see that what the value of ω_1 represents is the average flow rate coefficient of all the orifices behind the i th array of orifices. The results of calculation and experiment indicate that the ω_1 value may be expressed as a function of the $X\phi$ value, where

$$\phi = v_{j02}/v_{j0} \quad (3-4)$$

$$X_i = \sum_{j=i}^n A_{h,j}^2 / A_{h,i} = 1/G_p \quad (3-5)$$

Figure 7 shows the ω curve obtained from the experimental values. The horizontal coordinate in the plot is $X\phi$ and the vertical coordinate is $\omega_e, \omega_e = \epsilon_{\max} \cdot \omega$. In the Eq. ϵ_{\max} is the coefficient determined by ϕX_{\max} , see Figure 8. Notice that the air-inlet orifice in the head section of the flame tube is not included in the value of X_{\max} . From the diagram it can be seen that all the experimental points of various a_1 and X_{\max} values basically fall on one curve. Thus curve may be represented as ($\phi X_{\max} \leq 11$) .

$$\omega_e \approx 0.895(1 - e^{-0.8\phi X}) \quad (3-6)$$

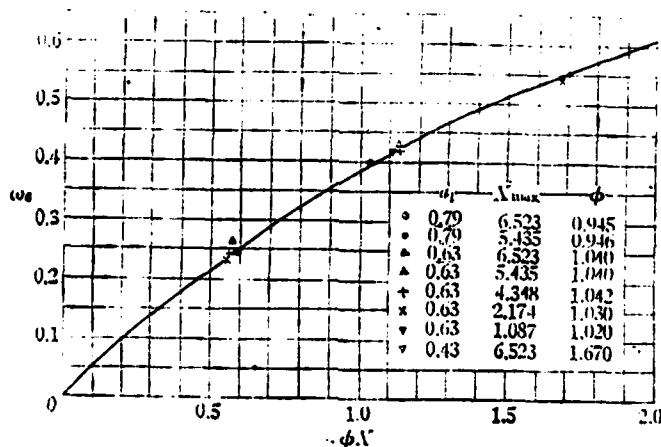


Figure 7a. Relation between ω_e and X (for small $X\phi$ values).

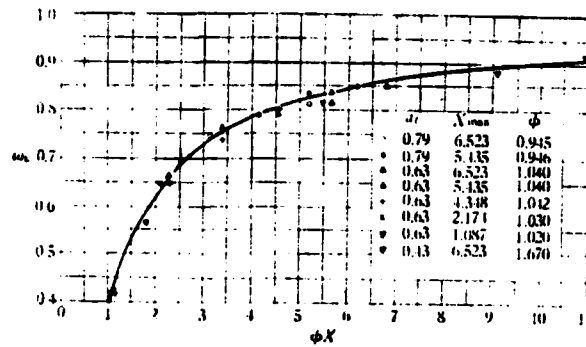


Figure 7b. Relation between ω_ϵ and ϕX (for large $X\phi$ values).

The ϵ_{max} curve in Figure 8 may be approximated as

/18

$$\epsilon_{max} \approx 0.725 + 0.090\sqrt{\phi X_{max} - 1} \quad (3-7)$$

From the definition of Eq. (3-2), we can see that: $\omega_{ex}=0$, for the last array of orifice cross-section of the flame tube, i.e., the outlet cross-section of the combustion chamber, and $\omega_{max} \rightarrow 1$ for the cross-section of the first row of orifices of the flame tube when $\phi X_{max} \rightarrow \infty$.

Since the coordinate parameter of the ω curve is ω_ϵ and not directly ω , hence it is more convenient to write (3-1) in the following form

$$W_{ii} = 1 - \frac{\omega_{\epsilon i} a_{\epsilon i}}{c_0 a_{\epsilon 0} \epsilon_{max} + \omega_{\epsilon max} a_{\epsilon i}} \quad (3-8)$$

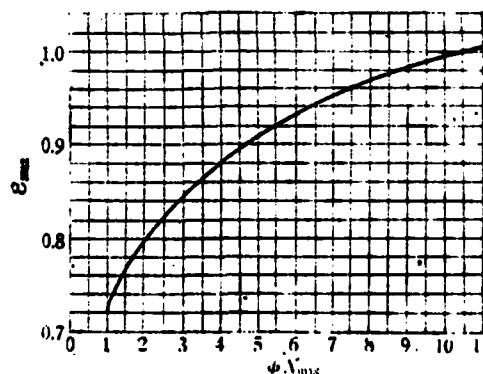


Figure 8. Relation between ϵ_{max} and ϕX_{max} .

The w curve in Figure 7 is obtained from the data for cooling air state (water flow simulation) when there is no vortex generator on the test piece. However, the large quantity of computational results indicate that the w curve in Figure 7 is truly a meaningful curve in the general sense. It is capable of taking into account the effects of many factors such as a_i, X_{max}, A_{h0} and combustion heat release, etc., and for flame tube or combustion chamber with variable cross-sectional area, the w curve above and some of the computational formula (including the dynamic equation) to be introduced below are still applicable. Their degree of accuracy is even surprising. We shall illustrate this point below by using as a concrete example a staged flame tube. The combustion chamber has constant cross-section ($a_{hi} + a_{li} = \text{const}$). The flame tube is staged with 6 rows of orifices (all with flat surface $a_{hi} = \text{const} = 0.1333$) except the vortex generator ($c_0 = 0.60, a_{h0} = 0.08$). For the two front rows, $a_i = 0.5$, the middle two rows, $a_i = 0.6$, and the last 2 rows $a_i = 0.7$. Heating ratio is $\theta = 1$. The comparison of the calculated results by the average flow rate coefficient method to the results in Reference [3] (see Reference [3] Figure 14a and Figure 23) is shown in the table below.

\bar{A}	w_1							ξ_T
	0	0.167	0.333	0.500	0.667	0.834	1.000	
Average flow rate coefficient method	0.116	0.212	0.369	0.482	0.645	0.802	1.000	5.41
Ref. [3]	0.125	0.231	0.363	0.494	0.640	0.802	1.000	5.40

The w curve obtained above is based on the experimental data of the inlet orifice in this experiment. The relation between the flow rate coefficient c^0 (the superscript "o" represents the inlet orifice in our experiment here) and the flow parameter F_p is shown in Figure 1. When the geometric shape of the inlet orifice we want

to calculate is different from the inlet orifice used in this experiment so that its flow rate coefficient C and F_p relation is different from the relation in Figure 1, the effect of the variation in flow rate coefficient must be taken into account. Under this circumstance, we may convert the various shaped inlet orifice area A_h to A_h^0 according to the principle of $CA_h = \text{constant}$, i.e., the A_h^0 in Eq. (3-5) should be calculated by the equation below

$$A_h^0 = (c/c^0)A_h \quad (3-9)$$

Results of calculation show that the flow rate coefficient of the inlet orifice is basically only related to $x\sqrt{\phi}$; hence the value of the flow parameter F_p will also be determined basically by the value of $x\sqrt{\phi}$. The relational curves between c^0 and F_p and $x\sqrt{\phi}$ may be formed from our experimental result as shown in Figure 9 and Figure 10. According to Figure 9, the c^0 value may be determined and the value of F_p may be determined from Figure 10 and hence the c value for other inlet orifice shapes may be found from the given $c = f(F_p)$ relationship (this relation must be given first in the calculation of combustion chamber flow rate distribution).

As mentioned above, it is necessary to know c/c^0 when X is to be determined and the value of c/c^0 is to be determined based on the X value. Hence

Figure 9a. Relation between small orifice flow rate coefficient c^0 and $x\sqrt{\phi}$ (for small $x\sqrt{\phi}$ values).

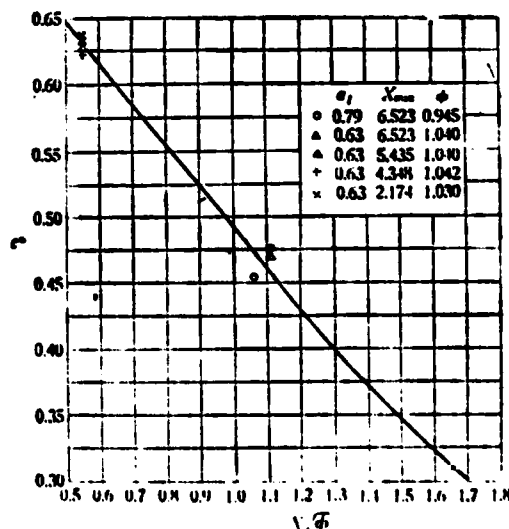


Figure 9b. Relation between small orifice flow rate coefficient c^0 and $x\sqrt{\phi}$ (for large $x\sqrt{\phi}$ values).

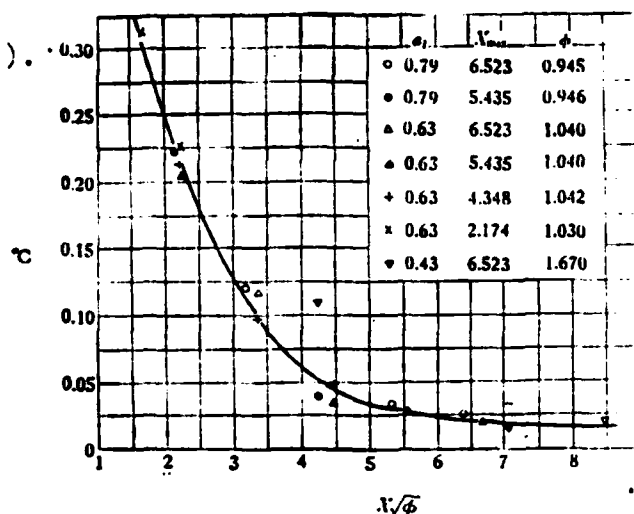


Figure 10a. Relation between flow parameter F_p and $x\sqrt{\phi}$ (for small $x\sqrt{\phi}$ values).

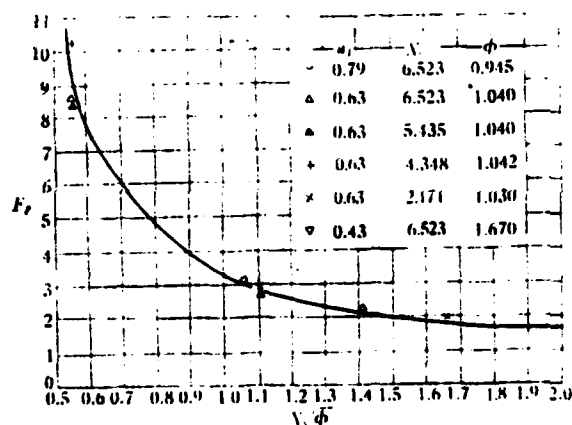
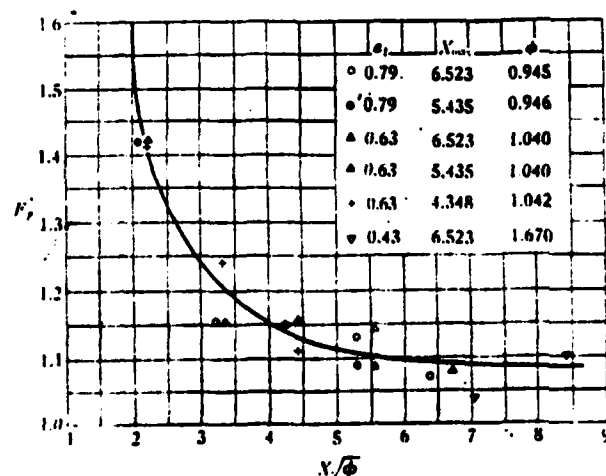


Figure 10b. Relation between flow parameter F_p and $x\sqrt{\phi}$ (for large $x\sqrt{\phi}$ values).



/191

A computational process is required in the calculation. Under these circumstances, it is best to calculate backward from the last row of orifices of the flame tube toward the front.

In the section below, we shall discuss the method of finding V_{jo} and V_{jex} values:

The value of the jet velocity v_{jo} at the initial flame tube cross-section may be easily determined from Eq. (3-3). However, the value of ω_{max} needs to be found from the curves based on the value of $X\phi$ and the value of ϕ is still unknown. Hence, in the calculation, one may first take a ϕ value (e.g. for cooling air we may take $\phi \approx 1$ and when heating ratio >1 , we may choose larger values for ϕ), find ω_{max} from ω curve, then calculate v_{jo} value from Eq. (3-3). We shall see below that the jet velocity v_{jex} at the outlet cross-section of the combustion chamber may be calculated from the value of v_{jo} , and therefore a new value of ϕ may be found. Based on this ϕ value, we can re-calculate v_{jo} until the 2 successive values of v_{jo} are close to each other.

Table 2 gives the comparison between the v_{jo} value as calculated above and the experimental results. We can see that the v_{jo} values calculated from the ω curves are very close to the experimental values.

Table 2. Comparison of the results calculated from the average flow rate coefficient method to the experimental values.

parameter	method	test piece								
		$a_1=0.79$ $X_{max} =$ 6.523	$a_1=0.79$ $X_{max} =$ 5.435	$a_1=0.63$ $X_{max} =$ 6.523	$a_1=0.63$ $X_{max} =$ 5.435	$a_1=0.63$ $X_{max} =$ 4.348	$a_1=0.63$ $X_{max} =$ 2.174	$a_1=0.63$ $X_{max} =$ 1.087	$a_1=0.43$ $X_{max} =$ 6.523	$a_1=0.43$ $X_{max} =$ 5.435
%	average flow rate coeff. method	5.25	5.26	2.96	2.98	3.00	3.35	4.74	2.02	1.86
	experi. value	5.24	5.22	2.97	2.98	3.00	3.40	4.63	1.94	1.92
%	avg. flow rate coeff. method	1.02	1.03	0.96	0.97	0.99	1.29	2.84	1.66	1.62
	experi. value	1.02	1.05	1.13	1.16	1.21	1.40	2.62	1.34	1.39

It is necessary to know the value of ϕ in order to make use of the ω curve in Figure 7 in computations. It should be pointed out that the v_{jex} value in the horizontal coordinate ϕX of Figure 7 has not taken into account the total pressure loss of the 2 passages. Detailed calculation shows that the effect of whether or not taking into account of the v_{jex} of the total pressure loss of the 2 passages in getting the ω curve in the calculation of flow rate distribution and total pressure loss is basically the same, but the latter is much simpler. Under this condition, we have

$$v_{jex}^2 = \frac{p_{a1}^* - p_{lex}}{(\rho_s/2)V_s^2} \quad (3-10)$$

From the flame tube dynamic equation:

$$\begin{aligned} p_{lex}A_{lex} + p_{lex}A_{lex}V_{lex}^2 - \sum_{i=1}^n (\Delta Q_i V_{ai}) = p_n A_n + p_n A_n V_n^2 \\ + (A_{lex} - A_n)(p_{lex} + p_n)/2 \end{aligned} \quad (3-11)$$

We get

$$v_{jex}^2 = v_{j0}^2 + \frac{1}{a_{l1} + a_{lex}} \left[\frac{\theta_{ex}}{a_{lex}} - \frac{\theta_1}{a_{l1}} (c_0 a_{l0} v_{j0})^2 - \frac{(3a_{a1} - a_{lex})}{4} (v_{j0} \omega_{max})^2 \right] \quad (3-12)$$

under the condition of $a_{a1} = \text{const}$ and $a_{li} = \text{const}$, then

$$v_{jex}^2 = v_{j0}^2 + \frac{2\theta_{ex}}{a_l^2} - 2\theta_1 \left(\frac{c_0 a_{l0} v_{j0}}{a_l} \right)^2 - \frac{a_s}{a_l} (v_{j0} \omega_{max})^2 \quad (3-13)$$

The combustion chamber friction coefficient is

$$\xi_r = \frac{p_{a1}^* - p_{lex}^*}{\rho_s V_s^2/2} = v_{jex}^2 - \frac{\theta_{ex}}{a_{lex}^2} \quad (3-14)$$

It should be pointed out that the average flow rate coefficient method introduced above is also applicable to the situation of ring type combustion chamber. Due to the limitation of space, we shall not discuss it here.

4. COMPARISON OF EXPERIMENTAL RESULTS AND COMPUTATIONAL RESULTS FOR COMBUSTION CHAMBER FLOW RATE DISTRIBUTION AND TOTAL PRESSURE LOSS

In Figures 11, 12, 5 and 6 are presented respectively the comparison of the calculated results and experimental results for flow rate distribution and total pressure loss. From the diagrams, it can be seen that the results calculated by solving the one dimensional flow equations (not taking into account of total pressure loss of 2 passages) and the results calculated by the average flow rate coefficient are in good agreement with the experimental result while those calculated by the flow resistance method differ more from the experimental result.

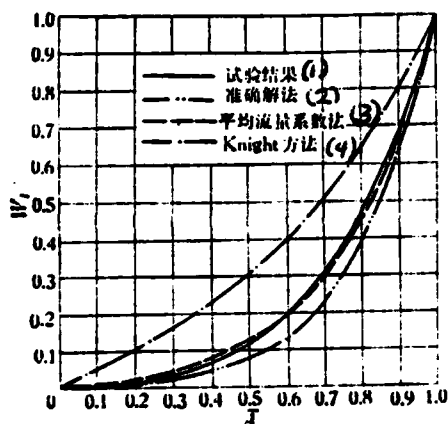


Figure 11. Comparison between calculated results of flow distribution and experimental value. ($\sigma_1 = 0.79$, $\chi_{\text{max}} = 6.323$)

1 - Experimental results;
2 - calculated results;
3 - average flow rate coefficient; 4 - Knight method

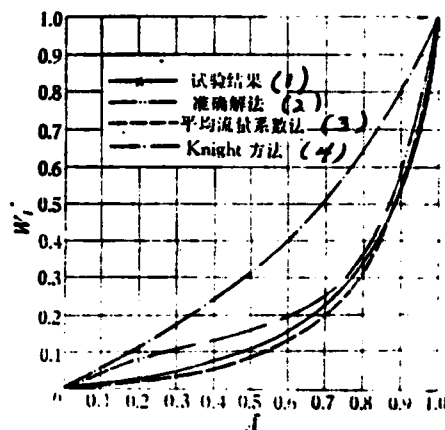


Figure 12. Comparison between the computed values of flow rate and the experimental value ($\sigma_1 = 0.43$, $\chi_{\text{max}} = 6.523$)

1 - Experimental results;
2 - calculated results;
3 - average flow rate coefficient; 4 - Knight method

/193

SYMBOL EXPLANATION

A, a - represent respectively the area and relative area (A/A_r)

$$\bar{A} = \frac{\sum_{i=1}^n A_{hi}}{\sum_{i=1}^n A_{hi}}$$

c - orifice flow rate coefficient (corresponding to total static pressure difference)

$$F_p = (V_i/V_a)^2 \quad - \text{flow parameter}$$

$$G_{pi} = A_{hi} / \sum_{i=1}^n A_{hi}^2 \quad - \text{area parameter}$$

n - number of orifices (not including the orifice in the head of the flame tube)

$\bar{p}, p^*, \Delta p^*$ - respectively static pressure, total pressure and total pressure difference

ΔQ - weight flow rate through flame tube orifice

$$q = (\rho/2)V^2 \quad - \text{velocity head}$$

V, v - respectively velocity and relative velocity (V/V_r)

$$w_{ii} = \sum_{i=1}^n \Delta Q_i / \rho g A_i V_i$$

$\Delta w = \Delta Q/Q$ - relative flow rate through flame tube orifice

$$X = 1/G_p = \sum_{i=1}^n A_{hi}^2 / A_{hi}$$

$$\xi = (p_{01}^* - p_{02}^*) / \frac{\rho}{2} V^2 \quad - \text{friction coefficient}$$

SUBSCRIPT

a, l - represent respectively 2 passage and flame tube.

h - flame tube orifice

i - order number of the cross-section of the orifice array or in front of the orifice array of the flame tube

j - order number of the orifice jet or orifice array

o - head orifice of the combustion chamber (including the vortex generator)

ex, in - respectively the outlet and inlet cross-section of the combustion chamber or the 2 passage way.

r - reference cross-section (taken as $A_r = A_1 + A_2$ in this paper)

SUPERSCRIPIT

o - corresponds to the inlet orifice used in our experiment

* - stagnation parameter

REFERENCES

- [1] Ditttrich, Ralph T. and Graves, Charles C., Discharge Coefficients for Combustor-Liner Air-Entry Holes, I. Circular Holes with Parallel Flow, NACA TN 3663, 1956.
- [2] Knight, H. A. and Walker, R. B.: The Component Pressure Losses in Combustion Chambers, ABC R & M 2987, 1957.
- [3] Analysis of Total-Pressure Loss and Airflow Distribution for Annular Gas Turbine Combustors, NASA TN D-5285, 1964.